

---

# Ultraschallmodifikation von Metallen – Einfluss des Ultraschalls auf die Dichte geometrisch notwendiger Versetzungen

---

Bearbeitung: Akaash Chakkaravarthy  
Betreuung: Jun.-Prof. Dr.-Ing Moritz Liesegang



Materials Science & Engineering  
Prof. Dr.-Ing. Tilmann Beck



---

# Ultrasonic modification of metals - influence of ultrasound on the density of geometrically necessary dislocations

---

Student: Akaash Chakkaravarthy

Supervision: Jun.-Prof. Dr.-Ing Moritz Liesegang

MA 8607 – 04/24

Eidesstattliche Erklärung

Name: *Chakkaravarthy*

Studiengang: *MSc Commercial*

*Vehicle*

*Technology(CVT)*

Vorname: *Akaash*

Matrikelnummer:

Geburtsort: *Virudhunagar, India*

Geburtsdatum:

Hiermit versichere ich, dass ich die Mastersrbet gemäß § 13 Abs. 6 DPO Maschinenbau und Verfahrenstechnik vom 17.08.2009 selbständig verfasst und keine anderen als die angegebenen Quellen und Hilfsmittel benutzt habe.

Mir ist bewusst, dass bei einem Verstoß gegen obige Erklärung nicht nur die betreffende Prüfungsleistung mit der Note – 5,0 – wegen Täuschungsversuchs gewertet werden, sondern auch eine Exmatrikulation erfolgen kann.

Kaiserslautern,

(Datum)

\_\_\_\_\_

\_\_\_\_\_  
(Akaash Chakkaravarthy)

## Abstract

Ultrasonic processes are typically energy time and cost efficient and recently of high interest, especially for joining. However, the sonication of materials is often associated with phenomena that remain largely unresolved to date, such as increased ductility during sonication and microstructural changes. To gain a deeper understanding of the elementary processes contributing to increased ductility through ultrasonic sonication, this study investigates the modification of metal by ultrasound and its impact on the density of geometrically necessary dislocations (GNDs). The presence of a large grain structure in IN617 allowed the effect of ultrasound to be more easily observed and analysed. Therefore, samples of IN617 were used for study. The effect of ultrasonic treatment on the density of GNDs in IN617 was analysed using Electron Backscatter Diffraction (EBSD) measurements. Additionally, an E–m model and finite element modelling (FEM) were employed to gain deeper insights into grain behaviour. The FEM model was successfully applied by correlating the mechanical behaviour predicted by the E–m model based on Young’s modulus and the Schmid factor with experimental observations. A combination of experimental data and computational modelling was used to analyse the effect of ultrasonic treatment on dislocation dynamics. EBSD data from three different samples were used to simulate the material’s response to various mechanical and ultrasonic loading conditions. The analysis revealed distinct variations in GND density across the samples. Many grains exhibited a unique response under different loading conditions, as observed through Young’s modulus, Schmid factor, resolved shear stress, and plastic strain. The results indicate that ultrasonic treatment influences dislocation behaviour by either promoting stress relaxation or increasing local hardness.

A geometrically necessary dislocation (GND) analysis was conducted to explore the effect of plastic deformation on three different samples (N1, N2, and N3) of IN617 alloy after sonication was applied. Several software tools, including MATLAB, MTEX tool box, Origin, GMSH, Python and Dassault Abaqus were employed to assist in the analysis. Three samples were analysed under different conditions: in the first case, the initial sample was examined; for the second case, the sample was subjected to a force of 400 N; for the third case, a force ranging from 100 to 200 N was applied over a period of 50 milliseconds; and for the fourth case, the same force was applied for a period of 5000 milliseconds. The GND analysis of all these cases was carried out using Electron Backscatter Diffraction (EBSD). Additionally, various plots, such as plastic strain, resulting shear stress, von Mises stress, and maximum principal stress,

were generated using ABAQUS. Other important data, including Young's modulus ( $E$ ), Schmid factor ( $m$ ), and the product of Young's modulus and Schmid factor ( $E \cdot m$ ), were also plotted. These graphs were compared, and a comprehensive study was conducted to understand the likelihood of plastic deformation under different conditions. By conducting the aforementioned analysis and detailed study, a comprehensive understanding of the influence of ultrasound on the density of geometrically necessary dislocations (GNDs) in the nickel-based super-alloy IN617 was achieved.

I. Table of Contents	
<b>II. List of Figures</b> .....	<b>III</b>
<b>III. List of Tables</b> .....	<b>VII</b>
<b>IV. Symbols and Abbreviations</b> .....	<b>VIII</b>
<b>1. Motivation and objectives of the work</b> .....	<b>1</b>
<b>2. Fundamentals and literature study</b> .....	<b>3</b>
2.1. Deformation and fracture of materials .....	3
2.1.1. Edge dislocation .....	3
2.1.2. Screw dislocation .....	4
2.2. Geometrically necessary dislocations (GND) .....	5
2.3. Various factors influencing GND.....	5
2.4. Calculation of GND density using EBSD data .....	6
2.4.1. Gathering Orientation Data .....	6
2.4.2. Determining Lattice Curvature.....	6
2.4.3. Using the Dislocation Density Tensor .....	7
2.4.4. Applying statistical Optimisation.....	7
2.4.5. Excluding High-Angle Grain Boundaries (HAGBs) .....	7
2.5. Ultrasonic and its impact on materials .....	8
2.6. Ultrasonic system .....	9
2.7. Role of Youngs modulus and Schmid factor in plastic deformation ...	11
<b>3. Materials and Methodologies</b> .....	<b>13</b>
3.1. Scanning electron Microscope (SEM) .....	13
3.2. An Overview of Inconel 617 Alloy .....	15
3.3. Softwares used.....	16
3.4. Measurement of EBSD data .....	16
3.5. EBSD Data to FEM model.....	19
3.6. GND density Analysis .....	22
<b>4. Results</b> .....	<b>24</b>

---

<b>5. Conclusion .....</b>	<b>57</b>
<b>6. Literature .....</b>	<b>59</b>
<b>7. Appendix .....</b>	<b>66</b>
7.1. Calculation of energy needed to move a dislocation.....	79

## II. List of Figures

Fig. 2-1 Illustration of edge dislocation .....	4
Fig. 2-2 Illustration of screw dislocation .....	4
Fig. 2-3 Schematic representation of an Ultrasonic vibration system&(1-Generator,2-Transducer,3-Concentrator,4-Sample) .....	10
Fig. 2-4 Ultrasonic metal testing equipment .....	10
Fig. 3-1 schematic representation of Scanning electron microscope. ....	13
Fig. 3-2 SEM images of samples a)N1, b)N2, c)N3 .....	14
Fig. 3-3 Sample used in investigation .....	15
Fig. 3-4 Schematic representation of electron beam, specimen and phosphor screen [72] .....	17
Fig. 3-5 Damage from sectioning IN617 alloy. ....	18
Fig. 3-6 Damage on the surface due to polishing of IN617 alloy .....	18
Fig. 3-7 Recalculated Microstructure .....	20
Fig. 3-8 Mesh obtained from GMSH software .....	21
Fig. 3-9 Abaqus file with added material properties and boundary conditions .....	21
Fig. 3-10 Experimental Procedure for Analysing GND Density Evolution in IN617 Alloy Under Mechanical and Ultrasonic Conditions .....	23
Fig. 4-1 a) Youngs modulus E in GPa, b) Product of Youngs Modulus and Schmid factor ( $E \cdot m$ ) in GPa, c) Schmid factor, d) IPF(Inverse Pole figure), e) Plastic strain, f) Resulting shear stress in MPa .....	25
Fig. 4-2 GND density maps for all tests conducted on Sample N1: (a) N1_A (initial), (b) N1_B (only Force 400N), (c) N1_C (20 $\mu$ m, ~100-200N, 50ms) and (d) N1_D (20 $\mu$ m, ~100-200N, 5000ms).....	26
Fig. 4-3 a) IPF (Inverse pole figure) and evolution of GND Density in Grain 1 b) N1_A (initial), c) N1_B (only Force 400N), d) N1_C (20 $\mu$ m, ~100-200N, 50ms), e) N1_D (20 $\mu$ m, ~100-200N, 5000ms).....	27
Fig. 4-4 a) IPF(Inverse pole figure) and Evolution of GND Density in Grain 2 b) N1_A(initial), c) N1_B(only Force 400N), d) N1_C(20 $\mu$ m, ~100-200N, 50ms), e) N1_D(20 $\mu$ m, ~100-200N, 5000ms).....	27
Fig. 4-5 a) IPF (Inverse pole figure) and evolution of GND Density in Grain 3 b) N1_A (initial), c) N1_B (only Force 400N), d) N1_C (20 $\mu$ m, ~100-200N, 50ms), e) N1_D (20 $\mu$ m, ~100-200N, 5000ms).....	28

Fig. 4-6 a) IPF (Inverse pole figure) and evolution of GND Density in Grain 4 b) N1_A (initial), c) N1_B (only Force 400N), d) N1_C (20μm, ~100-200N, 50ms), e) N1_D (20μm, ~100-200N, 5000ms).....	29
Fig. 4-7 a) IPF (Inverse pole figure) and evolution of GND Density in Grain 5 b) N1_A (initial), c) N1_B (only Force 400N), d) N1_C (20μm, ~100-200N, 50ms), e) N1_D (20μm, ~100-200N, 5000ms).....	29
Fig. 4-8 a) IPF (Inverse pole figure) and evolution of GND Density in Grain 6 b) N1_A (initial), c) N1_B (only Force 400N), d) N1_C (20μm, ~100-200N, 50ms), e) N1_D (20μm, ~100-200N, 5000ms).....	30
Fig. 4-9 a) IPF (Inverse pole figure) and evolution of GND Density in Grain 7 b) N1_A (initial), c) N1_B (only Force 400N), d) N1_C (20μm, ~100-200N, 50ms), e) N1_D (20μm, ~100-200N, 5000ms).....	30
Fig. 4-10 Evolution of GND Density in IN617 Alloy Grains Under Mechanical and Ultrasonic Conditions for sample N1 .....	31
Fig. 4-11 SEM image of Sample N1 a) With slip bands b) Highlighted slip bands .....	34
Fig. 4-12 a) Youngs modulus E in GPa, b) Product of Youngs Modulus and Schmid factor ( $E \cdot m$ ) in GPa .....	35
Fig. 4-13 GND density maps for all tests conducted on Sample N2: (a) N2_A (initial), (b) N2_B (only Force 400N), (c) N2_C (20μm, ~100-200N, 50ms) and (d) N2_D (20μm, ~100-200N, 5000ms).....	36
Fig. 4-14 a) IPF (Inverse pole figure) and evolution of GND Density in Grain 7 b) N2_A (initial), c) N2_B (only Force 400N), d) N2_C (20μm, ~100-200N, 50ms), e) N2_D (20μm, ~100-200N, 5000ms). .....	37
Fig. 4-15 a) IPF (Inverse pole figure) and evolution of GND Density in Grain 7 b) N2_A (initial), c) N2_B (only Force 400N), d) N2_C (20μm, ~100-200N, 50ms), e) N2_D (20μm, ~100-200N, 5000ms). .....	37
Fig. 4-16 a) IPF (Inverse pole figure) and evolution of GND Density in Grain 7 b) N2_A (initial), c) N2_B (only Force 400N), d) N2_C (20μm, ~100-200N, 50ms), e) N2_D (20μm, ~100-200N, 5000ms). .....	38
Fig. 4-17 a) IPF (Inverse pole figure) and evolution of GND Density in Grain 7 b) N2_A (initial), c) N2_B (only Force 400N), d) N2_C (20μm, ~100-200N, 50ms), e) N2_D (20μm, ~100-200N, 5000ms). .....	38
Fig. 4-18 Plastic Strain and Resulting Shear Stress Distribution in an IN617 Alloy Grain 4..	39

Fig. 4-19 a) IPF (Inverse pole figure) and evolution of GND Density in Grain 7 b) N2_A (initial), c) N2_B (only Force 400N), d) N2_C (20 $\mu$ m, ~100-200N, 50ms), e) N2_D (20 $\mu$ m, ~100-200N, 5000ms). .....	39
Fig. 4-20 a) IPF (Inverse pole figure) and evolution of GND Density in Grain 7 b) N2_A (initial), c) N2_B (only Force 400N), d) N2_C (20 $\mu$ m, ~100-200N, 50ms), e) N2_D (20 $\mu$ m, ~100-200N, 5000ms). .....	40
Fig. 4-21 Plastic Strain and Resulting Shear Stress Distribution in an IN617 Alloy Grain 6..	40
Fig. 4-22 a) IPF (Inverse pole figure) and evolution of GND Density in Grain 7 b) N2_A (initial), c) N2_B (only Force 400N), d) N2_C (20 $\mu$ m, ~100-200N, 50ms), e) N2_D (20 $\mu$ m, ~100-200N, 5000ms). .....	41
Fig. 4-23 a) IPF (Inverse pole figure) and evolution of GND Density in Grain 7 b) N2_A (initial), c) N2_B (only Force 400N), d) N2_C (20 $\mu$ m, ~100-200N, 50ms), e) N2_D (20 $\mu$ m, ~100-200N, 5000ms). .....	41
Fig. 4-24 a) IPF (Inverse pole figure) and evolution of GND Density in Grain 7 b) N2_A (initial), c) N2_B (only Force 400N), d) N2_C (20 $\mu$ m, ~100-200N, 50ms), e) N2_D (20 $\mu$ m, ~100-200N, 5000ms). .....	42
Fig. 4-25 a) IPF (Inverse pole figure) and evolution of GND Density in Grain 7 b) N2_A (initial), c) N2_B (only Force 400N), d) N2_C (20 $\mu$ m, ~100-200N, 50ms), e) N2_D (20 $\mu$ m, ~100-200N, 5000ms). .....	42
Fig. 4-26 a) IPF (Inverse pole figure) and evolution of GND Density in Grain 7 b) N2_A (initial), c) N2_B (only Force 400N), d) N2_C (20 $\mu$ m, ~100-200N, 50ms), e) N2_D (20 $\mu$ m, ~100-200N, 5000ms). .....	43
Fig. 4-27 Evolution of GND Density in IN617 Alloy Grains Under Mechanical and Ultrasonic Conditions for sample N2 .....	43
Fig. 4-28 SEM image of Sample N2 a) With slip bands b) Highlighted slip bands .....	46
Fig. 4-29 a) Young's modulus E in GPa, b) Product of Young's Modulus and Schmid factor (E.m) in GPa, c) Schmid factor(m), d) IPF(Inverse Pole figure), e) Plastic strain, f) Resulting shear stress in MPa. ....	47
Fig. 4-30 GND density maps for all tests conducted on Sample N3: (a) N3_A (initial), (b) N3_B (only Force 400N), (c) N3_C (20 $\mu$ m, ~100-200N, 50ms) and (d) N3_D (20 $\mu$ m, ~100-200N, 5000ms). .....	48

Fig. 4-31 a) IPF (Inverse pole figure) and evolution of GND Density in Grain 7 b) N3_A (initial), c) N3_B (only Force 400N), d) N3_C (20µm, ~100-200N, 50ms), e) N3_D (20µm, ~100-200N, 5000ms). .....	49
Fig. 4-32 a) IPF (Inverse pole figure) and evolution of GND Density in Grain 7 b) N3_A (initial), c) N3_B (only Force 400N), d) N3_C (20µm, ~100-200N, 50ms), e) N3_D (20µm, ~100-200N, 5000ms). .....	49
Fig. 4-33 a) IPF (Inverse pole figure) and evolution of GND Density in Grain 7 b) N3_A (initial), c) N3_B (only Force 400N), d) N3_C (20µm, ~100-200N, 50ms), e) N3_D (20µm, ~100-200N, 5000ms). .....	50
Fig. 4-34 a) IPF (Inverse pole figure) and evolution of GND Density in Grain 7 b) N3_A (initial), c) N3_B (only Force 400N), d) N3_C (20µm, ~100-200N, 50ms), e) N3_D (20µm, ~100-200N, 5000ms). .....	51
Fig. 4-35 a) IPF (Inverse pole figure) and evolution of GND Density in Grain 7 b) N3_A (initial), c) N3_B (only Force 400N), d) N3_C (20µm, ~100-200N, 50ms), e) N3_D (20µm, ~100-200N, 5000ms). .....	51
Fig. 4-36 Evolution of GND Density in IN617 Alloy Grains Under Mechanical and Ultrasonic Conditions for sample N3 .....	52
Fig. 4-37 SEM image of Sample N3 a) With slip bands b) Highlighted slip bands .....	55

### III. List of Tables

Tab. 1 List of Samples and the parameters they are tested with. ....	11
Tab. 2 SEM Imaging parameters.....	14
Tab. 3 Yield stress and plastic strain.....	22

## IV. Symbols and Abbreviations

### Symbols

$E$	Youngs modulus	[GPa]
$m$	Schmid factor	[-]
$E \cdot m$	Product of Youngs modulus and Schmid factor	[MPa]
$\tau_{a,res}$	Resolved Shear stress	[Pa]
$\sigma_a$	Applied stress amplitude	[Pa]
$\varepsilon_{a,t}$	Strain amplitude	[-]
$C$	Stiffness matrix	[-]
$E_d$	Energy per unit length of dislocation	[J/m]
$G$	Shear modulus	[Pa]
$b$	Burgers victor	[m]
$\nu$	Poisson's ratio	[-]
$w$	Work done	[J]
$\tau$	Applied shear stress	[Pa]
$L$	Distance moved by dislocation	[m]

### Abbreviations

GND	Geometrically necessary dislocations
BCC	Body-centered cubic
FCC	Face-centered cubic
CPH	Close-packed hexagonal
SSD	Statistically stored dislocations
OFHC	Oxygen-free high-conductivity
UST	Ultrasonic Treatment
SEM	Scanning Electron microscope
GAM	Grain average misorientation
KAM	Kernel average misorientation
HAGB	High angle grain boundaries
IN617	Inconel617 alloy

## 1. Motivation and objectives of the work

In recent years, the modification of metals through ultrasonic treatment has gained attention due to its ability to enhance material properties, refine the microstructure of metals. [1] Ultrasonic vibration also known as sonication is a process that utilizes high frequency wave to move particles in a medium. When ultrasonic vibration is applied to a metal, it can introduce plastic deformation, affect dislocation densities, and alter the grain structure within the metal along with several other acoustic effects that include increased fatigue life and cavitation. [2,3]

Material deformation can result from exposing the material to ultrasonic vibrations. This occurs due to the superposition of high-frequency acoustic waves onto existing mechanical loads, which enhances atomic mobility and facilitates dislocation movement within the material structure. [4] Another notable process is the generation of high strain rate plastic deformation, in which ultrasonic energy reduces internal friction within the material and promotes dislocation mobility, resulting in increased ductility and reduced work hardening. [5] Additionally, ultrasonic energy promotes stress relaxation, which can help enhance fatigue life and refine the microstructure. [6] Ultrasonic deformation is widely used in applications such as ultrasonic welding, ultrasonic shot peening, and ultrasonic-assisted machining. The use of ultrasonics in manufacturing enables efficient processing of materials such as titanium and other high-strength steels, increasing overall productivity. With ongoing advancements in understanding the relationship between ultrasonics and material behaviour, the application of ultrasonic energy remains an area of significant research interest. [7] The density of geometrically necessary dislocations (GNDs), using nickel-based super-alloys such as IN617, was explored in this research in relation to the effects of ultrasonic treatment.

Though laboratory experiments provide accurate results, ultrasonic Parameters such as amplitude, frequency, processing duration should be selected precisely in order to have accurate results when used in large scale components. [8,9] Available research on ultrasonic treatment of metals majorly focus on Aluminium, titanium with only a limited research on nickel based alloys. [9] This can be used as motivation for investigating into how ultrasonic modification influences GNDs in IN617 under various conditions. The reason to IN617 alloy was selected for this study due to its large grain size, which enables accurate Electron Backscatter Diffraction (EBSD) measurements.

In this study, the effect of applied force and ultrasound on the density and annihilation of Geometrically Necessary Dislocations in IN617 alloy was observed and explored. With the help of EBSD analysis, various factors influencing dislocation dynamics and their effects on material properties are studied and documented. Three samples of IN617 were subjected to force and sonication with varying amplitude and duration. It was observed that the application of sonication aided in the annihilation of GNDs but also led to material deformation. The factors influencing GNDs were investigated, and methods to analyse this deformation using different tools were also analysed. Additionally, the Em model was utilised to understand the effects of plastic strain. The super imposition of force and Sonics leads to a more pronounced plastic strain. The annihilation of geometrically necessary dislocations (GNDs) depends on the induced energy. Furthermore, the mechanical properties of the grains ( $E$ ,  $m$ , and  $E \cdot m$ ) and those of their neighbouring grains play a crucial role in determining the onset of plastic strain and the resulting shear stress. According to the Em-model, grains susceptible to early plastic strain exhibit corresponding changes in GND density. Therefore, the principles of the Em-model can be applied to explain the observed modifications in GND density under these conditions. By attaining a clear understanding of the material's performance and its response to ultrasound, it will be possible to understand dislocation behaviour. [3]

## 2. Fundamentals and literature study

### 2.1. Deformation and fracture of materials

Deformation in general can be referred as change in shape or size of a material when it is subjected to external factors like tension, compression or shear. Based on the material properties and the amount of applied stress the phenomenon could be a reversible change such as elastic deformation or a permanent change such as plastic deformation. [10] Macroscopic deformation behaviour can be studied and analysed by using stress strain curves obtained from various mechanical tests like tensile, compression and creep testing. [10] Through these tests it is possible to identify three unique stages of deformation: elastic deformation, plastic deformation, and failure. Each stage responds in a unique way to the applied stress. [8] The initial stage of deformation is reversible and follows Hooke's law ( $\sigma = E \cdot \epsilon$ ), Where  $E$  is the Young's modulus. [11]

When the applied stress on a material exceeds its yield strength, dislocations move along the crystal lattice, resulting in permanent deformation. [12] The next stage of plastic deformation is strain hardening, which occurs due to the interaction. [12,13] Dislocation motion can also be affected by high temperatures, which can either increase or decrease strain hardening depending on the specific conditions. [12,13] Fracture occurs due to structural degradation or dislocation accumulation. Fracture mechanisms often depend on the loading conditions. When the material undergoes higher strain, localized thinning occurs, a phenomenon known as necking. Fracture occurs due to structural degradation or dislocation accumulation.

At the atomic level, dislocation dynamics primarily govern the deformation, facilitating plastic deformation. These mechanisms are influenced by the interaction of dislocations with the crystal lattice, solute atoms, and microstructural features. [14] Several types of dislocations can be observed at atomic level namely edge dislocation, screw dislocation and mixed dislocation.

#### 2.1.1. Edge dislocation

Under mechanical loading the motion of atoms happen perpendicular to the dislocation line, driven by shear stresses. This movement is considered important for accommodating plastic strain during deformation. Edge dislocation in general is defined by an extra half plane of atoms that distort the lattice locally. [14,15] This can be understood by the figure provided below.

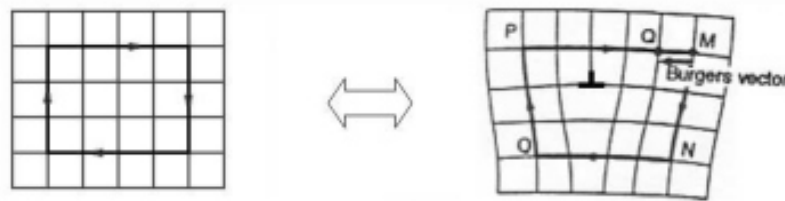


Fig. 2-1 Illustration of edge dislocation

### 2.1.2. Screw dislocation

Helical distortion of atomic planes occurs due to screw dislocations. This movement takes place parallel to the dislocation line. [14,15] Illustration of screw dislocation is provided in Fig 2-2.

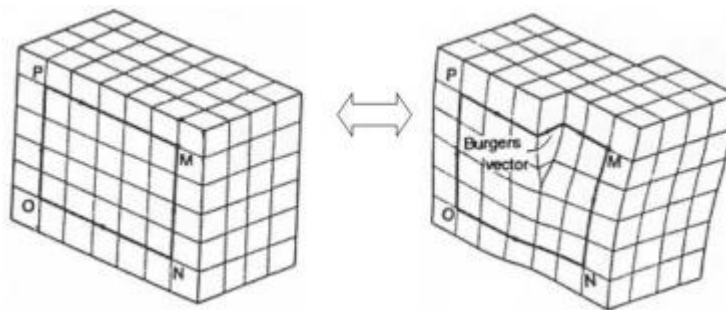


Fig. 2-2 Illustration of screw dislocation

There is also a phenomenon known as mixed dislocations where characteristics of both Edge and screw dislocations can be seen. Strain hardening and plasticity are contributed as a result of their behaviour under mechanical stress. [14]

These phenomena help in understanding material behaviour, as they influence properties such as strength, conductivity, and ductility. [16,17] One such phenomenon is dislocation multiplication, where dislocation density increases through mechanisms like Frank-Read sources during mechanical deformation, generating new dislocations under stress. [12,18] Another phenomenon is dislocation interaction, where dislocations interact under mechanical load, leading to pile-up at grain boundaries, which enhances the material's strength. [12,19] Other phenomena, such as pipe diffusion, influence deformation behaviour by promoting atom segregation near dislocations, contributing to strain localization. [12,20] Under cyclic mechanical loading, cross-slip becomes essential for accommodating larger grains and preventing major failures. This phenomenon is associated with stacking faults or cross-slip

events. [12,18] Precipitation-dislocation interaction is another critical phenomenon where the interaction between precipitates and dislocations can contribute to strengthening but may also lead to micro crack formation due to localized stress concentrations. [19] Severe mechanical deformation can lead to the creation of vacancies, contributing to damage accumulation during tensile loading. This key atomic-scale phenomenon is known as vacancy formation. [8] Interplay between all the above stated phenomena determine the strength and creep resistance of an alloy. [15] By using methods like electron Microscopy and atom probe tomography it is possible to obtain in depth knowledge about these mechanisms. [21,22]

## 2.2. Geometrically necessary dislocations (GND)

The structure of a crystalline solid typically consists of numerous randomly oriented grains separated by grain boundaries. Most materials have crystalline nature characterized by atoms arranged in a repeating pattern that extends periodically in three dimensions. [23] Inside a crystal structure dislocations are usually classified into two main categories statistically stored dislocations (SSDs) and geometrically necessary dislocations (GNDs). [24] SSDs are vaguely distributed within the crystal lattice and do not affect the crystal's orientation. In contrast, GNDs are responsible for accommodating plastic deformation and inducing changes in crystal orientation. [24]

GNDs play a crucial role in understanding material behaviour under deformation and contribute to enhancing material strength. Several factors, such as strain, stress, and strain rate, significantly influence GND characteristics. Experimental observations indicate that GND density tends to be higher along grain boundaries than within grain interiors, highlighting the localized nature of these dislocations and their significant impact on material performance. The measurement of GND density is typically obtained by analysing lattice curvature, which is facilitated by techniques such as Electron Backscatter Diffraction (EBSD). [14]

## 2.3. Various factors influencing GND

This discussion explores key factors such as strain, strain rate, temperature, and microstructure, which significantly influence the behaviour of geometrically necessary dislocation (GND) density. [25] With respect to applied strain, it can be observed that as strain increases, the corresponding GND density also increases. Additionally, GNDs tend to concentrate along grain boundaries, highlighting their redistribution and accumulation within the material. [26,27] GND accumulation is further accelerated at high strain rates, emphasizing the influence of strain rate on material response. [28] Regarding temperature, studies indicate that GND density

decreases as temperature increases, suggesting that thermal energy promotes dislocation annihilation and redistribution. [29,30]The microstructure of an alloy also plays a crucial role in plastic deformation and GND behaviour. In materials where slip is the dominant deformation mechanism, GND accumulation occurs more gradually. However, twinning is another important mechanism of deformation, and when twinning is the primary mechanism of plastic deformation, the GND density tends to increase more slowly than in materials where slip predominate.[31] The connection between microstructure and GND formation provides valuable insights into how materials respond to mechanical stress. Therefore, all the discussed factors play a key role in determining GND characteristics. Each of these factors is crucial in defining GND behaviour and material response under mechanical stress.

## **2.4. Calculation of GND density using EBSD data**

Calculating geometrically required dislocation (GND) density is a methodical and complex process that combines statistical analysis, mathematical modelling, and experimental methods. [32] In our research, EBSD measurements were performed with a step size of 7  $\mu\text{m}$  on the sample to ensure adequate spatial resolution for analysing the sample. With advancements in technology, an EBSD camera is now used in place of a phosphor screen to capture the diffraction patterns from the sample. In our research, a Hikari EBSD camera was utilized to capture the EBSD patterns.

### **2.4.1. Gathering Orientation Data**

Using EBSD to get spatially resolved orientation data is the first step. At many locations across the material, this method yields comprehensive maps of the crystal lattice orientation. [33]Every data point adds to a thorough representation of the crystalline structure by indicating the lattice's local orientation. The capacity of EBSD to generate high-resolution orientation data across wide regions is particularly beneficial since it enables the detection of minute variations in lattice orientation that signify the existence of dislocations. [34] In addition to highlighting areas of interest where notable deformation or misorientation takes place, these measurements also record the intrinsic structural characteristics of individual grains. [35]

### **2.4.2. Determining Lattice Curvature**

Variations in crystal orientation within a grain are strongly related to lattice curvature, a crucial element in GND density calculations. [32] Departures from the average lattice orientation indicate the presence of GNDs and can be used to describe the underlying curvature. [36]

Orientation difference vectors, which characterize the variations in lattice orientation throughout the sample, are computed to quantify these deviations. [35] Researchers can identify patterns of deformation and learn how the crystal lattice reacts to external loads by methodically mapping these orientation deviations. [37] Understanding the processes by which GNDs adapt to plastic deformation and transfer strain energy inside the material is crucial. [33]

### 2.4.3. Using the Dislocation Density Tensor

In order to connect the observed lattice curvature to the dislocation structures that accommodate it, the dislocation density tensor is essential. [33] The density and kinds of dislocations that are present, including edge and screw dislocations, are described in depth by this mathematical construct. [32] The tensor allows the accurate computation of GND density by combining contributions from different dislocation configurations. [35] In order to effectively represent the link between lattice curvature and dislocation structures, this phase requires complex computational techniques. [34] In addition to measuring the number of dislocations, the tensor provides information about their spatial distribution and the material's microstructural behaviour under various loading scenarios. [37]

### 2.4.4. Applying statistical Optimisation

For GND density calculations to be improved and their correctness guaranteed, statistical techniques are crucial. [36] The linear simplex optimization method is a frequently used technique that accurately represents the observed lattice curvature while minimizing the total dislocation content. [35] This method guarantees that the computed densities match the real dislocation arrangements in the material and have physical significance. [32] Additionally, statistical optimization reduces the possibility of mistakes brought on by assumptions in the mathematical model or noise in EBSD data. [32] Researchers can increase their confidence in their findings and produce a more accurate depiction of the material's microstructural properties by utilizing strong statistical methods. [37]

### 2.4.5. Excluding High-Angle Grain Boundaries (HAGBs)

To ensure accuracy, high-angle grain boundaries (HAGBs) are purposefully left out of GND density computations. [36] These borders, which are unrelated to GNDs, indicate a substantial misorientation between neighbouring grains. [38] To avoid overestimation and guarantee that the analysis only considers dislocations within individual grains, regions close to HAGBs are assigned a GND density of zero. [35] The idea that these borders do not add to the lattice curvature within grains is the basis for HAGBs' exclusion. [37] This phase improves the

precision of GND density calculations and offers a better comprehension of the material's deformation mechanics by separating the impacts of intra-grain dislocations. [39]

To provide a thorough understanding of dislocation structures within crystalline materials, the GND density calculation combines statistical analysis, mathematical modelling, and experimental methodologies. [32] The dislocation density tensor links dislocation structures to lattice curvature, which is analysed using orientation data from EBSD. [37] The computations are improved by statistical optimization techniques, which guarantee that they faithfully capture the microstructure of the material. [34] The analysis stays concentrated on geometrically required dislocations by eliminating HAGBs, providing important information about how dislocations accommodate deformation. [35] In addition to improving our comprehension of material behaviour, this methodical approach helps designers create materials with better mechanical qualities. [35]

## 2.5. Ultrasonic and its impact on materials

Several researches state that ultrasonic high amplitude treatments can result in a sustainable increase or decrease of the flow stress of metallic materials after. [40,41,42,43] Ultrasonic energy affects materials in two main ways: amplitude and frequency. Some studies show that temporary softening of the material is directly related to the size of the vibration. In other words, larger vibrations cause more softening. These softening effects of ultrasound are commonly referred to as the Acoustoplastic effect.[44,45] Other studies suggest that this softening is connected to the amount of energy in the ultrasonic waves. While earlier research showed little effect from frequency, more recent studies indicate that as the frequency increases, the material becomes less softened. Thus, higher frequency waves might make the material harder, rather than easier, to deform. [10,46]

The effects of UST also depend on other factors, such as the duration of treatment and the material's state, which lead to significant changes in mechanical properties and microstructure. Material hardness and strength are greatly influenced by the accumulation and rearrangement of dislocations induced by UST. [47] Studies conducted on zinc crystals by Blaha and Langenecker showed that low amplitude vibrations do not cause work hardening, while high amplitude vibrations lead to dislocation activity and microstructural transformations. [47]

The application of UST can lower the static stress required for the plastic deformation of metallic materials, thereby reducing the forming load and energy consumption. This

phenomenon is known as the acoustic softening effect. [48] Djavanroodi's research concluded that the forming load decreases as vibration frequency increases. [49] UST on aluminium alloys improves ductility. [50] UST treatment on copper during tensile testing increased yield stress. However, UST applied during testing decreased yield stress, showcasing UST's dual effect on material plasticity and strength. [51]

Study on nickel alloys using Electron Backscatter Diffraction (EBSD) revealed an increase in dislocation density and hardness after UST, with minimal effect on grain morphology but significant changes in the internal substructure. [52]. With low-amplitude vibrations, it was observed that the material retained its structure. However, if the vibrations applied were beyond a certain amplitude, there was a higher chance of material deformation. It was also observed that the material was strengthened with prolonged UST treatment, thereby proving that UST could be optimally used to control the material's microstructure and mechanical properties. [52] According to Rusinko, ultrasonic hardening occurs when the yield strength of a material increases due to the defects in the crystalline structure that are initiated and developed by acoustic energy. [53]

In this study, the effect of plastic deformation on metals was aimed to be understood by employing a nickel-based alloy.

## 2.6. Ultrasonic system

The ultrasonic vibration system in general has four main components, as illustrated schematically in Fig. 2-3 Schematic representation of an Ultrasonic vibration system&(1-Generator,2-Transducer,3-Concentrator,4-Sample).These components are the ultrasonic generator, ultrasonic transducer, concentrator, and the instrument to which the sample is attached. [54]

The process begins with the ultrasonic generator, which produces electrical oscillations. These oscillations are then transmitted to the ultrasonic transducer. The transducer plays a crucial role by converting the electrical oscillations into mechanical vibrations. To amplify these vibrations, a concentrator is employed. This device ensures that vibrations of higher amplitude are achieved, which are essential for the effectiveness of the ultrasonic treatment. [54]

Finally, the amplified mechanical vibrations are transferred to the sample attached to the instrument. This setup enables precise application of ultrasonic vibrations, which are critical for modifying the material properties under study.

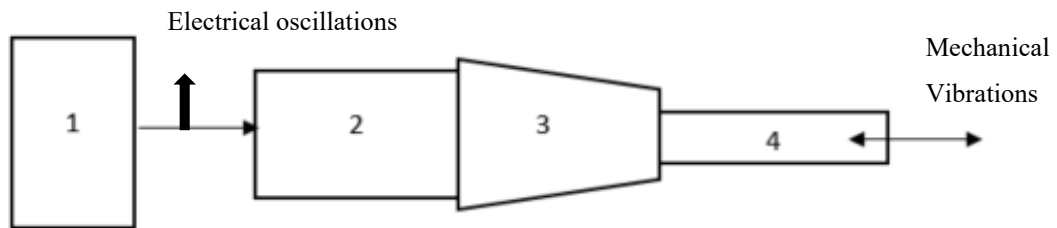


**Fig. 2-3 Schematic representation of an Ultrasonic vibration system&(1-Generator,2-Transducer,3-Concentrator,4-Sample)**

The setup utilized to apply ultrasound effects on metals at the laboratory is shown below and it follows the mechanism described in Fig. 2-4. Three samples of IN617 were used for GND analysis, and these samples were pre-treated with ultrasound at varying durations and amplitudes, as shown in the table below. No separate experimental work was conducted in this research. Each sample had four test cases, and multiple samples were analysed to ensure accurate and reliable results

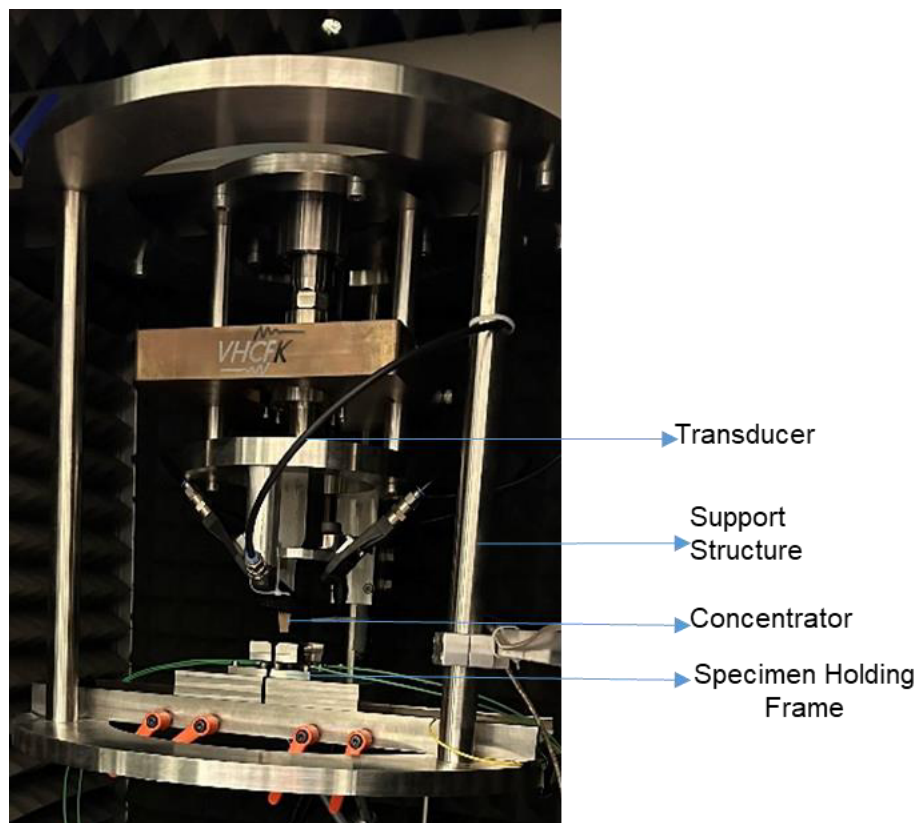


**Fig. 2-4 Ultrasonic metal testing equipment**

Sample ID	Duration in (ms)	Force in (N)	Ultrasonic amplitude in ( $\mu m$ )
N1_A	0	0	0
N2_A			
N3_A			
N1_B	0	400	0
N2_B			
N3_B			
N1_C	50	100-200	20
N2_C			
N3_C			
N1_D	5000	100-200	20
N2_D			
N3_D			

Tab. 1 List of Samples and the parameters they are tested with.

## 2.7. Role of Youngs modulus and Schmid factor in plastic deformation

This study directly addressed the relationship between Young's modulus ( $E$ ), the Schmid factor ( $m$ ), and their combined influence on resolved shear stress, particularly in anisotropic systems. [55] For plastic deformation to occur in a material, it is generally considered that the shear stress arising in the slip systems, as a result of the applied stress, must exceed the critical resolved shear stress. This critical value varies depending on the material's intrinsic properties, such as composition, crystal structure, and processing history. To delve deeper into the relationship between Young's modulus ( $E$ ) and the Schmid factor ( $m$ ) Benedikt Engel, in his research on the investigated the behaviour of a single grain subjected to stress. [55]

The fundamental equation governing this relationship is expressed as:

$$\tau_{a,res} = \sigma_a \cdot m \quad (1)$$

Here  $\tau_{a,res}$  is the resolved shear stress amplitude,  $\sigma_a$  is the applied stress amplitude,  $m$  is the Schmid factor, which depends on the grain orientation and the direction of applied stress.

When the loading condition is altered from stress-controlled to strain-controlled, the stress amplitude  $\sigma_a$  can be estimated using Hooke's law. This leads to the modified equation:

$$\tau_{a,res} = \varepsilon_{a,t} \cdot E \cdot m \quad (2)$$

$\varepsilon_{a,t}$  is the strain amplitude, assumed constant in strain-controlled loading, E is Young's modulus, m remains the Schmid factor. This formulation underscores the significance of the product  $E \cdot m$  in determining the resulting shear stress during elastic behaviour. Both E and m are influenced by the crystallographic grain orientation, while  $\varepsilon_{a,t}$  is a constant value under strain-controlled conditions. [55]

From Engel's work, it was evident that the interaction between Young's modulus and the Schmid factor played a pivotal role in understanding the mechanical behavior of materials, particularly in anisotropic systems. The main purpose of using  $E \cdot m$  as a parameter was to determine how grain orientation influenced the resulting shear stress amplitude for a given total strain amplitude. It was found that both Young's modulus (**E**) and the Schmid factor (**m**) played crucial roles in determining the resulting shear stress amplitude, which triggered local plastic deformation, as both of these values depended on the same grain orientation. [55] These parameters jointly influence the material's reaction to external loads, providing critical insights into the stress and strain distribution at the microscopic level. Such analyses are especially relevant in studying fatigue crack initiation, where localized anisotropy and deformation mechanisms dictate the material's performance. [55] Hence it was understood that  $E \cdot m$  model was considerably more accurate than the conventional methods that solely depends on the Schmid factor(m). In this research, the  $E \cdot m$  model, along with FE simulation, was used to demonstrate how the tested alloy behaved under UST.

### 3. Materials and Methodologies

#### 3.1. Scanning electron Microscope (SEM)

Scanning Electron Microscopy (SEM) is an imaging technique used to obtain high-resolution images and detailed surface information about tested samples. [56] Unlike optical microscopes, SEM uses a focused beam of electrons to scan the surface of a specimen, providing high-resolution images. [56,57] The interaction between the sample and the electron beam generates various signals, including secondary electrons (SE), backscattered electrons (BSE), and characteristic X-rays, which provide information about the sample's topography, composition, and other properties. These signals are then processed to create a grayscale image, which can be viewed on an external monitor. [56,57,58] Figure 3-1 below provides a schematic representation of the Scanning Electron Microscope, while Figure 3-2 illustrates how the sample appears on the external monitor

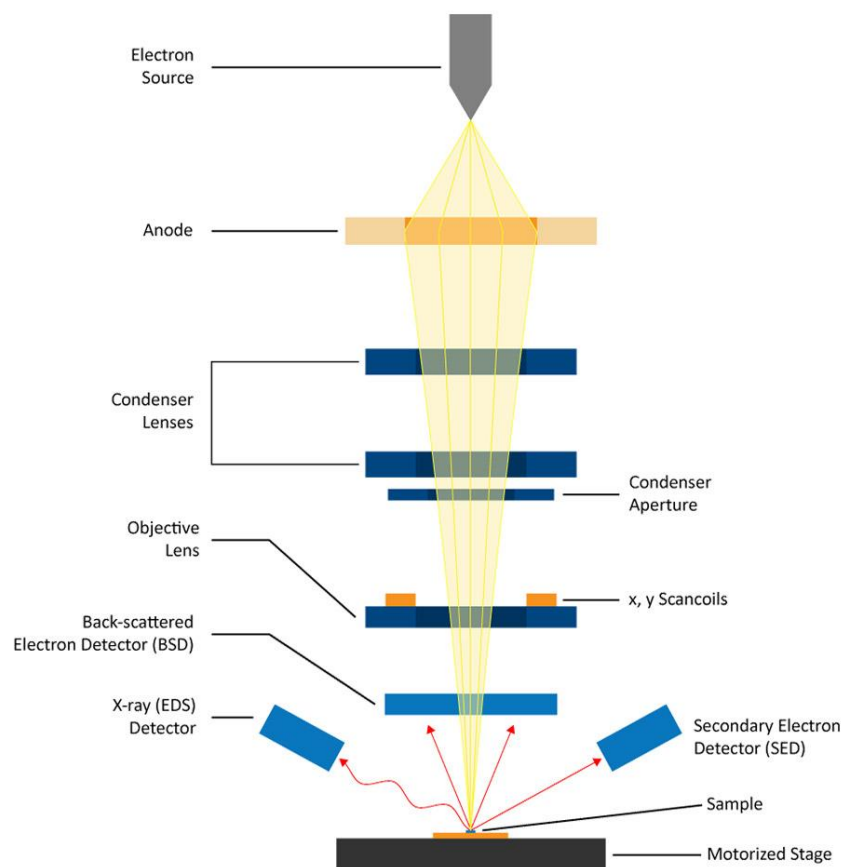


Fig. 3-1 schematic representation of Scanning electron microscope.

This research utilized FEI Quanta Scanning Electron Microscope and the Gaya Scanning Electron Microscope.

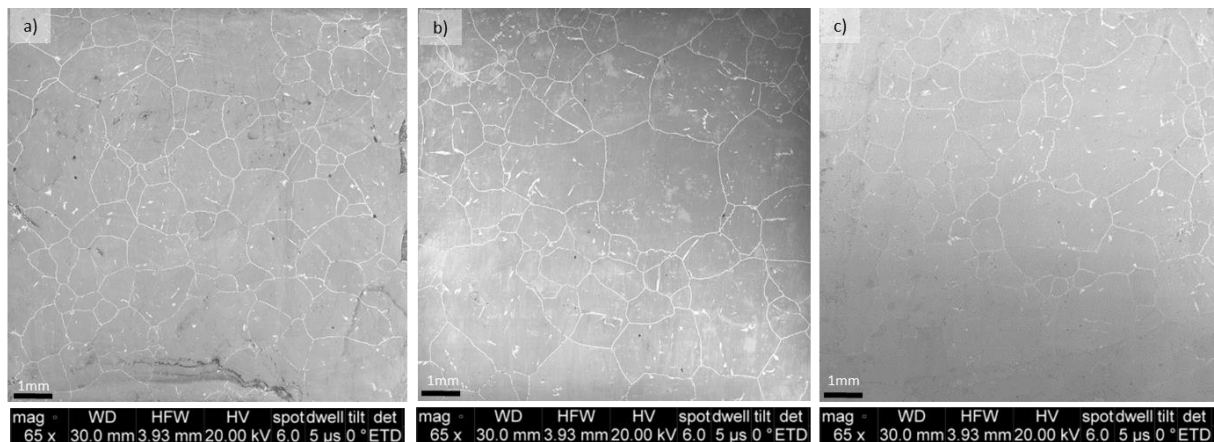


Fig. 3-2 SEM images of samples a)N1, b)N2, c)N3

The figure 3-2 provided below showcase a selection of SEM images taken from the IN617 samples that were tested and analysed in this study. These images were used to study the grain structure, phase distribution, and defects present in the material. Additionally, they provide insights into conditions such as slip bands, grain boundary movements, and material deformation.

EBSD Parameters that were employed in obtaining the SEM images shown in Fig 3-2 include the level of magnification, Working distance, High Field width, High voltage, the spot size along with dwell time and the detector type. [24] This can be understood by the table provided below.

Magnification (mag)	Working Distance(WD)	High-Field Width(HFW)	High Voltage	Spot size/Dwell time	Tilt Angle	Detector Type(DEt)
65×	30.0mm	3.93mm	20kV	6.0/5μs	0°	ETD

Tab. 2 SEM Imaging parameters

### 3.2. An Overview of Inconel 617 Alloy

The nickel-chromium-cobalt-molybdenum alloy Inconel 617 is renowned for its remarkable blend of metallurgical stability, oxidation resistance, and high-temperature strength [60,61]. Heat treatment improves corrosion resistance of the work piece surface as well as tensile and fatigue properties of the alloy. [22] Three samples of IN617 with varying dimensions of length, breadth and height were used: Sample 1 measuring 2.95mm × 2.96mm × 1.7mm, Sample 2 measuring 2.98mm × 3mm × 1.67mm, and Sample 3 measuring 3.04mm × 3.07mm × 1.66mm were used in this research. These samples were subjected to EBSD (Electron Backscatter Diffraction) measurements after different experimental conditions, including variations in step size, applied force, and time intervals as seen in Tab 1. The response of the material to these applied parameters was analysed to study critical aspects such as deformation behaviour, geometrically necessary dislocations (GND), stress, and strain.

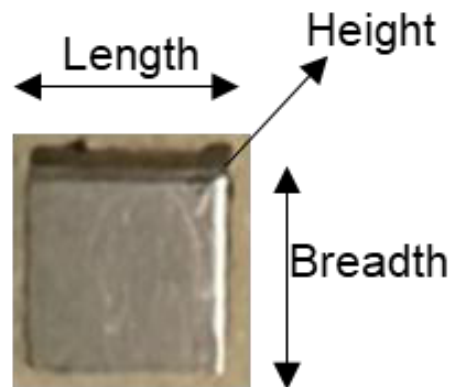


Fig. 3-3 Sample used in investigation

This comprehensive study aims to evaluate the material's performance under different external conditions, providing valuable insights into how factors like step size, force, and time affect its microstructural properties. By analysing the material's behaviour, a better understanding of the relationship between external parameters and the resultant changes in its structural and mechanical characteristics was obtained. Inconel 617 is composed of nickel (44.5–61%), chromium (20–24%), cobalt (10–15%), and molybdenum (8–10%), along with minor amounts of aluminium, carbon, iron, and titanium. [18,61] This alloy offers an exceptional balance of mechanical strength and resistance to environmental degradation. Nickel present in the alloy provides strength at high temperatures and resistance to corrosive substances. [18] By creating a thin, sticky oxide layer that protects the surface, chromium increases the material's resistance to oxidation. [63] Molybdenum helps with resistance to pitting and crevice corrosion, which is important in tough industrial environments, while cobalt offers thermal stability and high-

temperature strength. [63] Inconel 617 has a face-centred cubic (FCC) austenitic matrix in its microstructure. Some key properties of this alloy include high-temperature strength, as it maintains structural stability at elevated temperatures. [61,64] It is also resistant to oxidation and corrosion, even in environments containing high sulphur or other aggressive elements. [18,63] Due to its excellent machinability and weldability, it is used for manufacturing complex components. [64] Additionally, the alloy exhibits remarkable long-term stability. [60,63] Despite its advantages, Inconel 617 has certain drawbacks, such as its high cost, primarily due to its nickel and cobalt content. Additionally, the alloy requires careful fabrication to prevent issues like improper grain structure formation or welding defects.

### 3.3. Softwares used

All the software tools discussed here were used in FE modelling, and an overview of these tools is presented in this section. Their applications and results will be explored in the upcoming section. MATLAB 2024b, MTEX, and MTEXGmsh were used to import the EBSD data provided in.ang format. MTEX tool was used to extract the crystallographic orientation information and also for assigning orientation dependent material properties which were later utilized for FEM modelling. MTEX×Gmsh was used to convert the processed EBSD data into a mesh suitable for simulations. This processed data is then imported into GMSH for creating a 3D mesh. In this research Origin was used to plot Young's modulus ( $E$ ), the Schmid factor ( $m$ ), and the product of Young's modulus and the Schmid factor ( $E \cdot m$ ) which was used to study the material deformation behaviour. Python programming language was used to assign crystal orientation to the file that was exported from GMSH. Finally Dassault Simulia Abaqus 2024 was used to perform FEM analysis and also plastic strain, resulting shear stress, von Mises stress, and several other quantities can be plotted using this tool, which was used to study the material's deformation behaviour, failure mechanisms, and response under different loading conditions, providing insights into how microstructure, such as grain size and orientation, influences macroscopic mechanical properties. Practical application of all these tools can be understood by referring Appendix. [65,66,67,68,69]

### 3.4. Measurement of EBSD data

Specimen preparation is a crucial step in obtaining precise and high-quality EBSD (Electron Backscatter Diffraction) data. This ensures accurate and optimal electron diffraction and minimizes any irregularities that can interfere with data collection. Properly prepared

specimens allow for effective interaction between the electron beam and the material, producing high-resolution diffraction patterns. [25]

Data acquisition in EBSD involves directing an electron beam onto the prepared specimen's surface. The specimen to be analysed is mounted at an angle of  $70^\circ$  on the mounting table. When the beam interacts with the crystal lattice of the material, it undergoes diffraction. The diffracted electrons are then projected onto a phosphor screen, where they form distinct patterns. These patterns, known as electron channelling patterns (ECP), are characteristic of the crystal orientation and structure of the specimen. Some scanning electron microscopes (SEM) are equipped with detectors capable of capturing these ECPs, which are subsequently processed to generate EBSD data. [25]

As illustrated schematically in Fig. 3-4 Schematic representation of electron beam, specimen and phosphor screen [70], the diffraction of electrons from the sample surface plays a central role in the EBSD process. The captured patterns are analysed to extract detailed information about the material's microstructure, such as grain orientation, phase distribution, and dislocation density. [25]

By adhering to a thorough preparation protocol and utilizing advanced detection systems, researchers can ensure that the EBSD measurements are both accurate and reproducible.

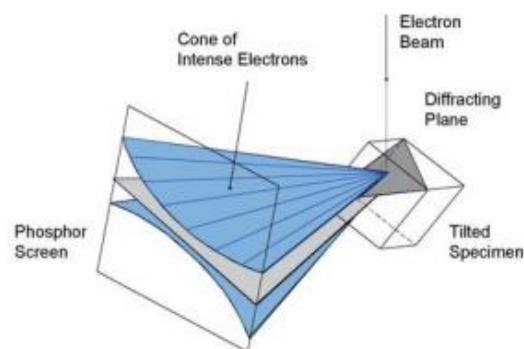


Fig. 3-4 Schematic representation of electron beam, specimen and phosphor screen [70]

Metals with higher purity levels generally require significantly more time to prepare compared to alloys. This is because pure metals are often more sensitive to damage during the preparation stages. [54]

Sectioning is one of the most important and difficult processes in the preparation process. Improper sectioning can cause damage to the sample, and this risk is notably higher for face-

centred cubic (FCC) metals compared to body-centred cubic (BCC) metals, due to the structural properties of FCC materials FCC metals have a higher tendency to deform under stress due to the presence of an increased number of slip systems. Additionally, their lower hardness makes them more susceptible to damage during sectioning. Precision saws with thin, abrasive blades are frequently used to reduce damage. Because they use less force when cutting, these tools are less likely to introduce flaws. The metal surface must be kept as damage-free as possible, which requires careful machine and blade selection. Fig. 3-5 Damage from sectioning IN617 alloy. and Fig. 3-6 Damage on the surface due to polishing of IN617 alloy provide an illustrative overview of the types of damage that can occur during the sectioning process. Such damage can compromise the quality of the subsequent steps, such as grinding and polishing, and ultimately affect the accuracy of the data obtained during EBSD analysis. [59]

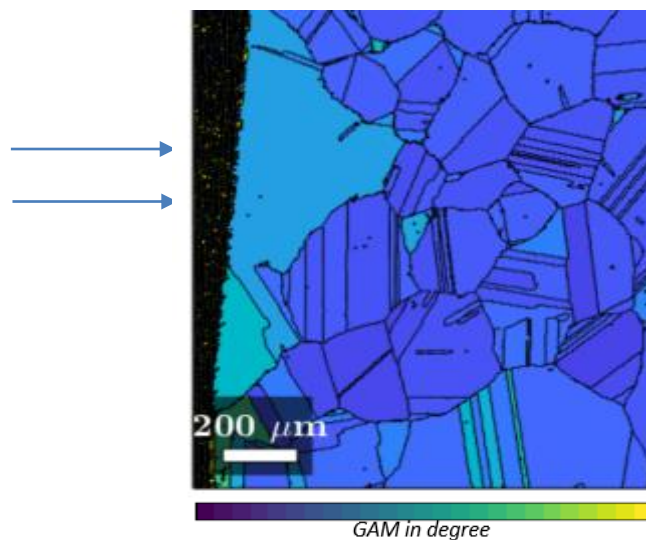


Fig. 3-5 Damage from sectioning IN617 alloy.

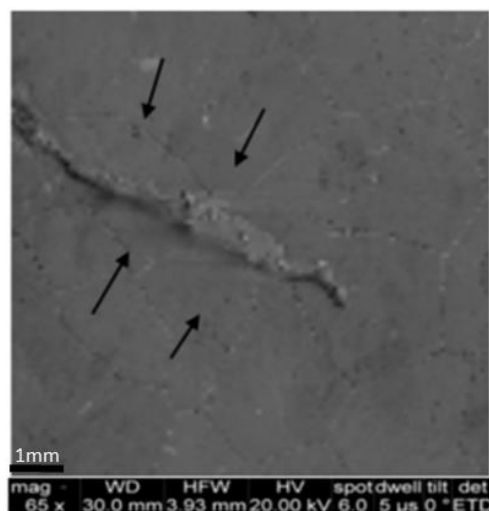


Fig. 3-6 Damage on the surface due to polishing of IN617 alloy

Materials such as silk, nylon, or specialty pads are used for polishing, as they apply less force when in contact with the material. This guarantees a surface that is damage-free and smooth, which is essential for producing precise and superior EBSD data. [71,72]

Electron backscatter diffraction (EBSD) data can only be accurate and dependable when the surface is flawless. Three to five distinct procedures are usually involved in preparing a metal or alloy for EBSD, and each is essential to the accuracy of the data. [71,72]

### 3.5. EBSD Data to FEM model

A Finite Element Model (FEM) was created utilizing information taken from an Electron Backscatter Diffraction (EBSD) investigation in order to provide a visual depiction of material deformation. This modelling method offers important insights into the possible deformation of a material under particular circumstances. But generating a FEM from EBSD data requires a number of painstaking procedures and the combination of several software programs.

The MTEX toolbox, a specialized tool for analysing and visualizing crystallographic data, was used in conjunction with the MATLAB platform to start the process. [68] Furthermore, the MTEX2Gmsh add-on was used to make it easier to convert EBSD data into a format that works with the cutting-edge mesh generating program GMSH. To produce precise, high-quality meshes that form the basis of the FEM, the most recent version of GMSH was necessary. [66] The flexible programming language Python 3.6.0 was utilized for automation and scripting in order to efficiently handle and analyse big datasets. The produced mesh was then loaded into Dassault Simulia Abaqus 2024, a powerful finite element analysis (FEA) software suite. [65] Researchers can forecast how dislocations and other microstructural characteristics affect material performance under varied loading situations because to Abaqus's ability to simulate deformation behaviour in great detail. Creating a finite element model from EBSD data was a complex procedure that calls for knowledge of programming, crystallography, and simulation tools. A thorough grasp of material deformation at the microstructural level can be attained by researchers by utilizing programs like MATLAB, MTEX, GMSH, Python, and Abaqus.

The MTEX toolbox in MATLAB was used to extract the Electron Backscatter Diffraction (EBSD) data used in simulations from a .ang file. To guarantee reliable and clean data for additional analysis, this procedure consists of a number of successive processes. In order to correctly align the crystal orientations with the specimen geometry, reference frames are first chosen, such as the specimen reference frame and the crystal reference frame. This phase lays the groundwork for successfully interpreting EBSD data.

The indexing procedure starts when the raw EBSD data is extracted. By recognizing and arranging the grain orientations, this procedure makes it possible to clearly depict the material's microstructure which can be understood by Fig. 3-7 Recalculated Microstructure provided below. In order to accurately depict the material microstructure, the next step was to compute the grain geometry. Accuracy may be hampered by specific gaps or unindexed locations that may arise during this process. A grain-filling process was used to handle these disparities, guaranteeing that any missing or ill-defined areas are fixed. Grain boundaries are also flattened to get rid of any sharp edges or abnormalities that can interfere with the computational model. The orientations are transformed into Euler angles, a mathematical representation of crystal orientations in three dimensions, after the grains have been indexed and polished. In order to connect a grain's orientation with its spatial geometry, each grain was given a unique Grain ID. Grain geometries and orientations that have been recalculated are exported to a geometry file in the .geo format. All of the orientation and spatial information needed for later meshing was included in this file.

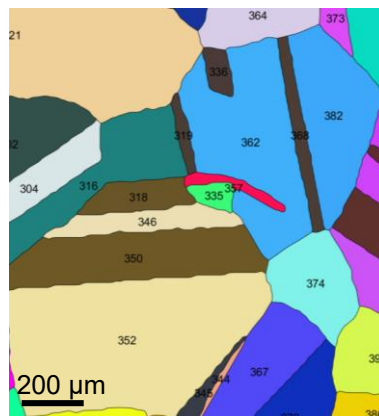


**Fig. 3-7 Recalculated Microstructure**

A high-quality computational mesh was then produced by importing the .geo file into the meshing program GMSH as seen in Fig. 3-8 Mesh obtained from GMSH software. Since the precision and dependability of the simulation results are greatly impacted by the mesh's quality, meshing is an essential step. After that, GMSH exports the meshed geometry as an input file in the .inp format that can be used with the Abaqus simulation program. To ensure accuracy, crystal orientations are assigned to each grains in the exported .inp file using a Python script. By doing this, the orientations are guaranteed to be constant and in line with the initial EBSD data. After that, Abaqus imports the improved input file for simulation which is given in Fig. 3-9 Abaqus file with added material properties and boundary conditions

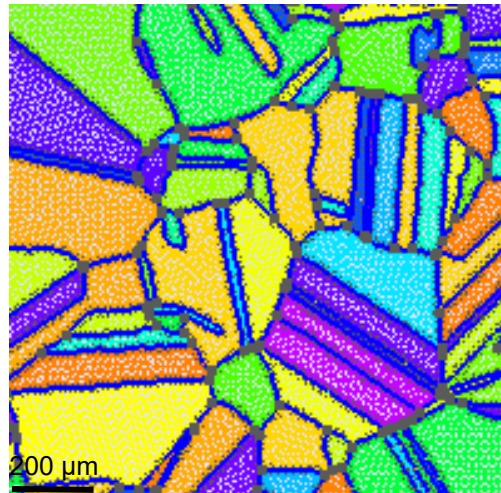


Fig. 3-8 Mesh obtained from GMSH software

To improve the accuracy of the simulation, Abaqus incorporates material features unique to the nickel alloy under study, such as IN617.

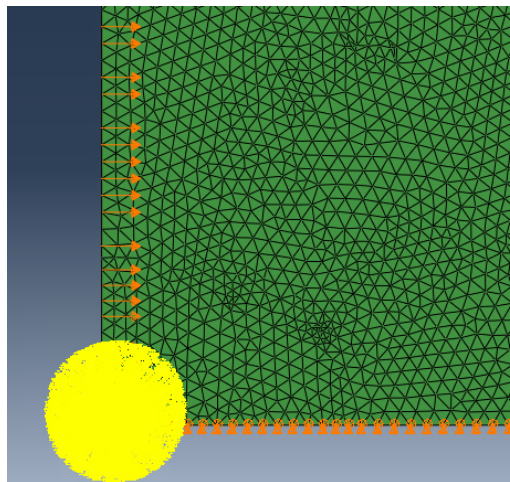


Fig. 3-9 Abaqus file with added material properties and boundary conditions

These characteristics, which come from the body of existing research, include density, stiffness matrix, yield stress, and strain values. Accurately simulating the behaviour of the material under applied stresses or strains requires these parameters.

The density of IN617 was considered to be  $8.5 \text{ g/cm}^3$ . For a face-centred cubic (FCC) material like IN617, the stiffness matrix is presented in the following format:

$$C = \begin{bmatrix} C_{11} & C_{12} & C_{12} & 0 & 0 & 0 \\ C_{12} & C_{11} & C_{12} & 0 & 0 & 0 \\ C_{12} & C_{12} & C_{11} & 0 & 0 & 0 \\ 0 & 0 & 0 & C_{44} & 0 & 0 \\ 0 & 0 & 0 & 0 & C_{44} & 0 \\ 0 & 0 & 0 & 0 & 0 & C_{44} \end{bmatrix}$$

The values used for stiffness matrix in our FEM simulation is

$$C = \begin{bmatrix} 280274 & 190988 & 190988 & 0 & 0 & 0 \\ 190988 & 280274 & 190988 & 0 & 0 & 0 \\ 190988 & 190988 & 280274 & 0 & 0 & 0 \\ 0 & 0 & 0 & 127064 & 0 & 0 \\ 0 & 0 & 0 & 0 & 127064 & 0 \\ 0 & 0 & 0 & 0 & 0 & 127064 \end{bmatrix}$$

The value of Yield stress and plastic strain used are

	Yield stress	Plastic strain
1	300	0
2	400	0.0053
3	470	0.02
4	500	0.03
5	820	0.53

**Tab. 3 Yield stress and plastic strain**

Manual to perform EBSD to FEM modelling is attached in Appendix.

### 3.6. GND density Analysis

Three samples of IN617 alloy were subjected systematically to a series of controlled tests in order to study the behaviour of GND (Geometrically Necessary Dislocation) density with varying external conditions. The tests started with an initial exploration of the samples in their original, as-received state, which was used as a control for direct comparison. This was followed by incremental application of an increasing level of mechanical force to a maximum load of approximately 400N. In the subsequent phase of testing, the samples were subjected to mechanical force of approximately 200N in conjunction with ultrasound of 20µm for a brief duration of approximately 50ms. In the subsequent phase, the samples were subjected once more to the identical level of force but in conjunction with ultrasound of 20µm for an extended duration of approximately 5000ms. Throughout these experimental tests, EBSD (Electron

Backscatter Diffraction) measurements were appropriately taken and analysed systematically in order to study the evolution and behaviour of GND density under different conditions. Another series of tests was also performed with a view to analysing the behaviour and mechanical properties of the material independently of EBSD measurements. However, for the purpose of this study, only the first four tests were selected and incorporated for detailed analysis and discussion.

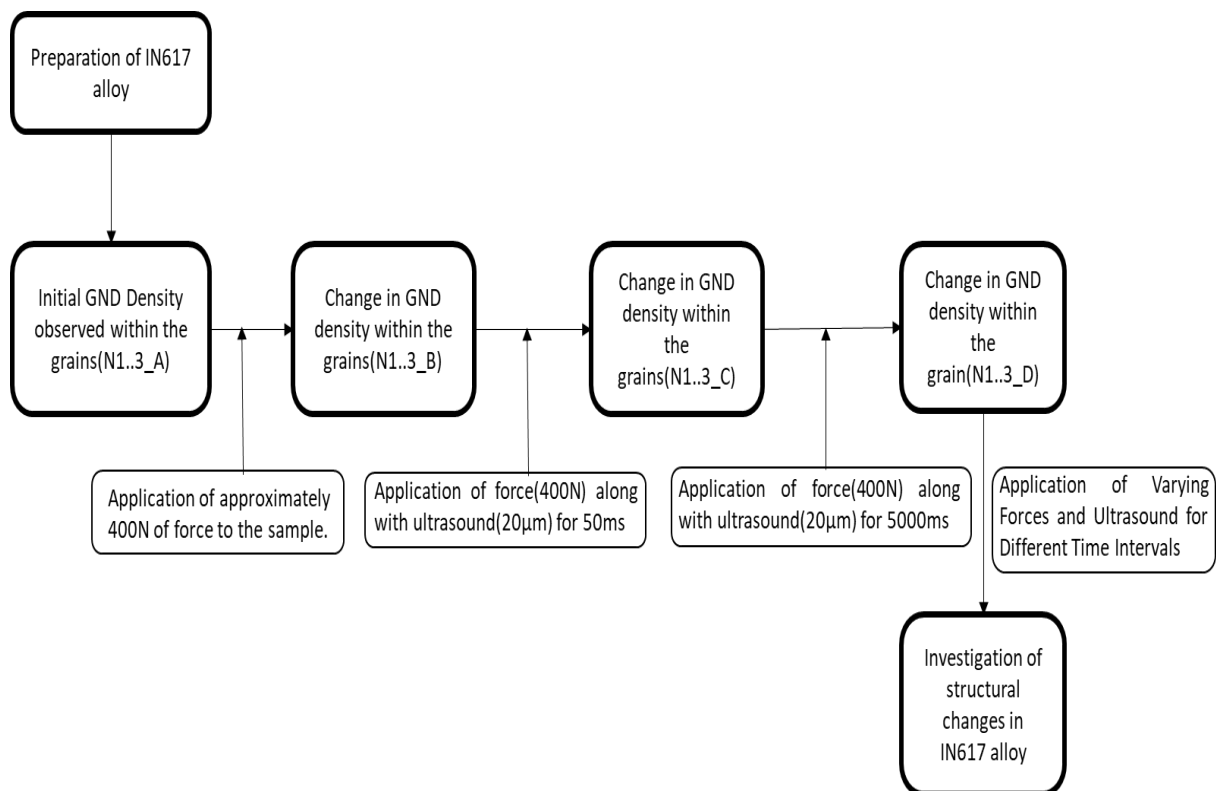


**Fig. 3-10 Experimental Procedure for Analysing GND Density Evolution in IN617 Alloy Under Mechanical and Ultrasonic Conditions**

Out of all the grains in the samples, particular grains were chosen for further examination. These grains were selected in order to provide a more thorough knowledge of the evolution of GND (Geometrically Necessary Dislocation) density because of their unique structural reactions to applied force and ultrasound. By concentrating on these grains, the research offers important new information about the processes controlling material rearrangement, stress relaxation, and dislocation behaviour under various circumstances. A more sophisticated and methodical approach to comprehending the impact of mechanical and acoustic interactions on the microstructure of the IN617 alloy is made possible by the in-depth investigations of these particular grains.

## 4. Results

### Sample 1 (N1)

Beyond evaluating the variations in GND density, several other essential mechanical properties were analysed to achieve a more comprehensive understanding of the material's deformation behaviour. These key properties included Young's modulus, the product of Young's modulus and the Schmid factor ( $E \cdot m$ ), the resulting shear stress, and the total strain, as illustrated in Figure 4-1.

To ensure a comprehensive understanding of these effects, several distinct grains that exhibited noticeable GND density patterns were carefully selected for further detailed study. This thorough investigation provides valuable insights into how the material responds to different loading and ultrasonic conditions, shedding light on its mechanical and microstructural evolution

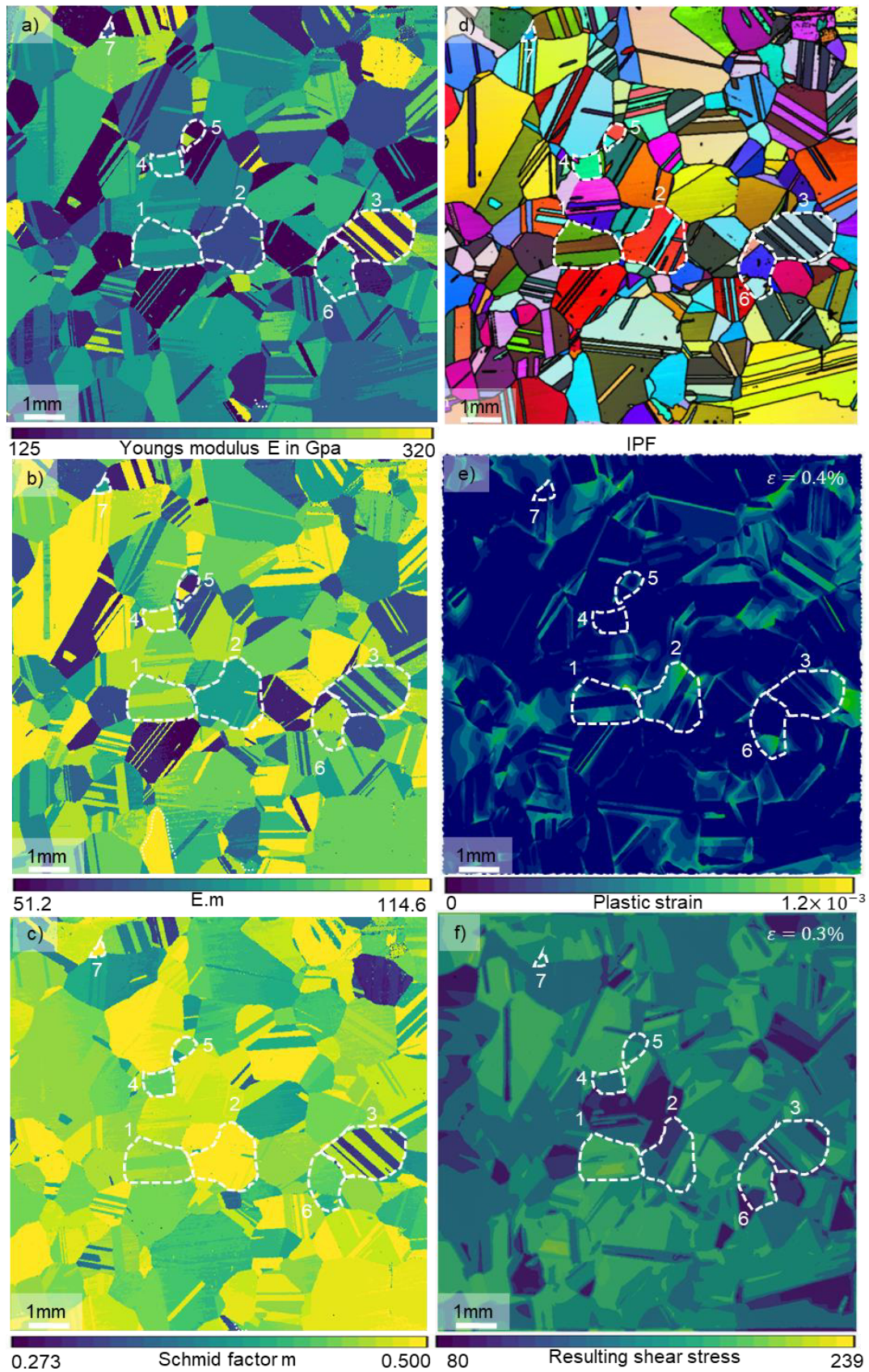


Fig. 4-1 a) Youngs modulus E in GPa, b) Product of Youngs Modulus and Schmid factor ( $E \cdot m$ ) in GPa, c) Schmid factor, d) IPF(Inverse Pole figure), e) Plastic strain, f) Resulting shear stress in MPa

All the grains that are analysed and discussed in the following sections have been carefully examined from Sample N1. The overall GND density map for Sample N1 is provided below.

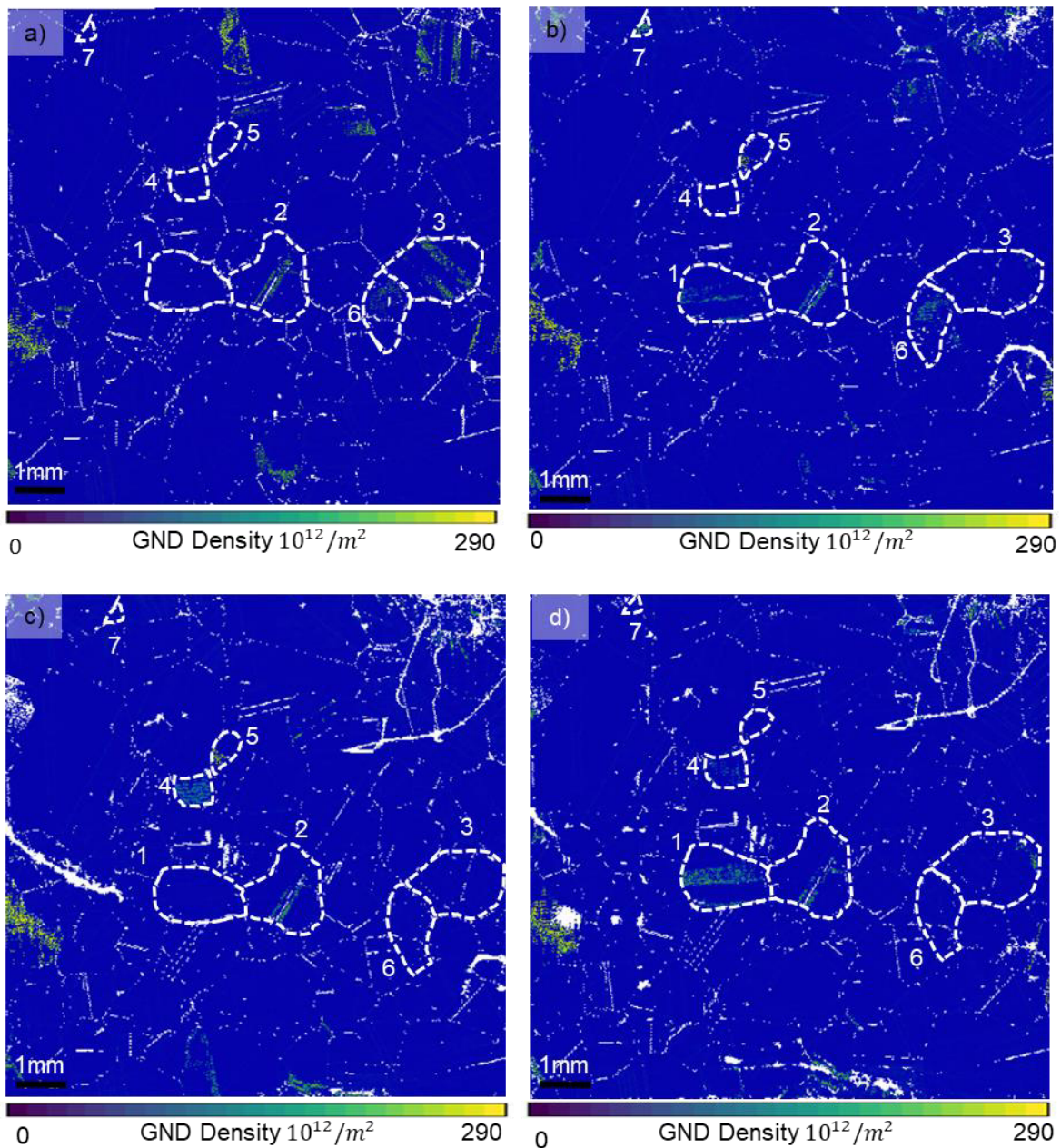


Fig. 4-2 GND density maps for all tests conducted on Sample N1: (a) N1\_A (initial), (b) N1\_B (only Force 400N), (c) N1\_C (20µm, ~100-200N, 50ms) and (d) N1\_D (20µm, ~100-200N, 5000ms).

Grain 1 initially did not show any GND density, as seen in Fig. 4-3b. Upon applying force, GND density was observed in Fig. 4-3c, indicating a structural response to the applied stress. When ultrasound was introduced along with force for a short duration, the GND density was not seen, as shown in Fig. 4-3d, suggesting a redistribution of dislocations. However, with sonication for 5000ms, the GND density was seen again as illustrated in Fig. 4-3e. Regarding

mechanical properties, Grain 1 of sample N1 exhibited a very high Young's modulus, as depicted in Fig. 4-1a, along with a correspondingly high value of  $E \cdot m$ , as seen in Fig. 4-1b. This grain appeared to have a moderate Schmid factor. It suggests an intermediate tendency for slip activation under loading as seen in Fig. 4-1c. The presence of slip bands in the plastic strain distribution, observed in Fig. 4-1e, suggests that the grain has undergone slip or has the potential for plastic deformation. Additionally, Fig. 4-1f reveals that resulting shear stress remains homogeneously distributed at a high magnitude throughout the grain, reinforcing the likelihood of plastic deformation.

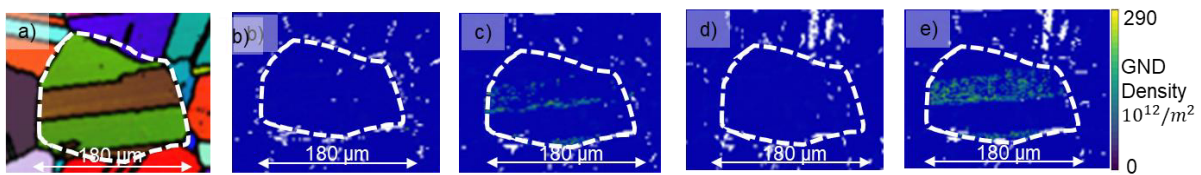


Fig. 4-3 a) IPF (Inverse pole figure) and evolution of GND Density in Grain 1 b) N1\_A (initial), c) N1\_B (only Force 400N), d) N1\_C (20 $\mu$ m, ~100-200N, 50ms), e) N1\_D (20 $\mu$ m, ~100-200N, 5000ms).

Grain 2 showed GND density concentrated along the middle of the grain, as depicted in Fig. 4-4b. The application of force alone did not alter this distribution, as seen in Fig. 4-4c. Similarly, introducing ultrasound for a short time did not cause any visible change in the GND density along the grain's middle, as observed in Fig. 4-4d. Even when ultrasound was applied for an extended duration of 5000ms, the GND density remained unchanged in Fig. 4-4e. When mechanical properties were taken into consideration, it was understood that Grain 2 had a moderate Young's modulus, as shown in Fig. 4-1a, and a similarly moderate  $E \cdot m$  value, as observed in Fig. 4-1b. From Fig. 4-1c it was seen that the grain had relatively high Schmid factor( $m$ ). It is more likely to experience plastic deformation when stress is applied. The plastic strain distribution, seen in Fig. 4-1e, revealed areas of both high and low strain, indicated by lighter and darker regions, respectively. This contrast suggests strain localization within the grain. The shear stress distribution in Fig. 4-1f was heterogeneous, demonstrating the influence of neighbouring grains and the presence of regions with high slip activity.

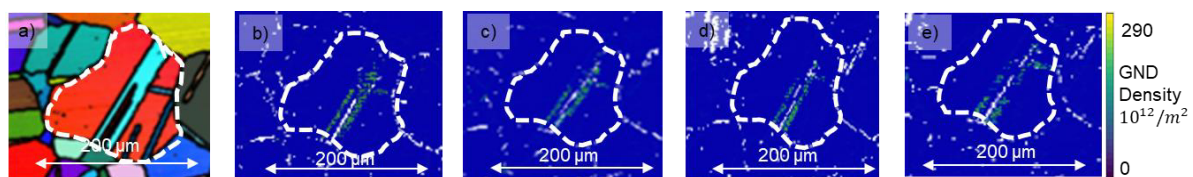
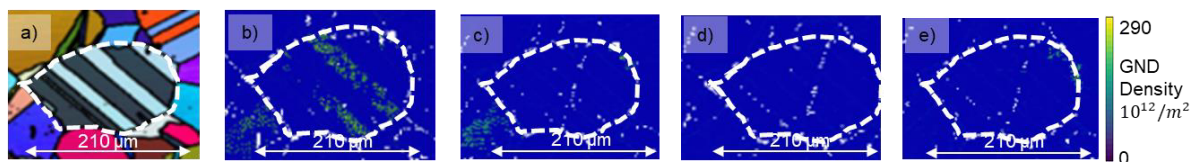


Fig. 4-4 a) IPF(Inverse pole figure) and Evolution of GND Density in Grain 2 b) N1\_A(initial), c) N1\_B(only Force 400N), d) N1\_C(20 $\mu$ m, ~100-200N, 50ms), e) N1\_D(20 $\mu$ m, ~100-200N, 5000ms).

Grain 3 had initial GND density, evident in Fig. 4-5b. When only force was applied, the GND was not seen, as observed in Fig. 4-5c. This state of GND density remained unchanged when ultrasound was applied for a short time, as shown in Fig. 4-5d, meaning the grain structure had stabilized in response to the applied force. However, with sonication(5000ms) exposure, the GND density was seen along the grain edges, as observed in Fig. 4-5e, indicating that extended exposure to ultrasound promoted localized reorganization of dislocations. Grain 3 showed the presence of slip bands, which may indicate plastic deformation or stress variations within the grain. This grain demonstrated both extremely high and low values of Young's modulus, as depicted in Fig. 4-1a. The alternating values of  $E \cdot m$  in Fig. 4-1b suggest heterogeneous deformation behaviour, with some regions showing higher susceptibility to slip while others resist deformation. Varying Schmid factor can be seen in Fig. 4-1c. The plastic strain distribution in Fig. 4-1e further supports the idea of slip activity, and regions of high shear stress, as shown in Fig. 4-1f.



**Fig. 4-5** a) IPF (Inverse pole figure) and evolution of GND Density in Grain 3 b) N1\_A (initial), c) N1\_B (only Force 400N), d) N1\_C (20 $\mu$ m, ~100-200N, 50ms), e) N1\_D (20 $\mu$ m, ~100-200N, 5000ms).

Grain 4, being smaller than the previous grains, exhibited distinct behaviour. Initially, no GND density was seen, as shown in Fig. 4-6b. The application of force alone did not alter this state, as confirmed in Fig. 4-6c. However, when ultrasound was applied for a short time, GND density was observed in Fig. 4-6d, suggesting that the vibrational energy annihilates it. With sonication for about 5000ms, the density was greatly reduced, as shown in Fig. 4-6e, implying that an extended duration facilitates partial relaxation and redistribution of dislocations. With respect to properties such as Young's modulus, the product of Young's modulus and the Schmid factor ( $E \cdot m$ ), resulting shear stress (RSS), and plastic strain across all the grains, several key observations were made. Grain 4, as seen in Fig. 4-1a, possessed a moderate Young's modulus and a high  $E \cdot m$  value, as indicated in Fig. 4-1b. This grain had a moderate Schmid factor, leading to an intermediate response to applied stress which can be seen in Fig. 4-1c. Unlike other grains, it showed no signs of plastic strain, as confirmed in Fig. 4-1e. The shear stress

distribution in Fig. 4-1f was homogeneous and comparatively low, suggesting that this grain remained largely unaffected by applied stresses and external influences.

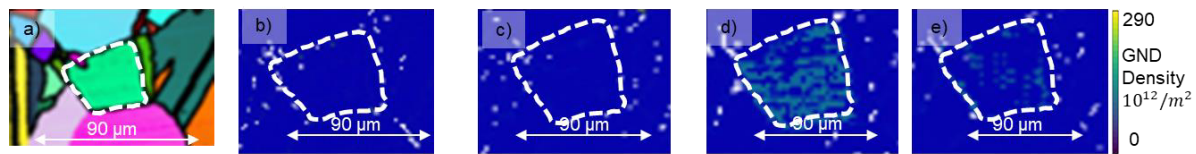


**Fig. 4-6** a) IPF (Inverse pole figure) and evolution of GND Density in Grain 4 b) N1\_A (initial), c) N1\_B (only Force 400N), d) N1\_C (20 $\mu$ m, ~100-200N, 50ms), e) N1\_D (20 $\mu$ m, ~100-200N, 5000ms).

Grain 5, despite its smaller size, demonstrated unique responses. Initially, it exhibited very minimal presence of GND density, as seen in Fig. 4-7b. With the application of force, the GND density was more prominent, as shown in Fig. 4-7c. The introduction of ultrasound for a short time maintained the GND density, as seen in Fig. 4-7d. However, with prolonged ultrasound exposure, the GND density completely diminished, as observed in Fig. 4-7e, indicating that the sustained vibrations facilitated complete relaxation and rearrangement of the internal structure. Grain 5, on the other hand, exhibited high values of both Young's modulus and  $E \cdot m$ , as shown in Figs. 4-1a and 4-1b. Schmid factor ( $m$ ) lied within the moderate range as seen in Fig. 4-1c. The plastic strain distribution in Fig. 4-1e presented a mix of high and low strain regions, with lighter areas indicating significant strain accumulation and darker areas showing lower strain. This suggests localized deformation and potential slip activity. Furthermore, the grain exhibited high RSS, as seen in Fig. 4-1f, reinforcing the idea that plastic deformation had taken place.

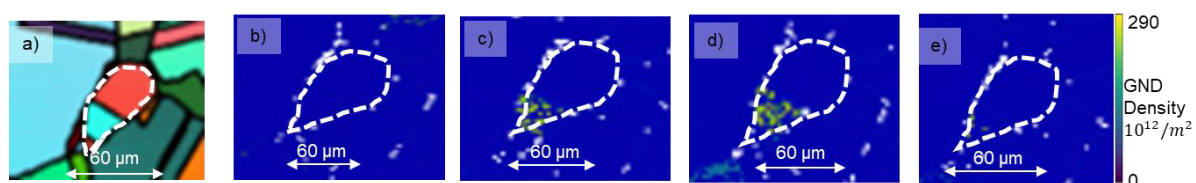


**Fig. 4-7** a) IPF (Inverse pole figure) and evolution of GND Density in Grain 5 b) N1\_A (initial), c) N1\_B (only Force 400N), d) N1\_C (20 $\mu$ m, ~100-200N, 50ms), e) N1\_D (20 $\mu$ m, ~100-200N, 5000ms).

Grain 6 behaved similarly to Grain 3, showing comparable responses to the applied conditions. Initially, it had GND density, as seen in Fig. 4-8b. When force was applied, the GND density become more visible, as shown in Fig. 4-8c, meaning the grain continued to accumulate dislocations under mechanical stress. With ultrasound applied for a short time, the density got was barely seen, as noted in Fig. 4-8d. Finally, with prolonged ultrasound exposure, the GND

density was completely removed, as seen in Fig. 4-8e, assuming that the accumulated dislocations have been fully relaxed and redistributed. Grain 6 shares similarities with Grain 3, demonstrating a high Young's modulus and a correspondingly high  $E \cdot m$  value, as evident in Figs. 4-1a and 4-1b. This grain had relatively high Schmid factor with some variation, experiencing localized slip under applied stress as seen in Fig. 4-1c. The plastic strain, as shown in Fig. 4-1e, remained very low, suggesting limited deformation. However, the high  $E \cdot m$  values and the elevated RSS observed in Fig. 4-1f indicated that the grain may have undergone plastic deformation, possibly in response to external stress.

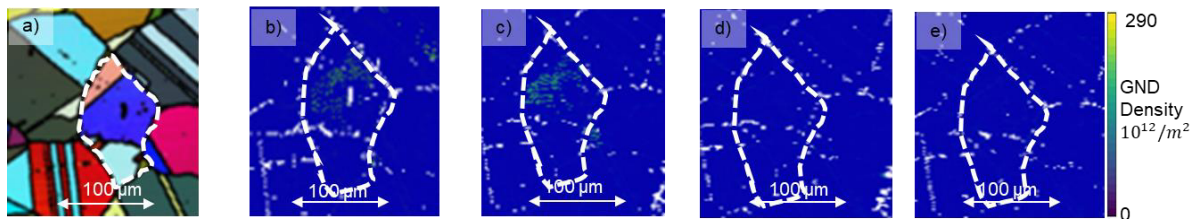


Fig. 4-8 a) IPF (Inverse pole figure) and evolution of GND Density in Grain 6 b) N1\_A (initial), c) N1\_B (only Force 400N), d) N1\_C (20 $\mu$ m, ~100-200N, 50ms), e) N1\_D (20 $\mu$ m, ~100-200N, 5000ms).

Lastly, Grain 7, the smallest among the studied grains, also exhibited distinct patterns. Initially, no GND density was observed, as shown in Fig. 4-9b, indicating a stress-free starting point. With applied force, GND density was seen, as observed in Fig. 4-9c. When ultrasound was introduced for a short time, the density returned to zero, as seen in Fig. 4-9d. With prolonged ultrasound exposure, the density observed was very minimal, nearly non-existent, as shown in Fig. 4-9e. Finally, considering the mechanical properties, Grain 7, as depicted in Fig. 4-1a, exhibited a low Young's modulus, while its  $E \cdot m$  value remained high, as shown in Fig. 4-1b. From Fig. 4-1c it was confirmed that the grain had low Schmid factor. The absence of plastic strain in this grain, confirmed by Fig. 4-1e, suggests that it did not experience significant deformation. Nevertheless, the shear stress distribution in Fig. 4-1f was uniform and relatively high, indicating that the grain had potential for plastic deformation under increased stress.

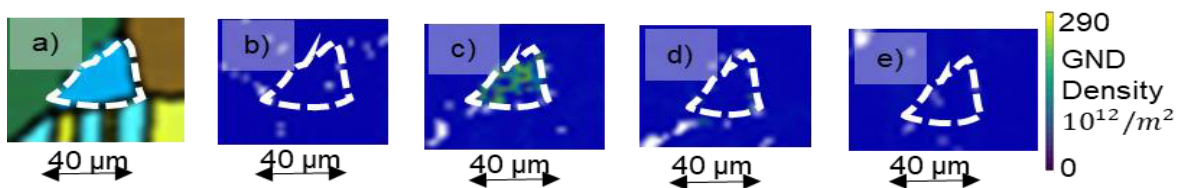
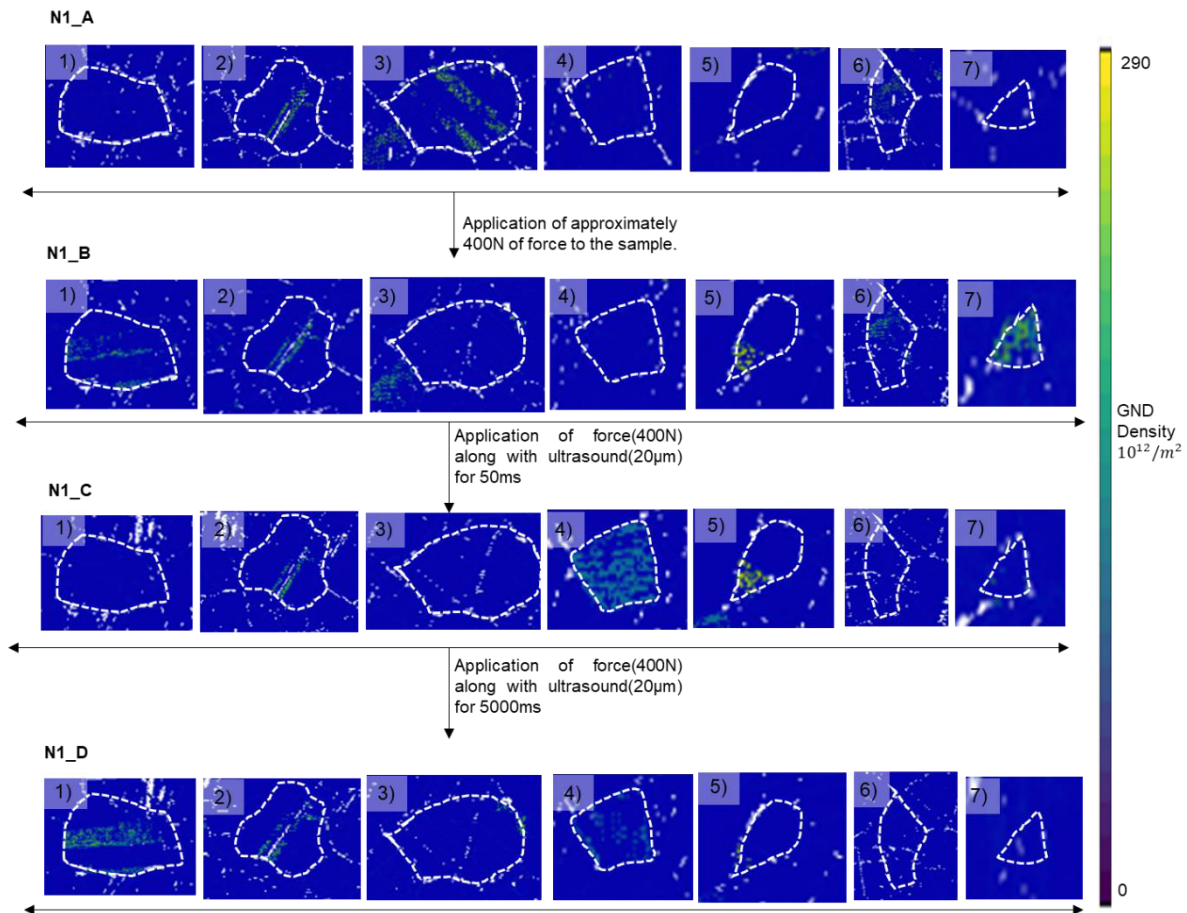


Fig. 4-9 a) IPF (Inverse pole figure) and evolution of GND Density in Grain 7 b) N1\_A (initial), c) N1\_B (only Force 400N), d) N1\_C (20 $\mu$ m, ~100-200N, 50ms), e) N1\_D (20 $\mu$ m, ~100-200N, 5000ms).

The schematic diagram illustrates the evolution of GND (Geometrically Necessary Dislocation) density in different grains under varying conditions: initial state, applied force, force with short ultrasound exposure, and force with prolonged ultrasound exposure. The schematic highlights the distinct behaviours of grains under mechanical stress and ultrasound, demonstrating how structural characteristics influence dislocation movement, relaxation, and accumulation.



**Fig. 4-10 Evolution of GND Density in IN617 Alloy Grains Under Mechanical and Ultrasonic Conditions for sample N1**

From this analysis, it was understood how different grains in the material responded to applied force and ultrasound over time, revealing crucial aspects of material deformation behaviour. The varying responses across different grains highlight the role of grain size, initial GND density, and external conditions in influencing dislocation movement and structural rearrangement.

A key takeaway is that some grains, such as Grain 1 and Grain 5, showed GND density when force was applied but experience significant relaxation when exposed to prolonged ultrasound,

indicating that vibration induced can effectively redistribute or remove dislocations. This suggests that ultrasound can play a crucial role in stress relaxation and dislocation movement, potentially aiding in the reduction of localized strain. Grains like Grain 2 exhibited prominent GND density that remained unchanged despite force and ultrasound application, implying a structural resistance to deformation. This suggests that certain grains may have inherent stability due to their orientation, internal composition, or interaction with neighbouring grains, making them less susceptible to external modifications. Grains 3 and 6 demonstrated an interesting phenomenon where GND density first becomes was not seen under force alone but reappeared along the edges with prolonged ultrasound application. This indicates that while stress relaxation occurs initially, sustained vibrational energy may lead to localized accumulation or redistribution of dislocations, potentially due to grain boundary interactions or internal stress concentrations. The smallest grains, such as Grain 7, showed minimal resistance to deformation, with GND density seen was seen under force but was not observed when exposed to ultrasound. This suggests that smaller grains may be more adaptable to external influences, with dislocations readily forming and dissipating based on applied conditions. Overall, these results provide valuable insights into how different grains within the material respond to mechanical and vibrational influences.

Several key observations can be made regarding the Young's modulus, the product of Young's modulus and the Schmid factor ( $E \cdot m$ ), Schmid factor ( $m$ ), the resulting shear stress (RSS), and the plastic strain across all the grains. This grain analysis provides valuable insights into the mechanical behaviour of the material under applied stress. Grains with a high Young's modulus, such as Grain 1, Grain 5, and Grain 6, exhibited a correspondingly high  $E \cdot m$  value, indicating significant internal stresses and a strong susceptibility to plastic deformation when subjected to sufficient loading. In contrast, grains with a lower Young's modulus, such as Grain 7, demonstrated limited plastic strain, though the high shear stress suggests they have the potential to deform under increased stress. The presence of slip ends in the plastic strain distribution, as seen in Grain 1, Grain 3, and Grain 5, is indicative of slip activity and localized plastic deformation. Some grains, like Grain 2, showed heterogeneous shear stress distribution, which suggested strain localization due to neighbouring grain influences or intrinsic grain properties. Meanwhile, Grain 4, despite possessing a moderate Young's modulus and a high  $E \cdot m$  value, showed no signs of plastic strain, indicating its resistance to deformation. Similarly, Grain 6, with its high modulus and RSS, had undergone minimal plastic strain but may still deform under further loading. Grain 7, with a low Young's modulus but high RSS,

also exhibited no plastic strain, reinforcing the idea that it had not yet experienced significant deformation but could if stress levels increase. Grains 2 and 6 likely had the highest Schmid factors, making them more prone to slip. Grains 1, 4, and 5 had moderate Schmid factors, meaning they may experience some slip under applied stress. Grains 3 and 7 have lower Schmid factors, meaning they were less likely to experience plastic deformation. Overall, the analysis highlights the heterogeneous nature of deformation within the material, showing that while some grains readily undergo plastic deformation, others resist due to their inherent properties and interactions with neighbouring grains. The interplay of Young's modulus ( $E$ ), the product of Young's modulus and Schmid factor ( $E \cdot m$ ), Schmid factor ( $m$ ), plastic strain, and shear stress significantly influenced how each grain responds to external loading. This suggests that stress concentration points exist, leading to strain localization in certain regions, which could impact the material's failure mechanisms. Understanding these interactions is crucial for optimizing microstructural properties and improving material performance.

Slip bands were created as a result of acoustic softening. When the material was subjected to sonication, it was observed that dislocations moved along specific crystallographic planes. Grains with different orientations reacted differently to ultrasound and the duration for which it was applied, leading to heterogeneous slip band formation across the material, as seen in Fig. 4-11. It was observed that in Fig. 4-11(b), the occurrence of slip was illustrated using highlighted lines. The highlighted lines likely present slip, which form when the material undergoes plastic deformation. The material's behavior was understood through this phenomenon. The formation of slip bands was observed using SEM. The SEM image attached below illustrated the presence and pattern of slip bands at several locations, allowing for the analysis of strain localization and dislocation activity within the material.

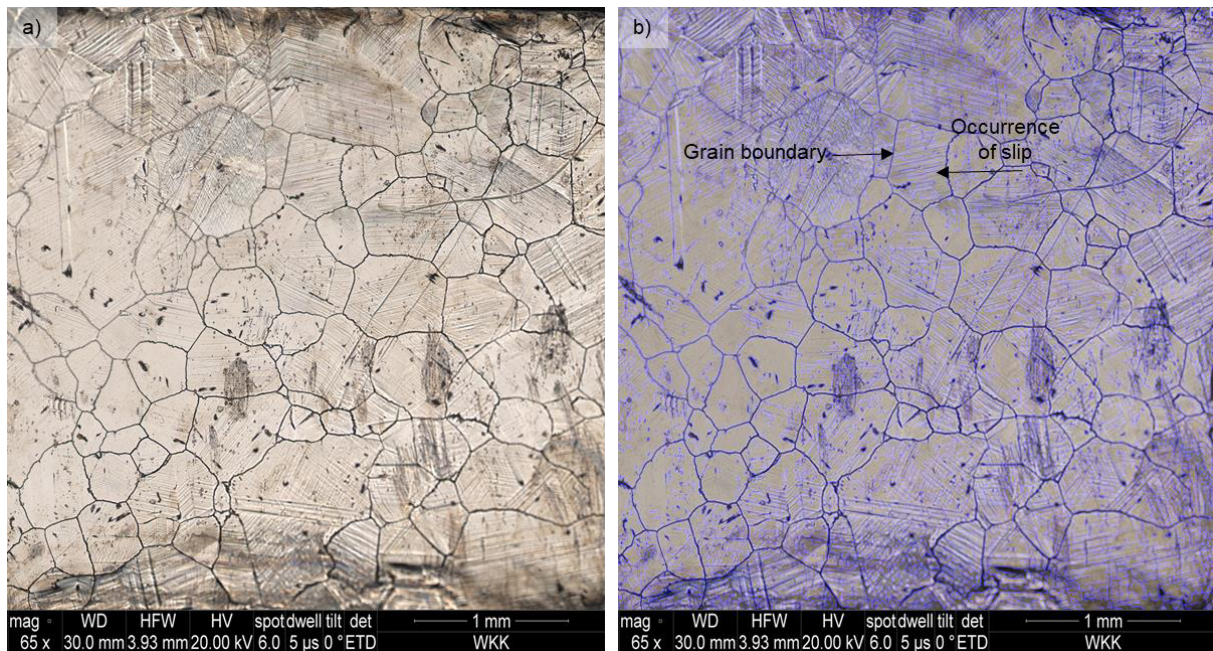


**Fig. 4-11 SEM image of Sample N1 a) With slip bands b) Highlighted slip bands**

The correlation between GND density observations and the mechanical parameters (Young's modulus  $E$ , the product of Young's modulus and Schmid factor  $E \cdot m$ , and the Schmid factor  $m$ ) showed the material's heterogeneous deformation behaviour. Grains with high  $E$  and  $E \cdot m$ , such as Grain 1 and Grain 5, exhibited significant GND density under applied force, indicating strong internal stresses and susceptibility to plastic deformation. However, their relaxation under ultrasound suggested that sonication can effectively redistribute or eliminate dislocations. On the other hand, grains with low  $E$  or high  $m$ , like Grain 2, retained their GND density despite force and ultrasound exposure, implying structural resistance to deformation. Grain 6, showed minimal plastic strain despite high  $E$  and RSS, aligns with its observed GND behaviour, where slip bands emerged under prolonged ultrasound. The smallest grains, such as Grain 7, with lower  $E$  and minimal GND retention, suggest that smaller grains were more adaptable to external influences, with dislocations forming and dissipating readily. Overall, the interplay between GND density,  $E$ ,  $E \cdot m$  and  $m$  reveals that grain-level mechanical properties dictate deformation mechanisms, influencing stress localization, slip activity, and overall material response to external loading.

Sample 2 (N2) of the same alloy, IN617, was subjected to identical test conditions as the previous sample, and the following observations were made regarding the GND density of selected grains. Figure 4-11 presents essential properties such as Young's modulus, the product of Young's modulus and the Schmid factor ( $E \cdot m$ ), the resulting shear stress, and the total strain.

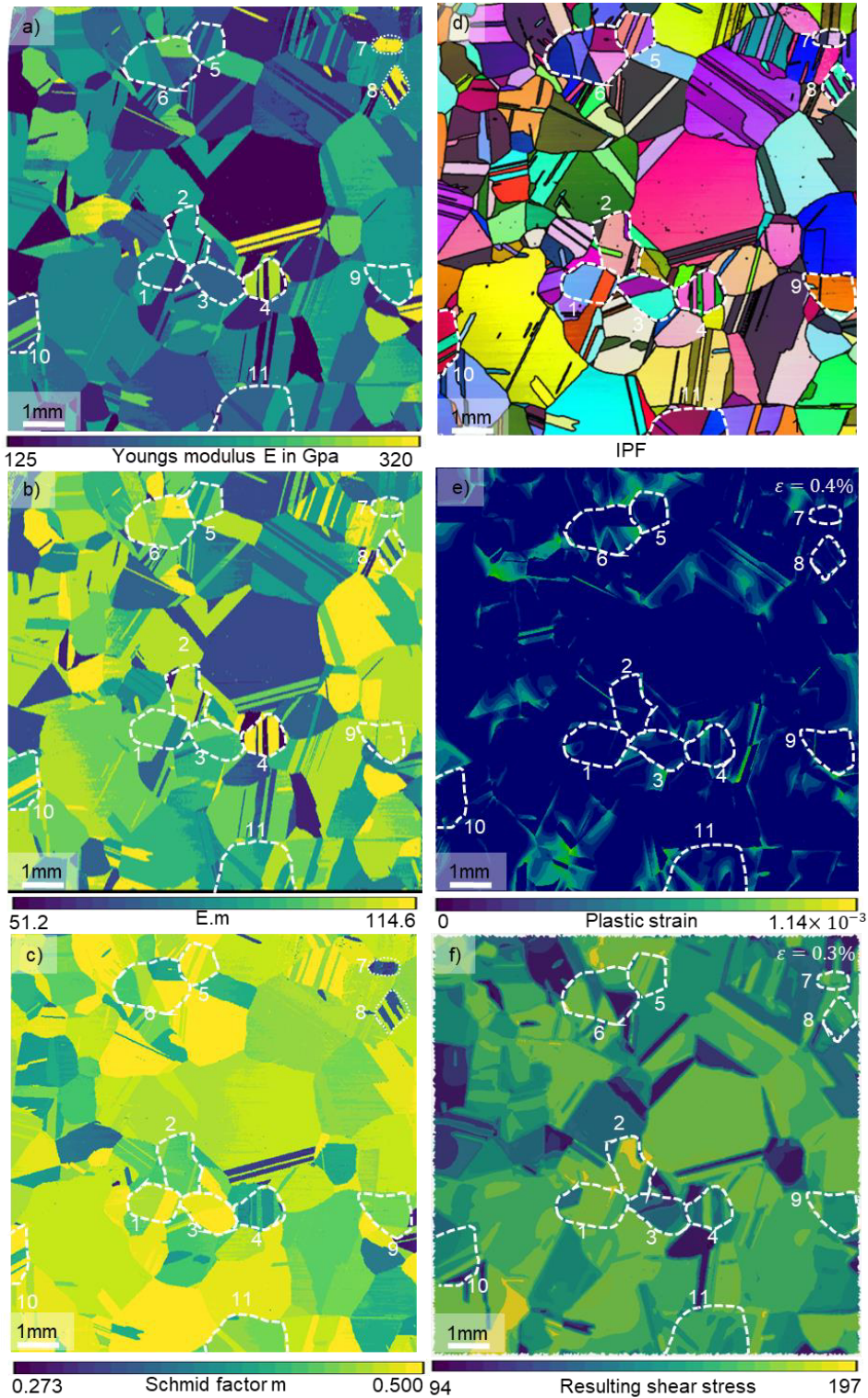
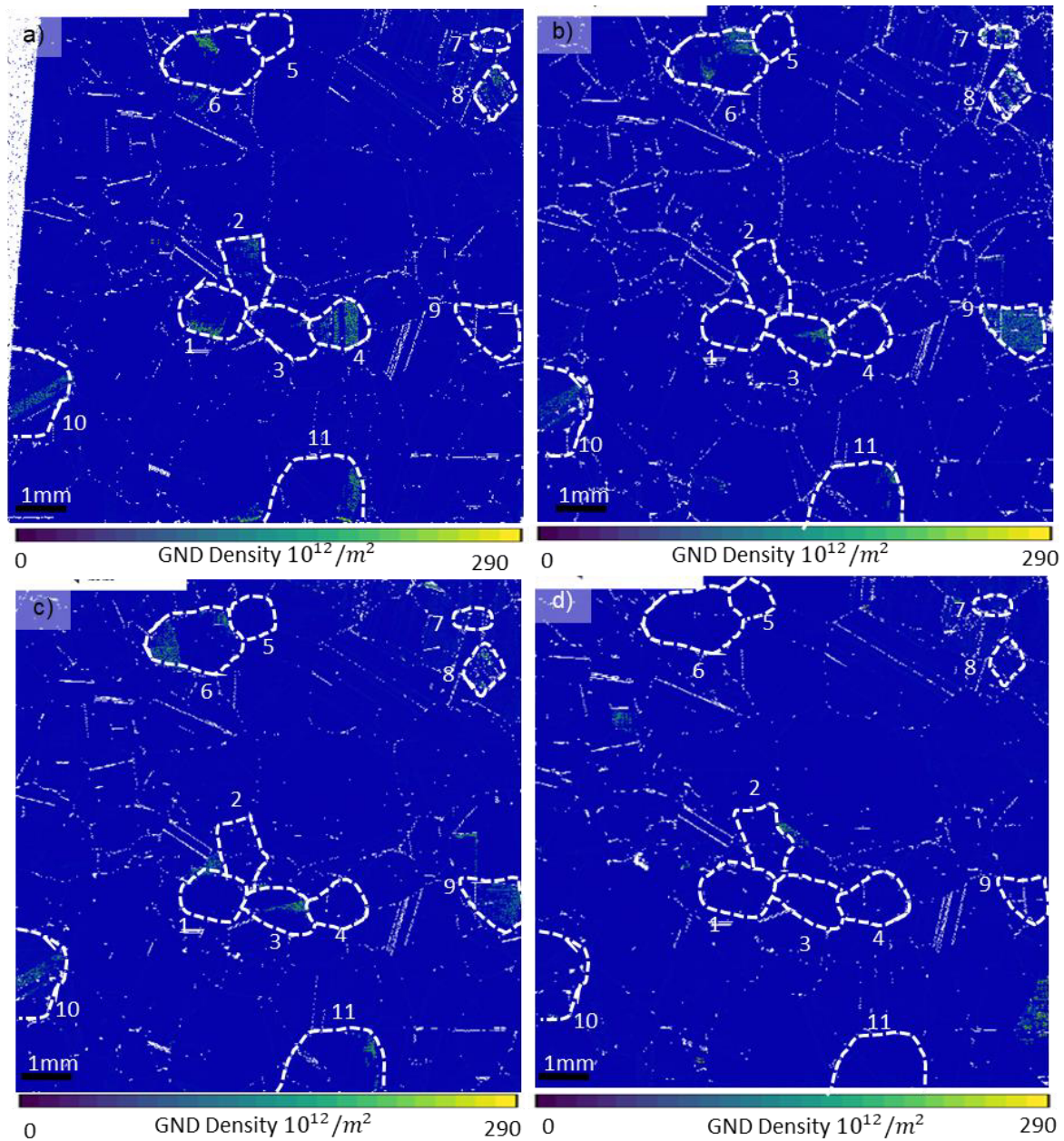


Fig. 4-12 a) Youngs modulus  $E$  in GPa, b) Product of Youngs Modulus and Schmid factor ( $E \cdot m$ ) in GPa  
c) Schmid factor( $m$ ), d) IPF (Inverse Pole figure), e) Plastic strain, f) Resulting shear stress in MPa

The overall GND density map for Sample N2 is provided below.



**Fig. 4-13** GND density maps for all tests conducted on Sample N2: (a) N2\_A (initial), (b) N2\_B (only Force 400N), (c) N2\_C (20 $\mu$ m, ~100-200N, 50ms) and (d) N2\_D (20 $\mu$ m, ~100-200N, 5000ms).

Grain 1 had GND density along the grain boundary Fig.4-14b. Throughout all test conditions—including force application Fig. 4-14c, ultrasound with force for a short duration Fig. 4-17d, and with sonication of 5000ms Fig. 4-14e GND density was not seen, indicating no structural changes or dislocation rearrangements within the grain. With respect to mechanical properties Grain 1 exhibited a moderate Young's modulus (Fig. 4-12a). It had a relatively high  $E \cdot m$  value

(Fig. 4-12b), but plastic strain remained low. This grain had a relatively high Schmid factor, making it more prone to slip under applied stress (Fig. 4-12c). A possibility of slip ends was observed (Fig. 4-12e), along with high shear stress concentration, which could contribute to localized strain accumulation (Fig. 4-12f).

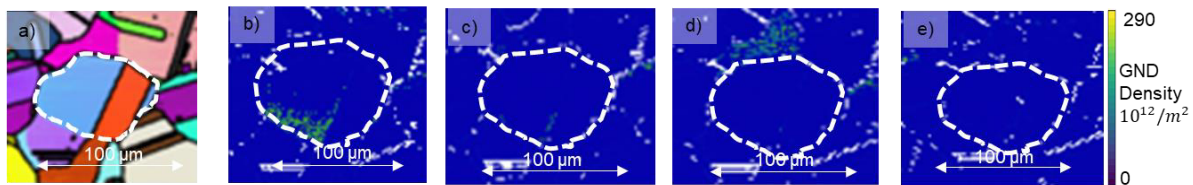


**Fig. 4-14** a) IPF (Inverse pole figure) and evolution of GND Density in Grain 7 b) N2\_A (initial), c) N2\_B (only Force 400N), d) N2\_C (20 $\mu$ m, ~100-200N, 50ms), e) N2\_D (20 $\mu$ m, ~100-200N, 5000ms).

Grain 2 initially had GND density, as shown in Fig. 4-15b. Upon the application of force, GND density was barely observed in Fig. 4-15c. When ultrasound was introduced along with force for a short duration, the GND was not seen, as shown in Fig. 4-15d. With sonication of about 5000ms, the GND density was not seen, as depicted in Fig. 4-15e. In terms of mechanical properties, Grain 2 had a moderate Young's modulus (Fig. 4-12a) and a high  $E \cdot m$  value (Fig. 4-12b). It had moderate Schmid factor (Fig. 4-12c). The presence of twins suggests slip activity or the potential for plastic deformation (Fig. 4-12e). Given the high  $E \cdot m$  and RSS (Fig. 4-12f), plastic deformation likely occurred, indicating the material's response to stress in this region.

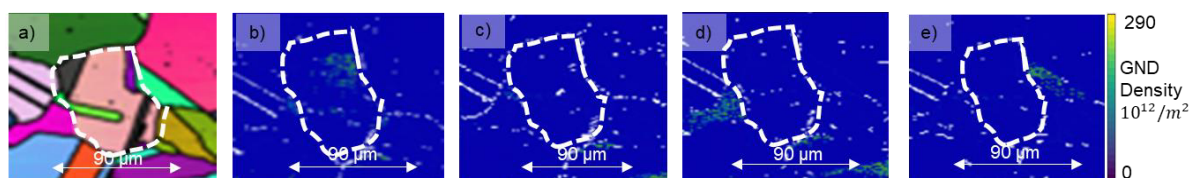


**Fig. 4-15** a) IPF (Inverse pole figure) and evolution of GND Density in Grain 7 b) N2\_A (initial), c) N2\_B (only Force 400N), d) N2\_C (20 $\mu$ m, ~100-200N, 50ms), e) N2\_D (20 $\mu$ m, ~100-200N, 5000ms).

Grain 3 has very minimal GND density Fig. 4-16b. When force was applied, GND density can be observed as seen in Fig. 4-16c. This trend continues with ultrasound applied for a short duration Fig. 4-16d. However, with sonication for 5000ms, the GND density was not seen Fig. 4-16e, indicating ultrasound's role in structural stabilization and stress relief. Regarding mechanical properties Grain 3 demonstrated moderate Young's modulus and  $E \cdot m$  values (Figs. 4-12a, 4-12b). Varying plastic strain across the grain suggested potential deformation

(Fig. 4-12e), though the resulting shear stress is relatively low (Fig. 4-12f), which may indicate limited slip propagation.

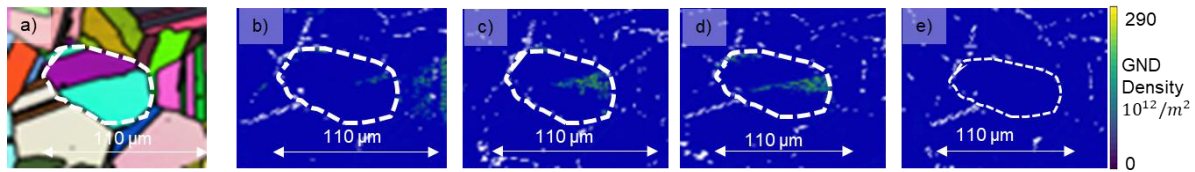


**Fig. 4-16** a) IPF (Inverse pole figure) and evolution of GND Density in Grain 7 b) N2\_A (initial), c) N2\_B (only Force 400N), d) N2\_C (20 $\mu$ m, ~100-200N, 50ms), e) N2\_D (20 $\mu$ m, ~100-200N, 5000ms).

Grain 4 considered here was a substructure and was a combination of many smaller grains. Initially, it had GND density Fig. 4-17b and was not seen with force application Fig. 4-17c. The application of ultrasound with force for a short duration had no GND density Fig. 4-17d, and with sonication for 5000ms no GND density was seen Fig. 4-17e. Considering the mechanical properties Grain 4 had twins, suggesting deformation mechanisms like dislocation movement or strain localization (Fig. 4-12a). Twin boundaries in  $E \cdot m$  indicate strain variations (Fig. 4-12b). It had a relatively high Schmid factor with some variation, experiencing localized slip under applied stress (Fig. 4-12c). Variation in plastic strain indicates localized strain accumulation (Fig. 4-12e), while heterogeneous stress distribution was evident, potentially influencing adjacent grains (Fig. 4-12f).

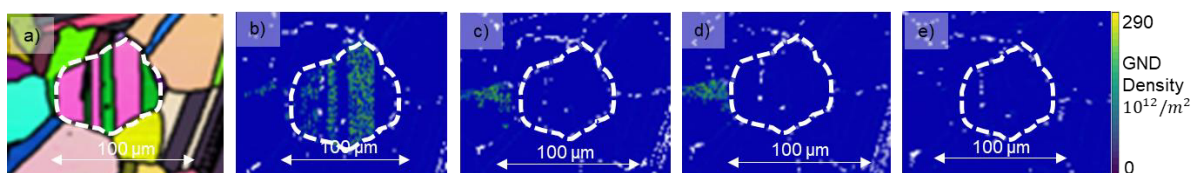


**Fig. 4-17** a) IPF (Inverse pole figure) and evolution of GND Density in Grain 7 b) N2\_A (initial), c) N2\_B (only Force 400N), d) N2\_C (20 $\mu$ m, ~100-200N, 50ms), e) N2\_D (20 $\mu$ m, ~100-200N, 5000ms).

The substructure considered here was composed of multiple grains, which exhibited unique structural and mechanical properties. Plastic strain and resulting shear stress were presented in Figure 4-18 to provide a better understanding of the grain. The alignment of high-strain and high-shear-stress bands suggested that slip or dislocation activity was highly likely to occur. The heterogeneous distribution indicated a grain-specific response, while the presence of high strain suggested that dislocation activity had taken place. Additionally, the non-uniform stress

distribution indicated that interactions with neighbouring grains and grain boundaries had influenced how stress was propagated.

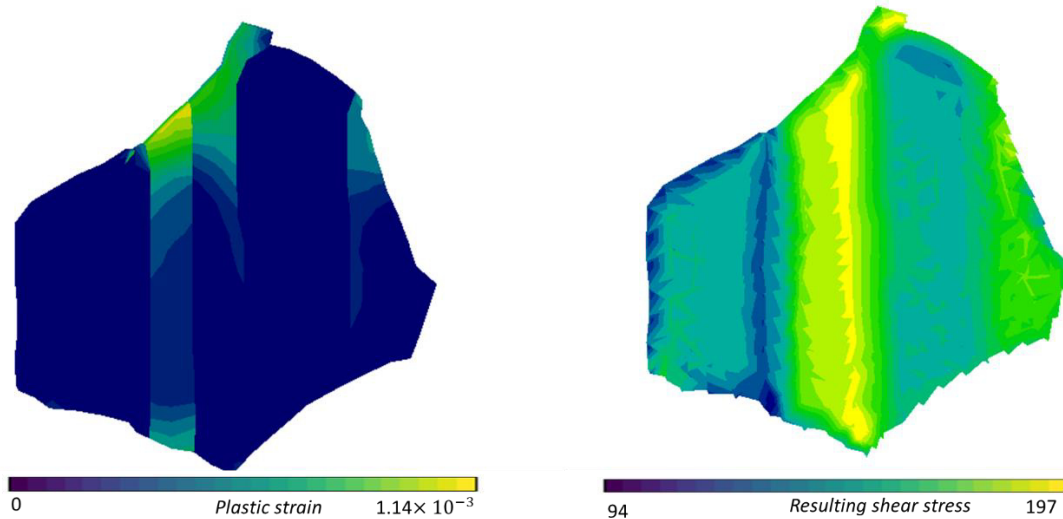


**Fig. 4-18 Plastic Strain and Resulting Shear Stress Distribution in an IN617 Alloy Grain 4**

Grain 5 had no GND density in all test cases. Despite force application Fig. 4-19c and sonication Fig. 4-19d, Fig. 4-19e, no significant changes occurred, this might indicate that this grain had resistance to structural modifications and might have inherent stability under the given conditions. In relation to mechanical properties Grain 5 displayed alternating Young's modulus values, implying dislocation activity or slip (Fig. 4-12a). Moderate  $E \cdot m$  values were observed (Fig. 4-12b). With a moderate Schmid factor, this grain may exhibit some slip activity (Fig. 4-12c). The presence of twins suggested slip (Fig. 4-12e), while high  $E \cdot m$  and RSS confirm plastic deformation, reinforcing the significance of stress interactions within the microstructure (Fig. 4-12f).

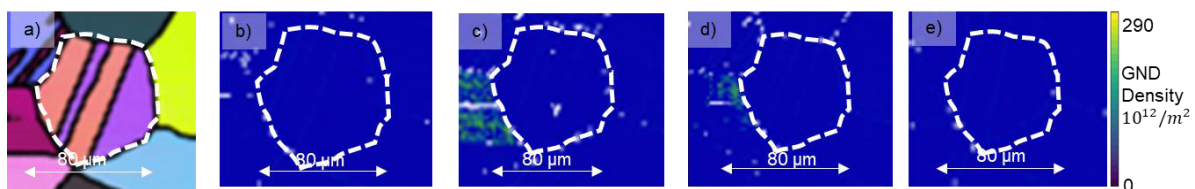


**Fig. 4-19 a) IPF (Inverse pole figure) and evolution of GND Density in Grain 7 b) N2\_A (initial), c) N2\_B (only Force 400N), d) N2\_C (20 $\mu$ m, ~100-200N, 50ms), e) N2\_D (20 $\mu$ m, ~100-200N, 5000ms).**

Grain 6 studied here is a substructure similar to grain 4 that exhibited a dynamic shift in GND density. Initially GND density was seen in Fig. 4-20b, and relocates within the grain upon force application Fig. 4-20c, suggesting internal stress redistribution. With ultrasound applied for a short duration, the GND density was seen again Fig. 4-20d, possibly due to the vibrational energy influencing dislocation mobility. However, sonication for 5000ms eliminated the GND density completely Fig. 4-20e. From a mechanical properties perspective Grain 6 had varying Young's modulus zones (Fig. 4-12a) and diverse  $E \cdot m$  values (Fig. 4-12b). A slightly higher Schmid factor than some neighbouring grains suggested moderate slip initiation (Fig. 4-12c). Plastic strain variations indicated slip or deformation (Fig. 4-12e), with shear stress influenced by neighbouring grains (Fig. 4-12f). This variation may lead to localized mechanical instability within the material.

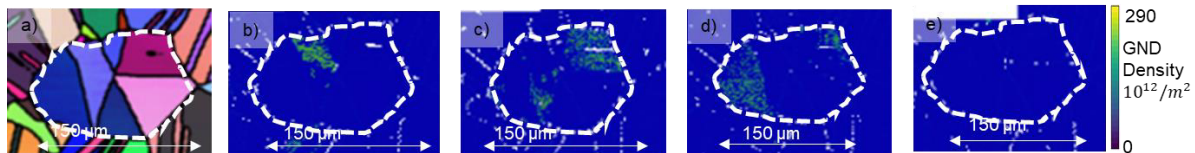


**Fig. 4-20** a) IPF (Inverse pole figure) and evolution of GND Density in Grain 7 b) N2\_A (initial), c) N2\_B (only Force 400N), d) N2\_C (20 $\mu$ m, ~100-200N, 50ms), e) N2\_D (20 $\mu$ m, ~100-200N, 5000ms).

This substructure shown below is also a combination of many small grains, similar to grain 4 discussed in Fig. 4-18. It also followed the material and mechanical properties discussed above.

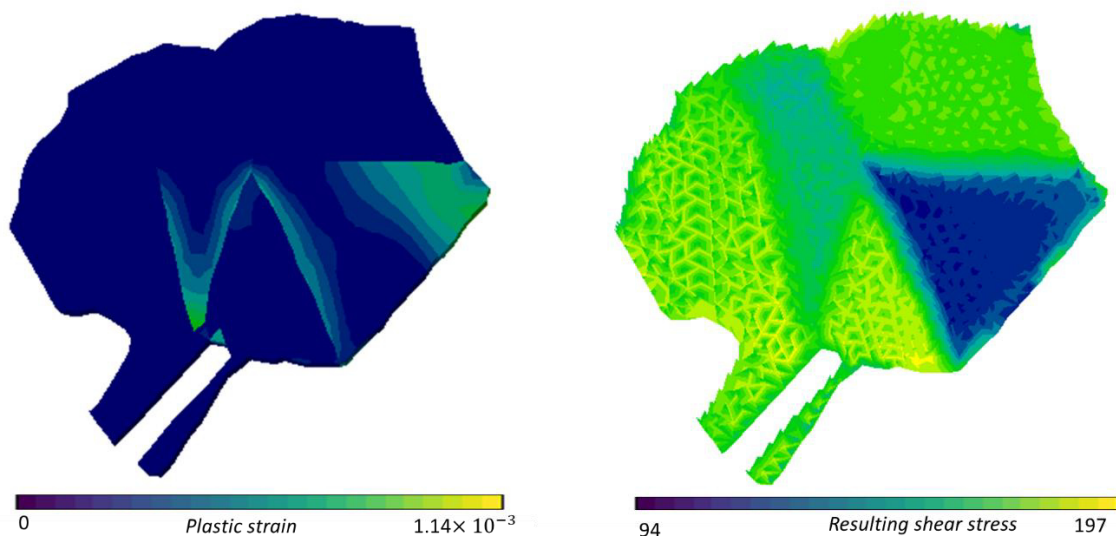


**Fig. 4-21** Plastic Strain and Resulting Shear Stress Distribution in an IN617 Alloy Grain 6

Grain 7, though small, displays unique behaviour. It had noticeable GND density Fig. 4-22b, which remained the same with force application Fig. 4-22c. With the introduction of ultrasound GND density was barely seen Fig. 4-22d, facilitating dislocation rearrangement, and with sonication for 5000ms no GND density was seen Fig. 4-22e, indicating an efficient relaxation process. Grain 7 had a very high Young's modulus (Fig. 4-12a) and a relatively high  $E \cdot m$  value (Fig. 4-12b). The value of Schmid factor was low (Fig. 4-12c). Despite minimal plastic strain (Fig. 4-12e), high  $E \cdot m$  and RSS suggest some plastic deformation (Fig. 4-12f). This indicated a contradiction where the grain appears both stiff and susceptible to stress concentration.

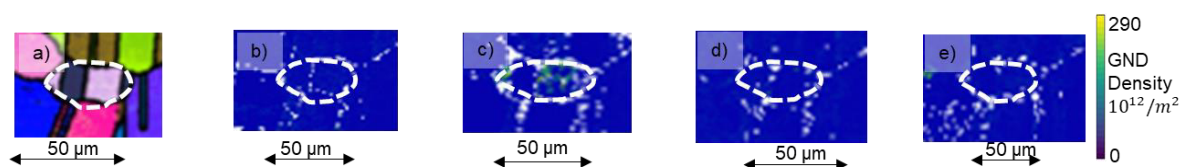


**Fig. 4-22** a) IPF (Inverse pole figure) and evolution of GND Density in Grain 7 b) N2\_A (initial), c) N2\_B (only Force 400N), d) N2\_C (20 $\mu$ m, ~100-200N, 50ms), e) N2\_D (20 $\mu$ m, ~100-200N, 5000ms).

Grain 8 initially had GND density (Fig. 4-23b). Upon the application of force, the GND density remained the same (Fig. 4-23c). When ultrasound was applied along with force for a short duration, the GND density was barely seen (Fig. 4-23d). With sonication of 5000ms, the GND density was completely eliminated (Fig. 4-23e), demonstrating the progressive effect of ultrasound in aiding material stabilization. In terms of mechanical properties, Grain 8 displayed alternating Young's modulus values, suggesting dislocation activity or slip (Fig. 4-12a). The  $E \cdot m$  value varied significantly (Fig. 4-12b). Similar to the previous grain, this grain also had a low Schmid factor (Fig. 4-12c). The presence of twins in the plastic strain distribution indicated slip or plastic deformation (Fig. 4-12e), while the shear stress remained high and homogeneous (Fig. 4-12f), highlighting the uniform distribution of stress across the grain.

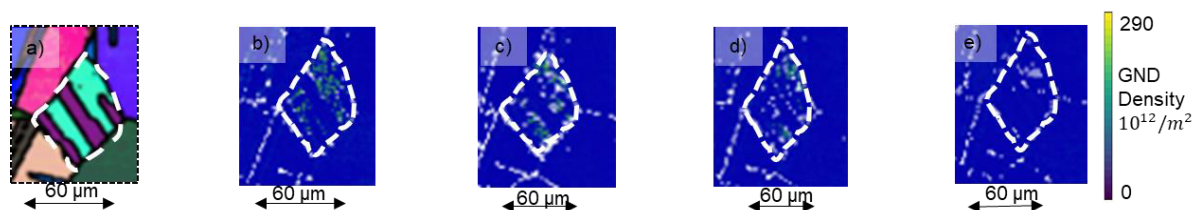


**Fig. 4-23** a) IPF (Inverse pole figure) and evolution of GND Density in Grain 7 b) N2\_A (initial), c) N2\_B (only Force 400N), d) N2\_C (20 $\mu$ m, ~100-200N, 50ms), e) N2\_D (20 $\mu$ m, ~100-200N, 5000ms).

With Grain 9 no GND density was seen (Fig. 4-24b). However, upon the application of force, the GND was greatly seen along the grain (Fig. 4-24c), likely due to mechanical strain-induced dislocation generation. When ultrasound was applied along with force for a short duration, GND density was still seen along the grain boundary, as seen in (Fig. 4-24d), indicating the initial effect of vibrational energy. With sonication of 5000ms GND density was not observed with the grain (Fig. 4-24e). Considering the grain's mechanical properties, Grain 9 exhibited a very high Young's modulus (Fig. 4-12a), a high  $E \cdot m$  value (Fig. 4-12b) a low Schmid factor (Fig. 4-12c). Despite the absence of plastic strain (Fig. 4-12e), the presence of uniformly distributed high shear stress suggested potential plastic deformation (Fig. 4-12f), reinforcing the concept of stress accommodation without significant strain localization.

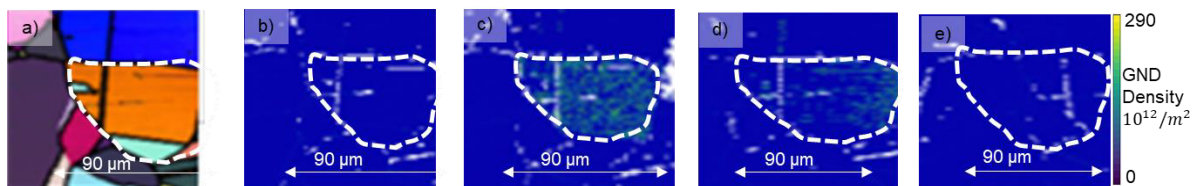


**Fig. 4-24** a) IPF (Inverse pole figure) and evolution of GND Density in Grain 7 b) N2\_A (initial), c) N2\_B (only Force 400N), d) N2\_C (20 $\mu$ m, ~100-200N, 50ms), e) N2\_D (20 $\mu$ m, ~100-200N, 5000ms).

Grain 10 initially had GND density (Fig. 4-25b), which remained unchanged with force application (Fig. 4-25c) and ultrasound exposure for a short duration (Fig. 4-25d). However, with prolonged sonication, GND density was not seen (Fig. 4-25e), indicating that extended ultrasound significantly influences this grain, possibly through energy-assisted structural rearrangement. Grain 10 exhibited alternating Young's modulus values, suggesting dislocation activity or slip (Fig. 4-12a).  $E \cdot m$  also fluctuated (Fig. 4-12b). The grain had low Schmid factor (Fig. 4-12c). The presence of twins in plastic strain indicated slip or plastic deformation (Fig. 4-12e), while high and uniform shear stress supports this possibility (Fig. 4-12f), further demonstrating the interaction of mechanical properties within the microstructure.

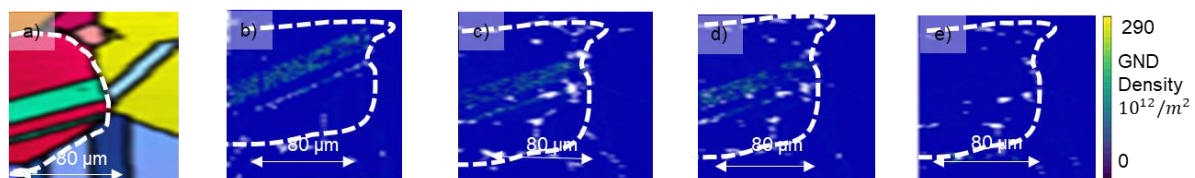


**Fig. 4-25** a) IPF (Inverse pole figure) and evolution of GND Density in Grain 7 b) N2\_A (initial), c) N2\_B (only Force 400N), d) N2\_C (20 $\mu$ m, ~100-200N, 50ms), e) N2\_D (20 $\mu$ m, ~100-200N, 5000ms).

Grain 11 had GND density (Fig. 4-26b), which remained low upon force application (Fig. 4-26c), indicating some dislocation movement. When ultrasound was applied for a short duration, the GND density was barely seen and shifts toward the grain border (Fig. 4-26d), suggesting localized redistribution. With prolonged exposure, the GND density was not seen (Fig. 4-26e). In terms of mechanical properties, Grain 11 displayed alternating Young's modulus values, indicating dislocation or slip activity (Fig. 4-12a). The  $E \cdot m$  value was relatively high and influenced by neighbouring grains (Fig. 4-12b). The grain had the lowest Schmid factor compared to the other grains (Fig. 4-12c). The observation of plastic strain suggests slip or plastic deformation (Fig. 4-12e), while variations in shear stress indicate deformation potential (Fig. 4-12f). This highlights the influence of surrounding grains on localized mechanical responses.

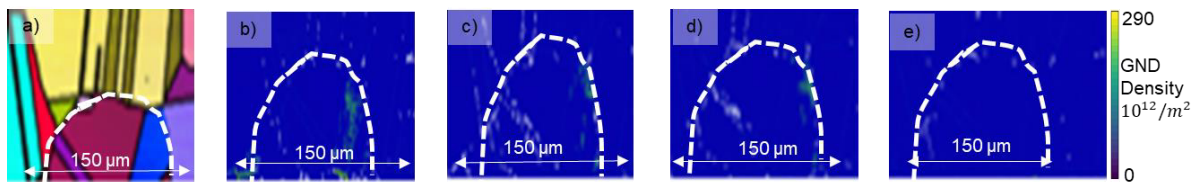


**Fig. 4-26** a) IPF (Inverse pole figure) and evolution of GND Density in Grain 7 b) N2\_A (initial), c) N2\_B (only Force 400N), d) N2\_C (20 $\mu$ m, ~100-200N, 50ms), e) N2\_D (20 $\mu$ m, ~100-200N, 5000ms).

The schematic diagram below illustrates the changes each grain undergoes during different testing phases.

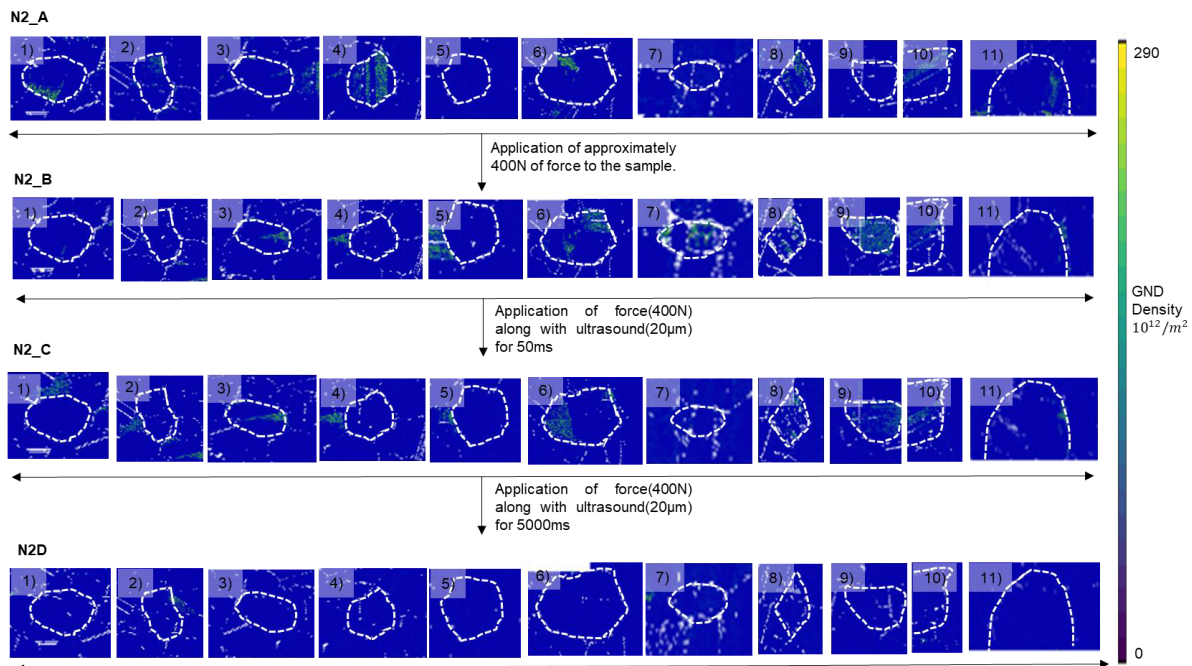


**Fig. 4-27** Evolution of GND Density in IN617 Alloy Grains Under Mechanical and Ultrasonic Conditions for sample N2

This analysis provides insights into how different grains in Sample 2 of IN617 respond to applied force and ultrasound, revealing key aspects of material deformation behaviour and dislocation movement.

A notable trend was observed in grains such as Grain 2, Grain 4, and Grain 8, where initially GND density was prominently seen and gradually becomes low and is completely eliminated with prolonged sonication. This indicated that ultrasound effectively aids in dislocation removal. These grains demonstrated the effectiveness of ultrasound in facilitating stress relief. On the other hand, Grain 1 and Grain 5 exhibited inherent stability, with no significant changes in GND density across all test conditions. The resistance to both force-induced and ultrasound-driven modifications suggested that certain grains possessed structural robustness, possibly due to their orientation, composition, or interaction with surrounding grains. Interestingly, Grain 6 and Grain 11 displayed dynamic behaviour where GND density was not only seen but also appears within the grain. The application of force initially redistributes dislocations, while ultrasound further influences their mobility, eventually leading to complete elimination. This suggests that vibrational energy promoted directional dislocation movement before facilitating full relaxation. In contrast, Grain 3 and Grain 9 initially exhibited GND density upon force application, highlighting that mechanical stress can introduce new dislocations. However, sonication for 5000ms counteracts this effect, demonstrating its role in stress dissipation and dislocation removal. The behaviour of Grain 7, a relatively small grain, aligned with its size-dependent response, where GND density fluctuates but ultimately is not seen with ultrasound. This suggests that smaller grains might be more adaptable to external influences, with dislocations forming and disappearing more readily. Grain 10 presents an interesting case where the GND density remained unchanged despite force and short-duration ultrasound exposure. However, prolonged sonication treatment eventually leads to dislocation elimination, indicating that certain grains may require extended exposure for effective structural modification. Overall, these findings highlight the significant role of ultrasound in manipulating dislocation structures, promoting stress relief, and influencing material stability.

This grain analysis provides valuable insights into the mechanical behaviour of the material under applied stress. The interplay between Young's modulus, the product of Young's modulus and Schmid factor ( $E \cdot m$ ), plastic strain, and shear stress significantly influences how each grain responds to external loading. Grains with a high Young's modulus, such as Grain 1, Grain 5, and Grain 6, exhibited relatively high  $E \cdot m$  values, indicating strong susceptibility to plastic deformation under sufficient loading. However, Grain 1 showed low plastic strain despite its

high shear stress concentration, which suggests localized strain accumulation rather than widespread deformation. Similarly, Grain 6 exhibited varying mechanical properties influenced by neighbouring grains, leading to zones of different plastic responses. Some grains, like Grain 2 and Grain 8, showed evidence of slip activity or plastic deformation due to high  $E \cdot m$  values and varying plastic strain. These grains also exhibit heterogeneous shear stress distribution, indicating strain localization that may be influenced by neighbouring grains or intrinsic properties. Grain 5, with alternating Young's modulus values, also suggested active slip mechanisms and significant deformation under applied stress. In contrast, Grain 7 and Grain 9, both with very high Young's modulus, displayed minimal plastic strain despite high shear stress. This contradiction suggests that while these grains are resistant to deformation, they may still accommodate stress through other mechanisms such as stress redistribution or neighbouring grain interactions. Grain 4, with varying  $E \cdot m$ , showed signs of strain localization or slip activity, reinforcing the concept of heterogeneous deformation within the material. Grains like Grain 10 and Grain 11 exhibited alternating Young's modulus values, suggesting dislocation movement or slip activity. The twins found in plastic strain and high shear stress indicated potential plastic deformation, further emphasizing how mechanical interactions between grains contributed to localized strain responses. Grains 1 and 2 show relatively high Schmid factors. These grains are likely to experience the most plastic deformation when stress is applied as seen in FE model. Grains 5 and 6 have intermediate Schmid factors, suggesting they may undergo some slip but to a lesser extent than grains with the highest factors. Localized deformation could be present. Grains 3, 4, 7, 8, 9, 10, and 11 exhibit low Schmid factors, meaning they are more resistant to slip. These grains contributed to structural stability and experience less plastic deformation under applied stress. Overall, this analysis highlighted the heterogeneous nature of deformation within the material. Some grains readily undergo plastic deformation, while others resist due to their inherent properties and interactions with neighbouring grains. The existence of stress concentration points suggested strain localization in specific regions, which could influence the material's failure mechanisms.

The formation of slip bands can be observed with the help of SEM. The SEM image attached below illustrates the presence and pattern of slip bands at several spots, allowing for analysis of strain localization and dislocation activity within the material.

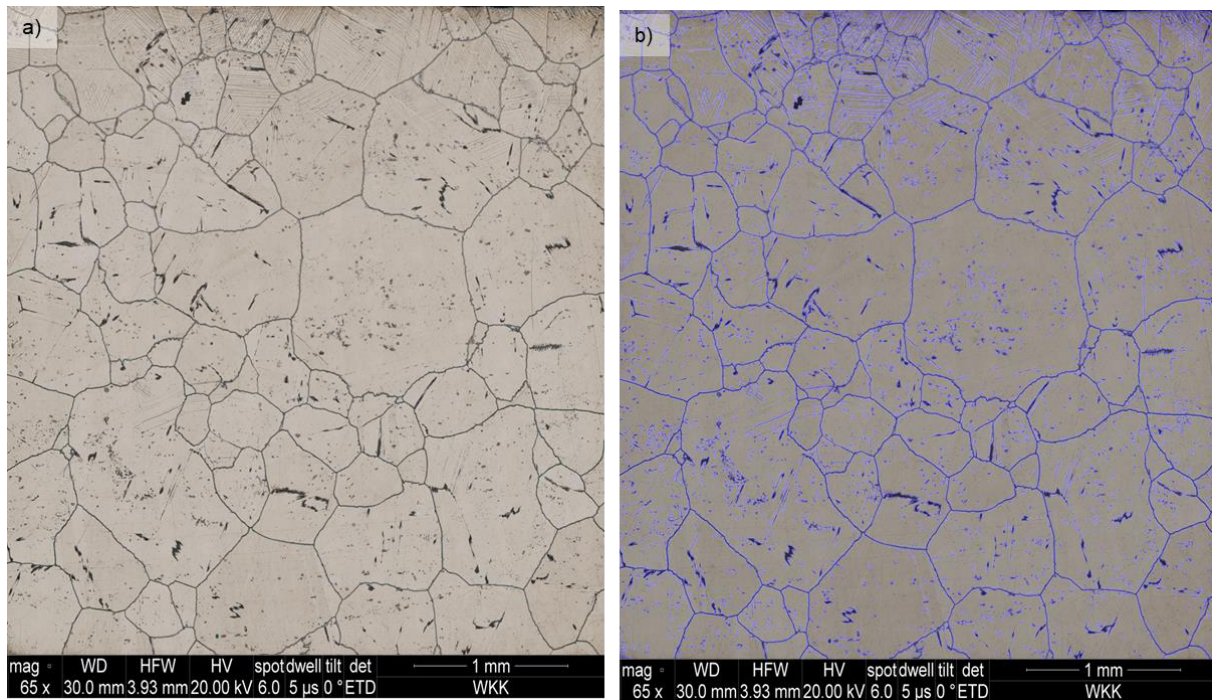


**Fig. 4-28 SEM image of Sample N2 a) With slip bands b) Highlighted slip bands**

The correlation between GND density observations and mechanical parameters ( $E$ ,  $E \cdot m$  and  $m$ ) revealed the complex interplay between microstructural stability and deformation behaviour as seen with sample N1. Grains such as Grain 2, Grain 4, and Grain 8, initially exhibited high GND density but showed gradual dislocation removal with ultrasound, also had high  $E \cdot m$  values indicating significant internal stresses and susceptibility to plastic deformation. Their ability to undergo slip activity aligns with their observed heterogeneous shear stress distribution. In contrast, Grain 1 and Grain 5, which had stable GND density across all conditions, exhibited high  $E$  but low plastic strain, suggesting localized strain accumulation rather than widespread deformation. Grain 6 and Grain 11, which displayed dynamic GND redistribution before dislocation elimination, had moderate  $E \cdot m$  values, implying an intermediate response to stress and ultrasound-induced relaxation. Meanwhile, smaller grains like Grain 7, with fluctuating GND density and high  $E$ , demonstrated adaptability to external influences, reinforcing the idea that grain size impacts dislocation mobility. Additionally, grains with high  $m$ , such as Grain 1 and Grain 2, were more prone to slip and deformation, aligning with their GND accumulation under force. Conversely, grains with low  $m$ , like Grain 3 and Grain 9, resisted slip and maintained structural stability, as seen in their minimal GND density changes. Overall, the correlation suggests that  $E$ ,  $E \cdot m$  and  $m$  collectively influence how dislocations form, move, and relax under mechanical and vibrational energy, shaping the material's deformation mechanisms and stress distribution.

Sample 3(N3) of the IN617 alloy was subjected to identical test conditions as the previous sample, with observations made regarding the GND density of selected grains under different conditions.

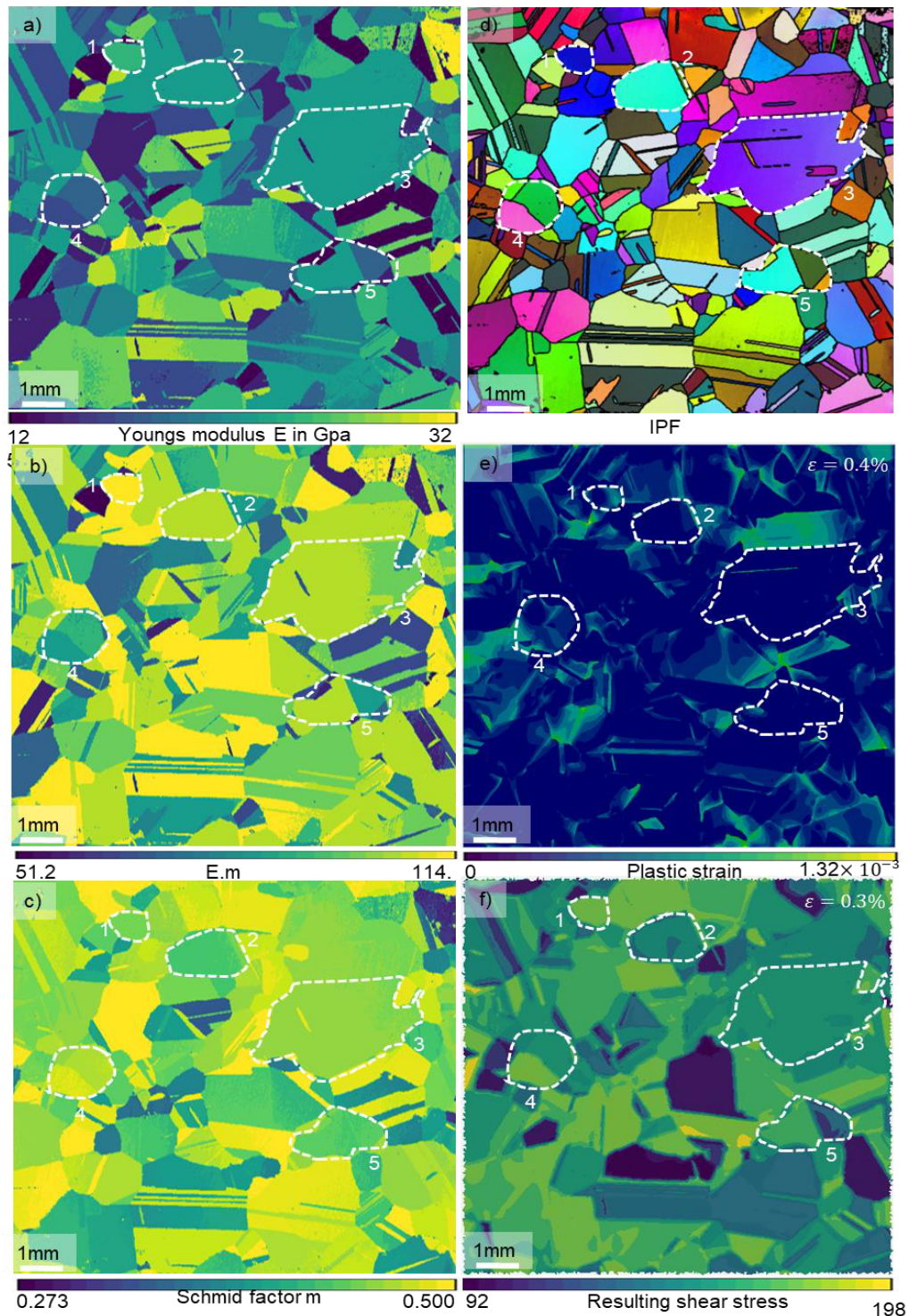


**Fig. 4-29** a) Young's modulus E in GPa, b) Product of Young's Modulus and Schmid factor (E.m) in GPa, c) Schmid factor (m), d) IPF (Inverse Pole figure), e) Plastic strain, f) Resulting shear stress in MPa.

The overall GND density map for Sample N3 is provided below.

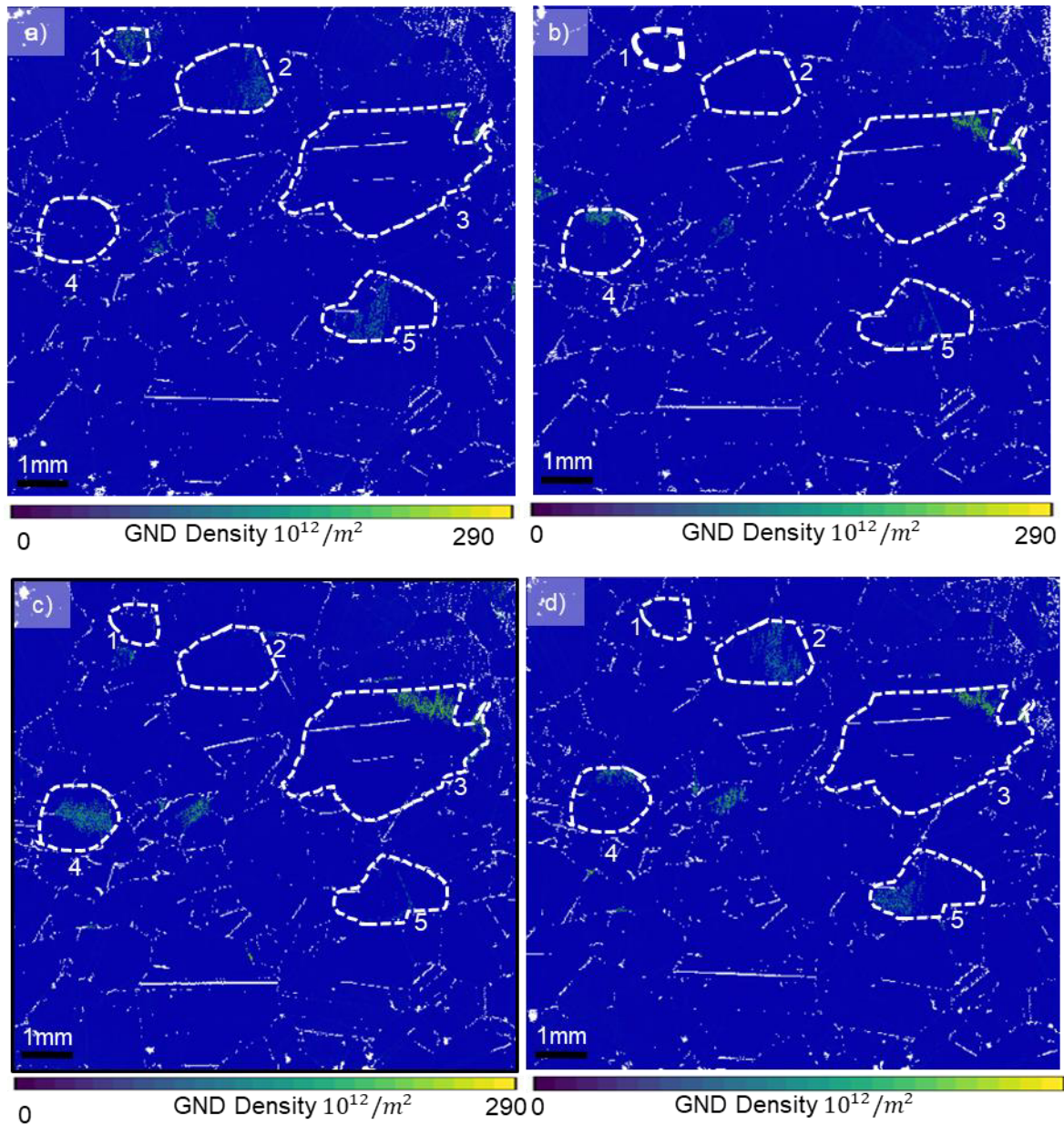


**Fig. 4-30** GND density maps for all tests conducted on Sample N3: (a) N3\_A (initial), (b) N3\_B (only Force 400N), (c) N3\_C (20 $\mu\text{m}$ , ~100-200N, 50ms) and (d) N3\_D (20 $\mu\text{m}$ , ~100-200N, 5000ms).

Grain 1 initially exhibited a noticeable GND density, as observed in Fig. 4-31b. However, upon applying force alone, GND density was not seen, indicating a complete annihilation of dislocations (Fig. 4-31c). When ultrasound was introduced alongside force, both for a short and prolonged duration, the GND was not seen (Figs. 4-31d, 4-31e). This suggests that the combined effect of force and ultrasound promoted dislocation movement to an extent where they either cancel out or redistribute in a way that prevented their reappearance, leading to

sustained dislocation annihilation. Grain 1 exhibited a moderate Young's modulus (Fig. 4-29a) with a relatively high  $E \cdot m$  value (Fig. 4-29b), influenced by neighbouring grains. A low Schmid factor was observed (Fig. 4-29c) The plastic strain distribution varied indicating possible slip and plastic deformation (Fig. 4-29e). Additionally, high shear stress concentration was observed (Fig. 4-29f).

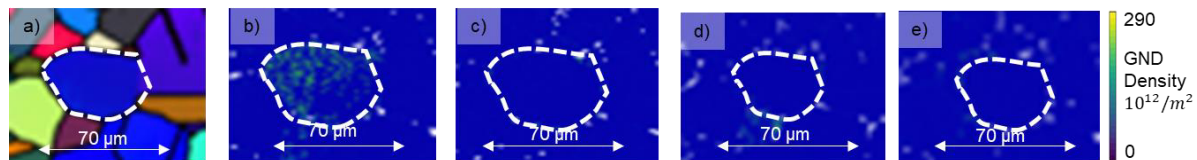


**Fig. 4-31** a) IPF (Inverse pole figure) and evolution of GND Density in Grain 7 b) N3\_A (initial), c) N3\_B (only Force 400N), d) N3\_C (20 $\mu$ m, ~100-200N, 50ms), e) N3\_D (20 $\mu$ m, ~100-200N, 5000ms).

Grain 2 has GND density initially, as seen in (Fig. 4-32b). When force was applied, the GND density was not seen (Fig. 4-32c), indicating that the dislocations were either eliminated or reorganized effectively. When ultrasound was introduced alongside force for a short duration, GND density was still not seen (Fig. 4-32d), implying that no new dislocations are generated in the grain. However, in contrast to this, sonication for 5000ms along with force resulted in a resurgence of GND density (Fig. 4-32e). This phenomenon suggests that instead of further annihilation, the prolonged vibrational energy induced a reorganization of dislocations, potentially due to stress redistribution within the grain structure. Grain 2 also had a moderate Young's modulus (Fig. 4-29a), a high  $E \cdot m$  value (Fig. 4-29b) and high Schmid factor (Fig. 4-29c). However, it shows zero plastic strain (Fig. 4-29e), while the shear stress remained high and uniformly distributed, suggesting the potential for plastic deformation (Fig. 4-29f).

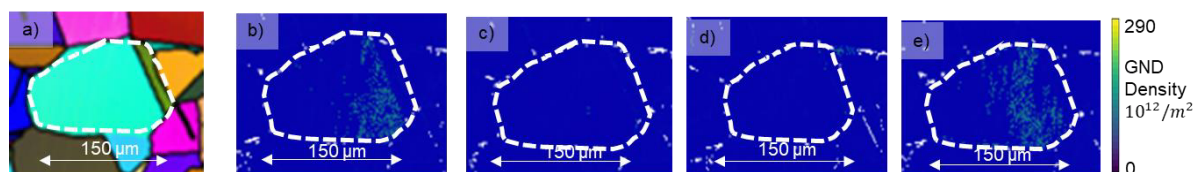


**Fig. 4-32** a) IPF (Inverse pole figure) and evolution of GND Density in Grain 7 b) N3\_A (initial), c) N3\_B (only Force 400N), d) N3\_C (20 $\mu$ m, ~100-200N, 50ms), e) N3\_D (20 $\mu$ m, ~100-200N, 5000ms).

Grain 3 initially possessed GND density, as depicted in (Fig. 4-33b). When force alone was applied, GND density was greatly seen as observed (Fig. 4-33c), suggesting an accumulation of dislocations due to external stress. With the addition of ultrasound for a short duration, this

GND density was maintained (Fig. 4-33d). This indicated that while ultrasound does not immediately reduce dislocation density, it may influence their mobility, leading to minor reconfigurations. However, when ultrasound was applied for 5000ms, the GND density was slightly seen experiencing a slight reduction (Fig. 4-33e), signifying a gradual relaxation of dislocations over time. This suggests that extended vibrational exposure facilitated partial dislocation annihilation, but not to the extent observed in other grains. Grain 3 displayed a range of Young's modulus values, including a localized region with very low modulus, indicating a potential deformation zone (Fig. 4-29a).  $E \cdot m$  values alternate across different sections (Fig. 4-29b), but plastic strain remains zero (Fig. 4-29c) and the Schmid factor was similar to grain 1 and was low (Fig. 4-29e) The resulting shear stress was high and homogenous (Fig. 4-29f).

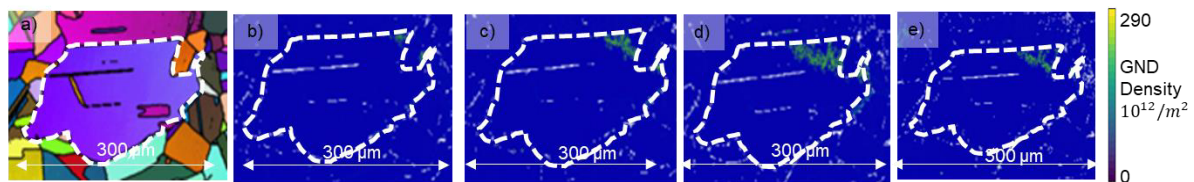


**Fig. 4-33** a) IPF (Inverse pole figure) and evolution of GND Density in Grain 7 b) N3\_A (initial), c) N3\_B (only Force 400N), d) N3\_C (20 $\mu$ m, ~100-200N, 50ms), e) N3\_D (20 $\mu$ m, ~100-200N, 5000ms).

Grain 4 initially exhibited no GND density, as seen in (Fig. 4-34b). Upon applying force, GND density was observed, particularly along the grain boundary (Fig. 4-34c), indicating that stress leads to localized dislocation accumulation at these regions. When ultrasound was applied for a short duration along with force, the density concentration shifts towards the grain centre (Fig. 4-34d). However, with sonication for 5000ms, the GND density was greatly seen along the grain boundary (Fig. 4-34e), demonstrating a dynamic and cyclic movement of dislocations within the grain. Grain 4 exhibited alternating Young's modulus values, indicating possible dislocation activity or slip (Fig. 4-29a). The  $E \cdot m$  values were also distributed in alternating patterns (Fig. 4-29b). This grain had a relatively high Schmid factor with some variation, experiencing localized slip under applied stress (Fig. 4-29c). A striped plastic strain pattern suggested ongoing slip or potential plastic deformation (Fig. 4-29e), while the shear stress distribution appeared heterogeneous due to varying stress levels and neighbouring grain influences (Fig. 4-29f).

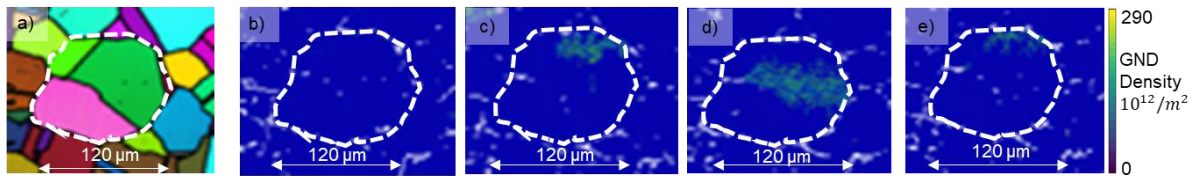


**Fig. 4-34** a) IPF (Inverse pole figure) and evolution of GND Density in Grain 7 b) N3\_A (initial), c) N3\_B (only Force 400N), d) N3\_C (20 $\mu\text{m}$ , ~100-200N, 50ms), e) N3\_D (20 $\mu\text{m}$ , ~100-200N, 5000ms).

GND density was seen initially in Grain 5, as illustrated in (Fig. 4-35b). With the application of force alone GND density was still seen (Fig. 4-35c). The presence of GND density continues when ultrasound was introduced for a short duration (Fig. 4-35d). However, when the grain was subjected to ultrasound for a prolonged period, there was a resurgence of GND density (Fig. 4-35e). This suggests that extended ultrasound exposure can lead to the reformation or re-entanglement of dislocations, possibly due to stress redistribution or interactions with neighbouring grains. This behaviour highlighted that while ultrasound can aid in dislocation annihilation, excessive exposure might sometimes result in dislocation reconfiguration rather than elimination. Grain 5 showed a striped pattern in Young's modulus, suggesting strain localization or dislocation movement (Fig. 4-29a). Alternating  $E \cdot m$  bands further indicated variations in slip activity (Fig. 4-29b). With the lowest Schmid factor among the grains, this grain was highly resistant to slip (Fig. 4-29c). Plastic strain remained zero (Fig. 4-29e), while shear stress distribution was heterogeneous, likely influenced by neighbouring grains (Fig. 4-29f).

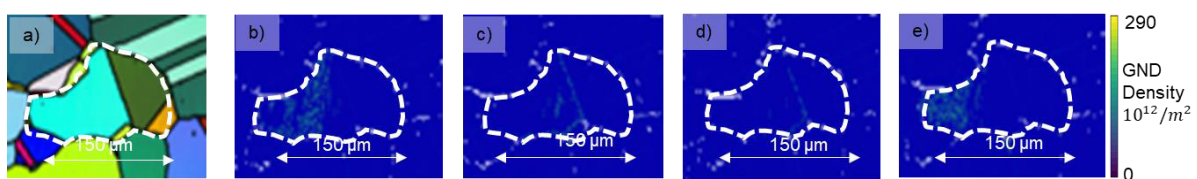


**Fig. 4-35** a) IPF (Inverse pole figure) and evolution of GND Density in Grain 7 b) N3\_A (initial), c) N3\_B (only Force 400N), d) N3\_C (20 $\mu\text{m}$ , ~100-200N, 50ms), e) N3\_D (20 $\mu\text{m}$ , ~100-200N, 5000ms).

The schematic diagram seen in Figure 4-36 provided depicts the changes in GND (Geometrically Necessary Dislocation) density across different grains under various conditions, including the initial state, applied force, force with short-duration ultrasound exposure, and force with prolonged ultrasound exposure.

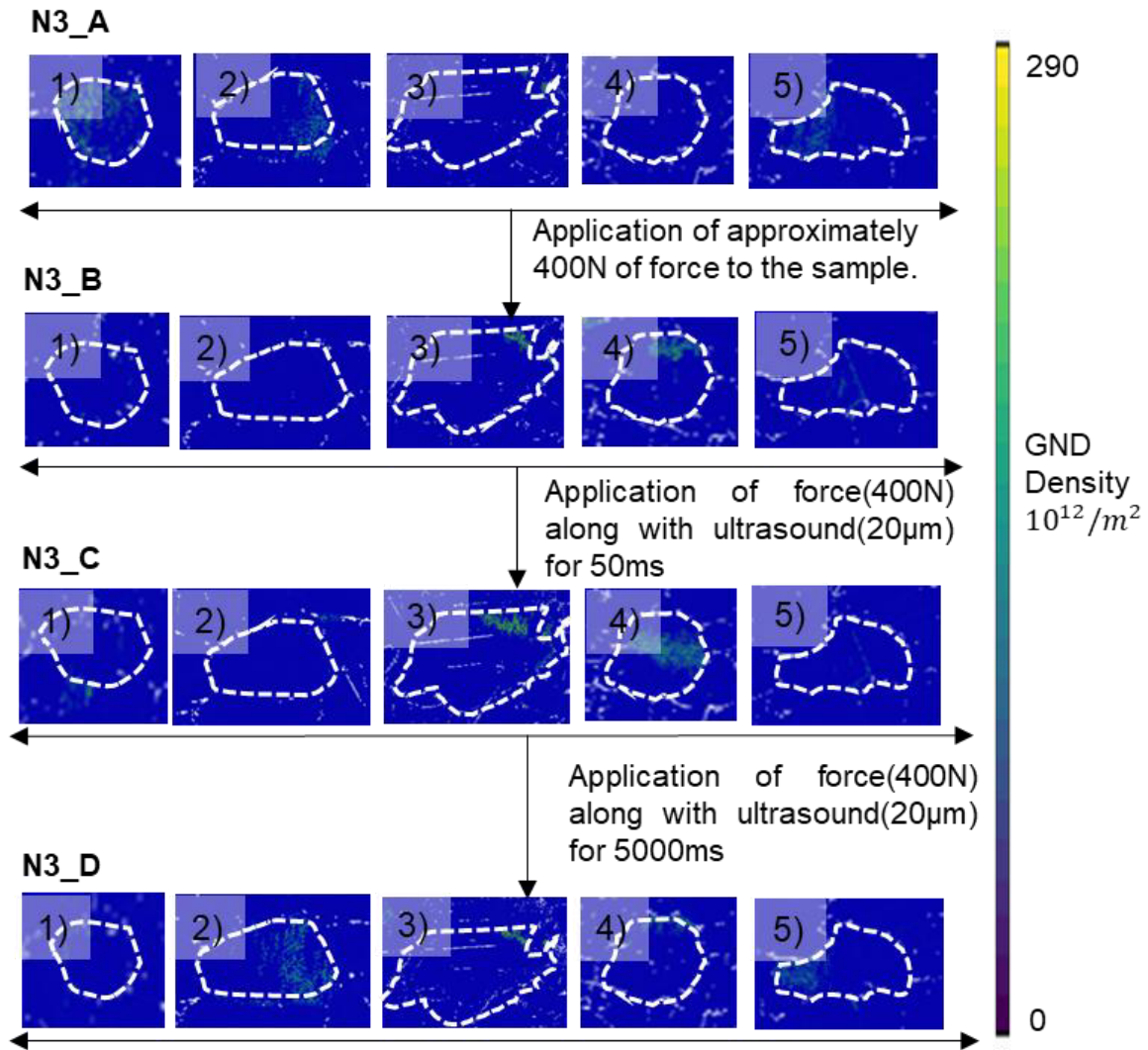


Fig. 4-36 Evolution of GND Density in IN617 Alloy Grains Under Mechanical and Ultrasonic Conditions for sample N3

From this analysis, we gain insight into how different grains in the IN617 alloy respond to applied force and ultrasound, highlighting key aspects of dislocation behaviour and strain evolution. The variation in GND density across grains emphasizes the influence of initial dislocation structures, grain orientation, and external conditions on deformation mechanisms.

A key observation was that grains such as Grain 1 and Grain 2 initially had noticeable GND densities, but when subjected to force alone, the dislocations were effectively eliminated. Interestingly, when ultrasound was introduced for a short duration along with force, these grains continue to exhibit zero GND density. However, for Grain 2, prolonged ultrasound exposure lead to a resurgence in GND density, suggesting that vibrational energy can, under certain conditions, promote dislocation generation or redistribution rather than simply aiding in

relaxation. In contrast, Grain 3 exhibited GND density when force was applied, with this effect persisting under short-duration ultrasound. However, with prolonged sonication for 5000ms ultrasound dislocation density was not seen much, suggesting that while initial dislocation motion was promoted, extended vibrational energy might lead to partial dislocation annihilation or rearrangement. Grain 4 presented a unique case where the initial GND density was not seen. Upon applying force, dislocation accumulation occurred primarily along the grain boundaries. With short-duration ultrasound exposure, the dislocations shift towards the grain centre, but with prolonged exposure, GND densities were seen along the grain boundaries. This pattern indicates that ultrasound not only influences dislocation density but also affects their spatial distribution, potentially playing a role in stress localization or grain boundary interactions. For Grain 5, the initial GND density was seen but when force alone was applied the presence of density was greatly reduced, further reducing with short-duration ultrasound. However, prolonged ultrasound exposure lead to an increase in GND density, similar to Grain 2. This suggests that while ultrasound can aid in dislocation movement and potential relaxation, extended exposure may cause dislocations to accumulate again, possibly due to secondary interactions.

Also the analysis highlights that different grains exhibit unique responses to applied force and ultrasound, underscoring the heterogeneous nature of deformation in polycrystalline materials. Ultrasound proved to be an effective tool for dislocation manipulation, aiding in dislocation annihilation in some grains while, in others, prolonged exposure lead to dislocation reformation, indicating a complex balance between stress relaxation and strain accumulation. Additionally, the redistribution of GND density between grain interiors and boundaries suggests that ultrasound plays a role in strain localization, which is crucial for understanding material fatigue and failure mechanisms.

With respect to Young's modulus, the product of Young's modulus and the Schmid factor ( $E \cdot m$ ), Schmid factor ( $m$ ), resulting shear stress (RSS), and plastic strain across all grains we can understand the mechanical behaviour of the material under applied stress, highlighting variations in deformation tendencies among different grains. Grains with moderate to high Young's modulus, such as Grain 1, Grain 2, and Grain 5, exhibited correspondingly high  $E \cdot m$  values, indicating significant internal stresses that could contribute to plastic deformation under sufficient loading. In contrast, some grains, such as Grain 3, contain regions with very low Young's modulus, suggesting a higher susceptibility to deformation despite currently exhibiting

no plastic strain. The presence of alternating Young's modulus and  $E.m$  values, as seen in Grain 4 and Grain 5, suggested localized strain accumulation and potential slip activity. Additionally, the heterogeneous shear stress distribution in these grains highlights the influence of neighbouring grains in shaping stress localization patterns. Grain 2, despite its high  $E.m$  value, remained strain-free, suggesting a resistance to deformation, whereas Grain 1 showed varying plastic strain, indicating possible slip initiation. Grain 3 and Grain 4 demonstrated distinct mechanical characteristics, with Grain 3 exhibiting uniform shear stress but no plastic strain, implying a stable deformation region, while Grain 4 showed stress variations influenced by its surroundings. The alternating stress levels in these grains suggested that external factors such as grain boundaries and neighbouring interactions play a crucial role in dictating mechanical responses. Grains 1, 3, and 5 exhibited low Schmid factors, meaning they were more resistant to slip and deformation. Grain 2 had a moderate Schmid factor, which suggested some potential for slip under stress. Grain 4 had the highest Schmid factor, making it the most likely to experience localized slip and plastic deformation.

Overall, this analysis underscores the heterogeneous nature of deformation across the microstructure, revealing that while some grains are predisposed to plastic deformation, others remain stable due to their inherent properties. The interplay of Young's modulus,  $E.m$  values, plastic strain distribution, and shear stress significantly influences the material's response to external loading.

The formation of slip bands can be observed with the help of SEM. The SEM image attached below illustrates the presence and pattern of slip bands at several spots, allowing for analysis of strain localization and dislocation activity within the material as discussed with the other samples

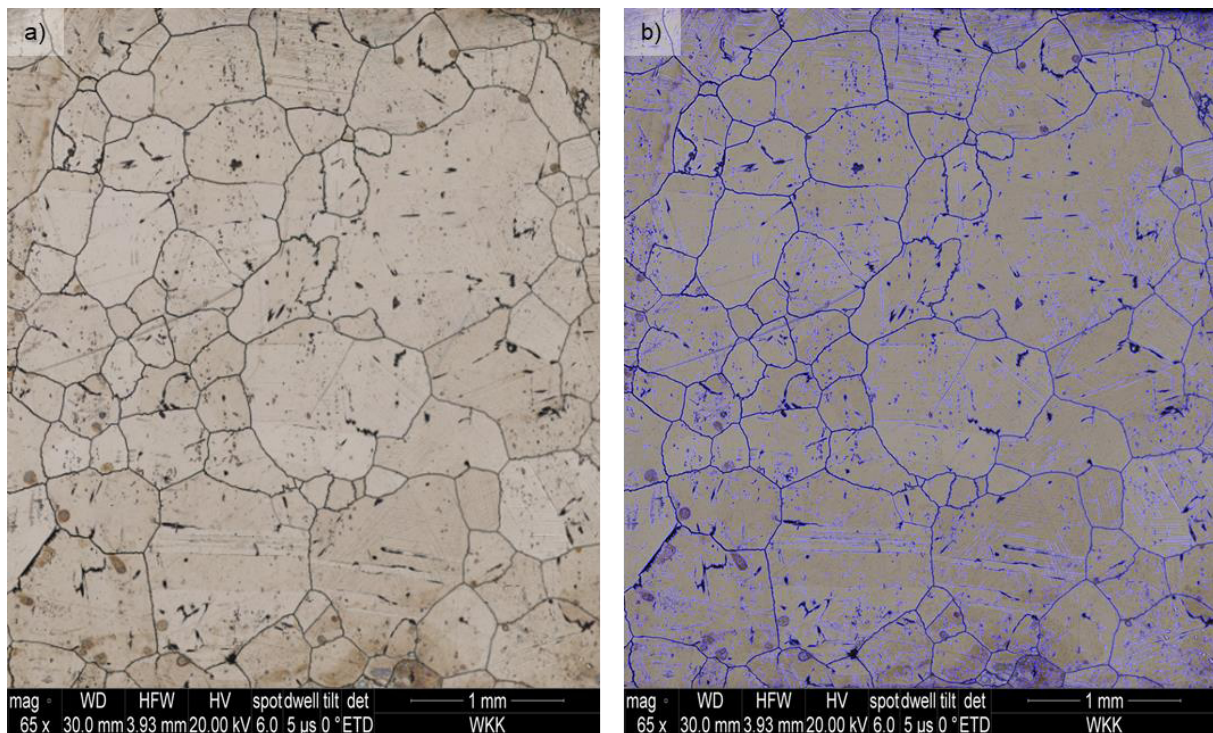


**Fig. 4-37 SEM image of Sample N3 a) With slip bands b) Highlighted slip bands**

The correlation between GND density observations and the mechanical parameters ( $E$ ,  $E \cdot m$  and  $m$ ) was evident in the deformation behaviour of different grains. Grains such as Grain 1 and Grain 2, which initially exhibited noticeable GND density, had their dislocations eliminated under force alone, aligning with their moderate to high  $E$  and  $E \cdot m$  values, indicating significant internal stresses. However, sonication for 5000ms led to a resurgence of GND density in Grain 2, suggesting that vibrations influenced dislocation redistribution rather than merely aiding in relaxation. This behaviour corresponded to its moderate  $m$ , which indicated a potential for slip initiation under stress. Grain 3, which displayed GND density under force and short-duration ultrasound but showed reduced dislocation density with prolonged sonication, exhibited a low  $E$  and no plastic strain, suggesting susceptibility to deformation despite its stability in shear stress. Grain 4, where dislocation accumulation initially occurred along the grain boundaries before shifting towards the centre and later redistributing along the boundaries, had the highest  $m$ , making it the most prone to localized slip and plastic deformation. Grain 5, which initially showed a reduction in GND density under force and short ultrasound but experienced an increase under prolonged sonication and also had alternating  $E$  and  $E \cdot m$  values, indicating localized strain accumulation and slip activity. The heterogeneous stress distribution in grains like Grain 4 and Grain 5 suggested that grain boundary interactions significantly influenced stress localization. Overall, the interplay between GND density changes and mechanical

properties confirmed that  $E$ ,  $E \cdot m$  and  $m$  governed dislocation behaviour, strain localization, and material stability under applied stress and ultrasound.

The sample N3 was identified as being thicker than one grain and exhibiting 3D effects due to the presence of significant grain boundaries and gradients, which were indicative of a possible variation in thickness when compared to sample N1 and N2. Additionally, a pronounced relief was observed, where some areas were perceived as raised compared to others. As a result, uneven stress distributions were expected to occur.

The analysis of samples N1, N2, and N3 provides an understanding of how plastic deformation and ultrasound influence geometrically necessary dislocations (GNDs) in crystalline materials. An important takeaway is the heterogeneous nature of deformation across different grains, where variations in initial GND density, grain size, and mechanical properties determine how each grain responds to applied force and ultrasound. The effect of neighbouring grains is also crucial, as local interactions influence stress distribution and slip activity. It was observed that grains with a high Young's modulus ( $E$ ) and Schmid factors ( $m$ ) had a greater tendency for slip, whereas grains with lower values of  $E$  and  $m$  were more resistant to deformation. Additionally, ultrasound played a significant role in dislocation annihilation. Some grains exhibited complete dislocation annihilation, while others showed GND reformation with prolonged sonication, highlighting that ultrasound can either promote annihilation or trigger new dislocation formation depending on the grain characteristics.

These findings align with the  $E \cdot m$  model, as GND behavior changed under varying external conditions. [52] The fact that some grains underwent plastic deformation while others remained stable supports the model's predictions. The presence of neighbouring grains influenced stress redistribution, creating regions of slip bands and confirming that grain boundary interactions dictate how stress propagates within the material. In Sample N3, the presence of 3D effects and thickness variations further reinforced the complexity of stress distribution, as uneven relief contributed to additional strain gradients.

Overall, this study provides insight into how GNDs are significantly influenced by applied ultrasound.

## 5. Conclusion

In the context of this work, the density and evolution of geometrically necessary dislocations (GNDs) in three different samples (N1, N2, N3) of IN617 alloy under various mechanical and vibrational conditions were examined in relation to the effect of ultrasonic treatment. A number of significant findings regarding the responses of various grains to external stresses through force and ultrasonic stimulation were obtained via Electron Backscatter Diffraction (EBSD) analysis and FEM modelling. From this analysis it was possible to understand the impact of ultrasound on GND Density, mechanical properties and deformation behaviour of the material. By analysing the correlation between GND density and mechanical parameters such as Young's modulus ( $E$ ), Schmid factor ( $m$ ), and the product of Young's modulus and Schmid factor ( $E \cdot m$ ) across all the samples, the heterogeneous nature of deformation in all the materials was revealed. It was observed that grains with high  $E$  and  $E \cdot m$  often exhibited prominent internal stresses and a higher likelihood of plastic deformation, as seen in grains such as Grain 1 and Grain 5 across all three samples (N1, N2, and N3). Pronounced GND density was observed in these grains under applied force, yet relaxation under ultrasound demonstrated that sonication effectively redistributed or eliminated dislocations. Similarly, grains that had high  $m$ , such as Grain 4, were susceptible to slipping and localized plastic strain, which corresponded with their observed shifts in GND density.

However, certain discrepancies were noted in some grains where  $E \cdot m$  observations did not align with the observed deformation behaviour. For instance, in Grain 2 of Sample 3, it was observed that after 5000 ms of sonication, GND density reappeared despite its initial elimination under applied force. The stress applied through ultrasound can aid in annihilation or trigger a new dislocation. Similarly, grains with low  $E$  and no plastic strain, such as Grain 3 in Sample 3, still exhibited GND density fluctuations, suggesting that external influences, such as neighbouring grains may contribute to stress accumulation and release.

Another factor influencing all the correlations mentioned above was the 3D nature of the samples, which are thicker than a single grain. Sample 3 in this research demonstrated this 3D nature, as explained in the results. This introduced added complexity, as it caused some underlying grains to be invisible from the surface and could also significantly influence the measured mechanical response. Discrepancies between  $E \cdot m$  values and observed GND behaviour in some grains could be due to the influence of sub-surface grains, where hidden interactions disrupted expected deformation patterns. This strongly indicated that while  $E$ ,  $E \cdot m$  and  $m$  are strong indicators of deformation behaviour, their relationship with GND density

could sometimes be affected by hidden stress distributions and grain-to-grain load transfer effects.

Overall, it was observed that grains with high  $E$  and  $E \cdot m$  showed significant internal stresses and a higher tendency for plastic deformation, while those with high  $m$  were more susceptible to slip and localized strain. However, discrepancies in some grains suggested that subsurface interactions and the properties of surrounding grains also played a critical role in deformation behaviour. The effect of ultrasound on GND density varied across different grains, indicating that sonication facilitated stress relaxation and dislocation in some cases while inducing local strain hardening in others. In some cases, prolonged sonication for about 5000 ms led to partial elimination of GNDs rather than complete removal, as evidenced by some examples where GND density reappeared after initial annihilation. This study underscored the complex interplay between ultrasonic treatment, mechanical properties, and dislocation dynamics in IN617 alloy. The findings confirm that the superimposition of force and Sonics leads to a more pronounced plastic strain with various samples that were tested. The observed annihilation of GNDs aligns with the hypothesis, as shorter energy induction durations resulted in reduced GND annihilation. Additionally, the mechanical properties of individual grains and their neighbours ( $E$ ,  $m$ , and  $E \cdot m$ ) significantly influenced the onset of plastic strain and shear stress distribution. The observed changes in GND density support the applicability of the  $Em$ -model, reinforcing its relevance in describing plastic deformation behavior under these conditions.

Future research could focus on exploring different ultrasonic parameters, such as frequency, amplitude, and duration, to better understand sonication-induced stress relaxation and dislocation behaviour. Another promising approach could be the development of more advanced FEM models that incorporate grain-to-grain interactions and subsurface effects, improving the understanding of deformation behavior in alloys with complex microstructures. Furthermore, applying similar analyses to other nickel-based super-alloys or different material classes could help validate the general applicability of the findings and refine ultrasonic treatment techniques for industrial applications.

## 6. Literature

- [1] Chen Y, Xu M, Zhang T, Xie J, Wei K, Wang S, Yin L, He P (2022) Grain refinement and mechanical properties improvement of Inconel 625 alloy fabricated by ultrasonic-assisted wire and arc additive manufacturing. *Journal of Alloys and Compounds* 910:164957. doi:10.1016/j.jallcom.2022.164957
- [2] Zhao T, Zhang S, Wang ZY, Zhang CH, Zhang DX, Wang NW, Wu CL (2022) Cavitation erosion/corrosion synergy and wear behaviors of nickel-based alloy coatings on 304 stainless steel prepared by cold metal transfer. *Wear* 510-511:204510. doi:10.1016/j.wear.2022.204510
- [3] Zhou Z, Yao C-F, Zhao Y, Wang Y, Tan L (2021) Effect of ultrasonic impact treatment on the surface integrity of nickel alloy 718. *Adv. Manuf.* 9(1):160–171. doi:10.1007/s40436-020-00329-8
- [4] Yang L, Yang L (2024) Wave-Particle Duality of Ultrasound: Acoustic Softening Explained by Particle Treatment of Ultrasonic Wave. arXiv
- [5] Song P, Li W-B, Zheng Y, Song J-P, Jiang X-C, Yan B-Y (2020) Study on Plastic Deformation Behavior of Mo-10Ta under Ultra-High Strain Rate. *Metals* 10(9):1153. doi:10.3390/met10091153
- [6] Ruirun C, Deshuang Z, Tengfei M, Hongsheng D, Yanqing S, Jingjie G, Hengzhi F (2017) Effects of ultrasonic vibration on the microstructure and mechanical properties of high alloying TiAl. *Sci Rep* 7:41463. doi:10.1038/srep41463
- [7] (2015) *Power Ultrasonics*. Elsevier
- [8] Phan V-T, Zhang X, Li Y, Oskay C (2017) Microscale modeling of creep deformation and rupture in Nickel-based superalloy IN 617 at high temperature. *Mechanics of Materials* 114:215–227. doi:10.1016/j.mechmat.2017.08.008
- [9] Zhang M, Wang Y, Wang D, Hassan Mohsan AU, Yang X, Gao X, Xu J, Cheng D, Zhang G (2025) Grain refinement and mechanical properties improvement of AlCuFeCoNi high-entropy alloy coatings fabricated by resonant ultrasonic assisted laser cladding. *Optics & Laser Technology* 182:112233. doi:10.1016/j.optlastec.2024.112233
- [10] Kaoumi D, Hrutkay K (2014) Tensile deformation behavior and microstructure evolution of Ni-based superalloy 617. *Journal of Nuclear Materials* 454(1-3):265–273. doi:10.1016/j.jnucmat.2014.08.003

- [11] Jun C, Kuaishe W, Wen W (2016) Characterization of High Temperature Deformation Behavior of BFe10-1-2 Cupronickel Alloy Using Constitutive Equation and Processing Map. *Rare Metal Materials and Engineering* 45(10):2549–2554. doi:10.1016/S1875-5372(17)30032-2
- [12] Zhang X, Oskay C (2016) Polycrystal plasticity modeling of nickel-based superalloy IN 617 subjected to cyclic loading at high temperature. *Modelling Simul. Mater. Sci. Eng.* 24(5):55009. doi:10.1088/0965-0393/24/5/055009
- [13] Salari S, Rahman MS, Polycarpou AA, Beheshti A (2020) Elevated temperature mechanical properties of Inconel 617 surface oxide using nanoindentation. *Materials Science and Engineering: A* 788:139539. doi:10.1016/j.msea.2020.139539
- [14] Li L, Khraishi T (2023) An Investigation of Spiral Dislocation Sources Using Discrete Dislocation Dynamics (DDD) Simulations. *Metals* 13(8):1408. doi:10.3390/met13081408
- [15] Wei C, Tang S, Kong Y, Shuai X, Mao H, Du Y (2023) Atomic-Scale Insights into the Deformation Mechanism of the Microstructures in Precipitation-Strengthening Alloys. *Materials (Basel)* 16(5). doi:10.3390/ma16051841
- [16] Le Q, Domenico J, Salerno K, Stiles D (2023) Atomic-Scale Modeling for Materials and Chemistry. *Atomic-Scale Modeling for Materials and Chemistry*
- [17] Zhou X Atomic Scale Dynamics of Sustainable Materials. Max planck institute for sustainable materials. [https://www.mpie.de/4955274/atomic\\_scale\\_dynamics\\_of\\_sustainable\\_materials](https://www.mpie.de/4955274/atomic_scale_dynamics_of_sustainable_materials)
- [18] Special Metals Corporation (2005) INCONEL 617. <https://www.specialmetals.com/documents/technical-bulletins/inconel/inconel-alloy-617.pdf>
- [19] Narayan singh A (2019) Study of Deformation and Fracture Behaviour of Alloy 617. Doctor of Philosophy
- [20] High Temperature Metals Inconel 617 - Technical Data for High-Temperature Alloys. <https://www.hightempmetals.com/techdata/hitempInconel617data.php>
- [21] Saksena A, Gault B Atomic-scale analytical imaging to understand deformation mechanisms in superalloys. Max planck institute for sustainable materials. [https://www.mpie.de/3832396/atomic-scale\\_analytical\\_imaging](https://www.mpie.de/3832396/atomic-scale_analytical_imaging)

- [22] Smith TM, Kantzos CA, Zarkevich NA, Harder BJ, Heczko M, Gradl PR, Thompson AC, Mills MJ, Gabb TP, Lawson JW (2023) A 3D printable alloy designed for extreme environments. *Nature* 617(7961):513–518. doi:10.1038/s41586-023-05893-0
- [23] Messerschmidt U (2010) Dislocation Motion. In: Hull R, Jagadish C, Osgood RM, Parisi J, Wang Z, Warlimont H, Messerschmidt U (Hrsg) *Dislocation Dynamics During Plastic Deformation*, Bd 129. Springer Berlin Heidelberg, Berlin, Heidelberg, S 73–154
- [24] Ma Y, Liu G, Yang S, Chen R, Xu S, Shen Y (2024) Effects of Strain Rate on the GND Characteristics of Deformed Polycrystalline Pure Copper. *Metals* 14(5):582. doi:10.3390/met14050582
- [25] Schwartz AJ, Kumar M, Adams BL (2000) *Electron Backscatter Diffraction in Materials Science*. Springer US, Boston, MA
- [26] Jang MJ, Praveen S, Sung HJ, Bae JW, Moon J, Kim HS (2018) High-temperature tensile deformation behavior of hot rolled CrMnFeCoNi high-entropy alloy. *Journal of Alloys and Compounds* 730:242–248. doi:10.1016/j.jallcom.2017.09.293
- [27] Zhang S, Romo S, Giorjao RA, Leao PB, Ramirez AJ (2022) EBSD analysis of strain distribution and evolution in ferritic-Pearlitic steel under cyclic deformation at intermediate temperature. *Materials Characterization* 193:112293. doi:10.1016/j.matchar.2022.112293
- [28] Li Z, Ge J, Kong B, Luo D, Wang Z, Zhang X (2023) Strain Rate Dependence and Recrystallization Modeling for TC18 Alloy during Post-Deformation Annealing. *Materials (Basel)* 16(3). doi:10.3390/ma16031140
- [29] Despax L, Vidal V, Delagnes D, Dehmas M, Matsumoto H, Velay V (2020) Influence of strain rate and temperature on the deformation mechanisms of a fine-grained Ti-6Al-4V alloy. *Materials Science and Engineering: A* 790:139718. doi:10.1016/j.msea.2020.139718
- [30] Zhang X, Tung Van P, Caglar O (2016) Microstructural creep, fatigue and creep-fatigue modeling of Nickel-based superalloy Inconel 617 at high temperature - 18506
- [31] Tian Z, Zhang T, Wang Z, Xie Z, Fang F (2023) Dynamic tensile deformation of Al<sub>0.1</sub>Ti<sub>0.1</sub>CoCrFeNi high entropy alloy with heterogeneous grain structure. *Journal of Alloys and Compounds* 968:172092. doi:10.1016/j.jallcom.2023.172092
- [32] Nye J (1953) Some geometrical relations in dislocated crystals. *Acta Metallurgica* 1(2):153–162. doi:10.1016/0001-6160(53)90054-6

- [33] Randle V (2008) Application of EBSD to the analysis of interface planes: evolution over the last two decades. *J Microsc* 230(Pt 3):406–413. doi:10.1111/j.1365-2818.2008.02000.x
- [34] Ruggles TJ, Fullwood DT (2013) Estimations of bulk geometrically necessary dislocation density using high resolution EBSD. *Ultramicroscopy* 133:8–15. doi:10.1016/j.ultramic.2013.04.011
- [35] Pantleon W (2008) Resolving the geometrically necessary dislocation content by conventional electron backscattering diffraction. *Scripta Materialia* 58(11):994–997. doi:10.1016/j.scriptamat.2008.01.050
- [36] Hansen N (2001) The Effect of Grain Size and Strain on the The Effect of Grain Size and Strain on the Density of Geometrically Necessary Dislocations 49(14):3457–3468
- [37] Field DP, Trivedi PB, Wright SI, Kumar M (2005) Analysis of local orientation gradients in deformed single crystals. *Ultramicroscopy* 103(1):33–39. doi:10.1016/j.ultramic.2004.11.016
- [38] Randle V (2009) Electron backscatter diffraction: Strategies for reliable data acquisition and processing. *Materials Characterization* 60(9):913–922. doi:10.1016/j.matchar.2009.05.011
- [39] Kröner E (1958) *Kontinuumstheorie Der Versetzungen Und Eigenspannungen*
- [40] Eaves AE, Smith AW, Waterhouse WJ, Sansome DH (1975) Review of the application of ultrasonic vibrations to deforming metals. *Ultrasonics* 13(4):162–170. doi:10.1016/0041-624X(75)90085-2
- [41] Mao Q, Coutris N, Rack H, Fadel G, Gibert J (2020) Investigating ultrasound-induced acoustic softening in aluminum and its alloys. *Ultrasonics* 102:106005. doi:10.1016/j.ultras.2019.106005
- [42] Zhou X, Mianroodi JR, Da Kwiatkowski Silva A, Koenig T, Thompson GB, Shanthraj P, Ponge D, Gault B, Svendsen B, Raabe D (2021) The hidden structure dependence of the chemical life of dislocations. *Sci Adv* 7(16). doi:10.1126/sciadv.abf0563
- [43] ZHUANG X, WANG J, ZHENG H, ZHAO Z (2015) Forming mechanism of ultrasonic vibration assisted compression. *Transactions of Nonferrous Metals Society of China* 25(7):2352–2360. doi:10.1016/S1003-6326(15)63850-X
- [44] Malygin GA (2000) Acoustoplastic effect and the stress superimposition mechanism. *Phys. Solid State* 42(1):72–78. doi:10.1134/1.1131170

- [45] Zhilyaev AP, Samigullina AA, Medvedeva AE, Sergeev SN, Cabrera JM, Nazarov AA (2017) Softening and hardening of ECAP nickel under ultrasonic treatment. *Materials Science and Engineering: A* 698:136–142. doi:10.1016/j.msea.2017.05.054
- [46] Hung J-C, Hung C (2005) The influence of ultrasonic-vibration on hot upsetting of aluminum alloy. *Ultrasonics* 43(8):692–698. doi:10.1016/j.ultras.2005.03.001
- [47] Blaha F, Langenecker B (1955) Dehnung von Zink-Kristallen unter Ultraschalleinwirkung. *Naturwissenschaften* 42(20):556. doi:10.1007/BF00623773
- [48] Abedini R, Abdullah A, Alizadeh Y (2017) Ultrasonic hot powder compaction of Ti-6Al-4V. *Ultrasonics Sonochemistry* 37:640–647. doi:10.1016/j.ultsonch.2017.02.012
- [49] Djavanroodi F, Ahmadian H, Koohkan K, Naseri R (2013) Ultrasonic assisted-ECAP. *Ultrasonics* 53(6):1089–1096. doi:10.1016/j.ultras.2013.02.003
- [50] YAO L, HAO H, JI S, FANG C, ZHANG X (2011) Effects of ultrasonic vibration on solidification structure and properties of Mg-8Li-3Al alloy. *Transactions of Nonferrous Metals Society of China* 21(6):1241–1246. doi:10.1016/S1003-6326(11)60848-0
- [51] Gindin IA, Malik GN, Neklyudov IM, Rozumnyi OT (1972) Effect of ultrasonic vibrations on the parameters of the hardening curve for copper single crystals. *Soviet Physics Journal* 15(2):192–196. doi:10.1007/BF00819431
- [52] Mukhametgalina AA, Samigullina AA, Sergeyev SN, Zhilyaev AP, Nazarov AA, Zagidullina YR, Parkhimovich NY, Rubanik VV, Tsarenko YV (2017) Effect of ultrasonic treatment on the structure and microhardness of ultrafine grained nickel processed by high pressure torsion. *LoM* 7(2):85–90. doi:10.22226/2410-3535-2017-2-85-90
- [53] Rusinko A (2011) Analytical description of ultrasonic hardening and softening. *Ultrasonics* 51(6):709–714. doi:10.1016/j.ultras.2011.02.003
- [54] Fatyukhin DS, Nigmatzyanov RI, Prikhodko VM, Sukhov AV, Sundukov SK (2023) Comprehensive Estimation of Changes in the Microgeometry of Steel 45 by Ultrasonic Plastic Deformation with a Free Deforming Element. *Metals* 13(1):114. doi:10.3390/met13010114
- [55] Engel B, Beck T, Moch N, Gottschalk H, Schmitz S (2018) Effect of local anisotropy on fatigue crack initiation in a coarse grained nickel-base superalloy. *MATEC Web Conf.* 165:4004. doi:10.1051/mateconf/201816504004
- [56] Nanoscience Instruments (2025) Scanning Electron Microscopy. <https://www.nanoscience.com/techniques/scanning-electron-microscopy/>

- [57] ThermoFisher Scientific (2025) Scanning Electron Microscope (SEM) - Materials Science. <https://www.thermofisher.com/de/de/home/materials-science/learning-center/applications/scanning-electron-microscope-sem-electron-column.html>
- [58] Aryal S (2025) Scanning Electron Microscope (SEM) - Microbiology Techniques. Microbe Notes. <https://microbenotes.com/scanning-electron-microscope-sem/>
- [59] Lai SY, Brown A, Vickerman JC, Briggs D (1986) The relationship between electron and ion induced secondary electron imaging: A review with new experimental observations. *Surf. Interface Anal.* 8(3):93–111. doi:10.1002/sia.740080302
- [60] Davis JR (2000) Nickel, Cobalt and Their Alloys
- [61] Reed RC (2009) The Superalloys. Cambridge University Press
- [62] Kewther MA, Yilbas BS, Hashmi M (2001) Tensile and fatigue testing of Inconel 617 alloy after heat treatment and electrochemical tests. *Industrial Lubrication and Tribology* 53(3):112–118. doi:10.1108/00368790110390201
- [63] Taylor M, Ding R, Mignanelli P, Hardy M (2022) Oxidation behaviour of a developmental nickel-based alloy and the role of minor elements. *Corrosion Science* 196:110002. doi:10.1016/j.corsci.2021.110002
- [64] Pollock TM, Tin S (2006) Nickel-Based Superalloys for Advanced Turbine Engines: Chemistry, Microstructure and Properties. *Journal of Propulsion and Power* 22(2):361–374. doi:10.2514/1.18239
- [65] Dassault Systèmes (2025) Abaqus - Simulation Software. In: Dassault Systèmes. <https://www.3ds.com/products/simulia/abaqus>
- [66] Geuzaine C, Remacle J-F (2009) Gmsh: A 3-D finite element mesh generator with built-in pre- and post-processing facilities. *Numerical Meth Engineering* 79(11):1309–1331. doi:10.1002/nme.2579
- [67] MathWorks (2025) MATLAB - Product Information. [https://de.mathworks.com/products/matlab.html?s\\_tid=hp\\_products\\_matlab](https://de.mathworks.com/products/matlab.html?s_tid=hp_products_matlab)
- [68] MTEX Toolbox (2025) MTEX - A Toolbox for the Processing and Analysis of Texture Data. <https://github.com/mtex-toolbox/mtex>
- [69] OriginLab (2025) OriginLab Software - Data Analysis and Graphing. <https://www.originlab.com/>
- [70] Sorby H (2005) Buehler's Guide to Materials Preparation. - The Science Behind Materials Preparation and Analysis
- [71] Vort GH Metallographic Preparation for Electron Backscattered Diffraction 5(2)

- [72] Hong,R. (2024). A review of the preparation methods and techniques of electron backscatter diffraction (EBSD) samples. Advances in Engineering Innovation,10,20-25. doi:10.54254/2977-3903/10/2024099

## 7. Appendix

# Stepwise Guide to Perform GND Analysis Using EBSD Data

Akaash Chakkaravarthy

[Chakkara@rhrk.uni-kl.de](mailto:Chakkara@rhrk.uni-kl.de)

Understanding material deformation mechanisms, such as strain localization and microstructure evolution, often requires detailed analysis of geometrically necessary dislocations (GNDs). GND analysis provides critical insights into the distribution of strain gradients, crystal lattice distortions, and material behaviour under various conditions. Obtaining accurate and reliable data for GND analysis is the foundational step in conducting a robust investigation.

This manual aims to guide users through the stepwise process of obtaining high-quality data for GND analysis. It is designed for researchers, engineers, and analysts who require a systematic approach to data collection, whether from experimental methods such as Electron Backscatter Diffraction (EBSD) or other advanced techniques. By following this manual, users will ensure that the data they obtain is suitable for subsequent analysis, leading to reliable and meaningful results.

Key objectives of this manual include:

- Providing a clear, step-by-step methodology for data acquisition.
- Highlighting best practices to ensure data accuracy and reproducibility.
- Addressing common challenges and troubleshooting tips.

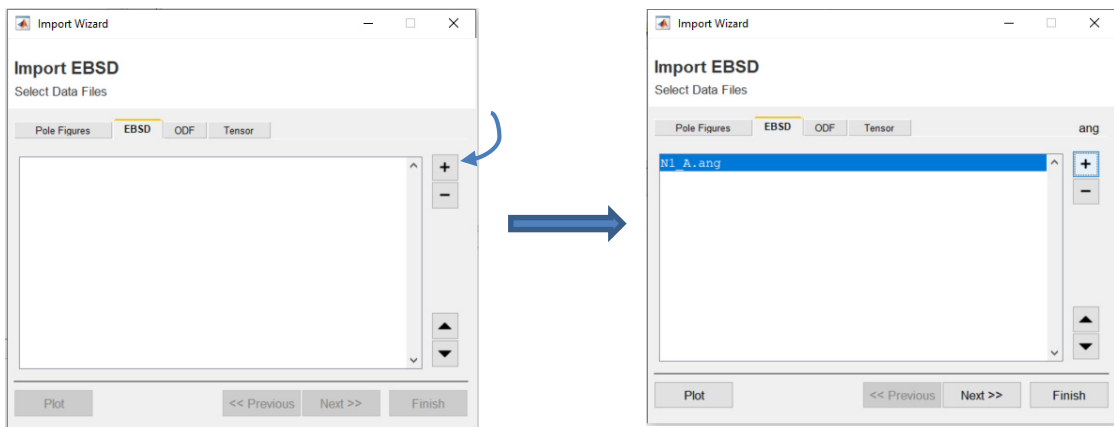
By adhering to the guidelines in this manual, users can enhance the efficiency and reliability of their GND data collection process, paving the way for precise material characterization and deeper scientific insights.

*\*This manual is created using a sample EBSD data NI\_A as an example. Replace NI\_A with the appropriate data and file name specific to your use case.*

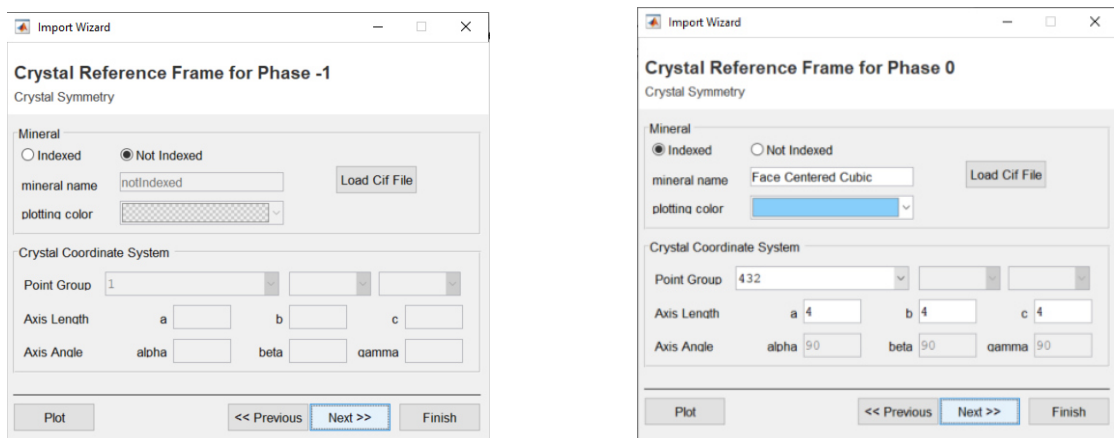
1. First install MATLAB.
2. Download the latest version of MTEX from:
  - a. [MTEX toolbox](#)
3. Unzip the folder to somewhere on your computer. A good place might be your Documents folder.
4. In MATLAB, navigate to the mtex folder you just unzipped and set the directory and run the command `startup_mtex`. If you get some links to import data, then MTEX is correctly installed.

```
>> startup_mtex
MTEX 5.11.2 (show documentation)
Import pole figure data
Import EBSD data
Check Installation
Uninstall MTEX
```

5. Assuming we have EBSD data in .ang format, it can be imported by using the 'Import EBSD Data' option. Upon clicking that link, we get the following.

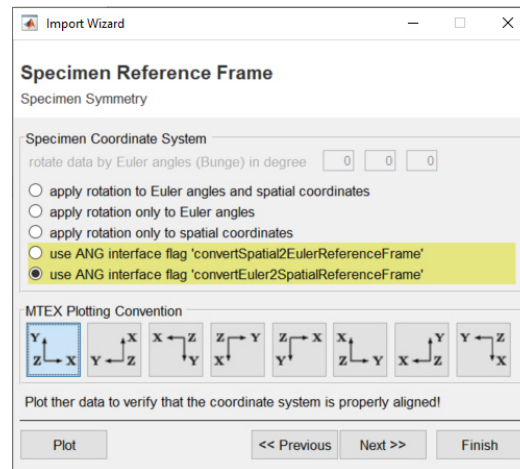


6. After adding the .ang file, click 'Next.' A tab labelled 'Crystal Reference Frame for Phase - 1' will appear. Simply proceed by clicking 'Next' again.
7. The next tab, labelled 'Crystal Reference Frame for Phase - 0,' will open. Continue by clicking 'Next' once more.

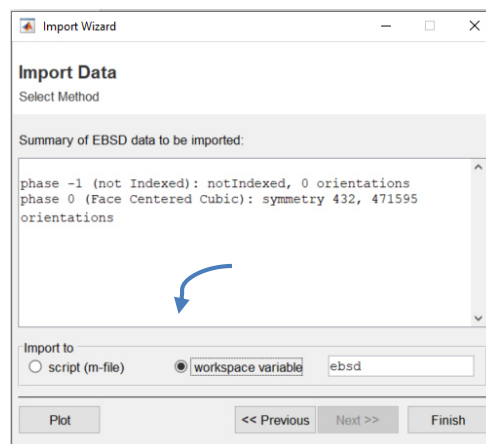


8. The next tab is the Specimen Reference Frame, which defines the orientation of the sample relative to the microscope. Correctly setting this frame ensures that all

derived orientations, maps, and analyses are accurate and meaningful. Select the desired MTEX plotting conversion and proceed by clicking ‘Next.’



9. Next, the 'Import Data' tab appears. Ensure that the 'Import to' option is set to 'Workspace Variable.' Upon clicking 'Finish,' the EBSD data from the selected .ang file will be loaded into the MATLAB workspace, where it can be accessed and analysed.



10. After extracting EBSD data from the .ang file, the data is processed to generate .geo files, which are subsequently converted into .inp files for use in ABAQUS. This process requires following a series of sequential steps to ensure proper format conversion and coMPatibility.
11. Ensure that MTEX2Gmsh is installed. You can do this by executing Install\_MTEX2Gmsh in the command window. For more information about this toolbox, visit [MTEX2Gmsh Documentation](#).
12. After installation of MTEX2Gmsh. The provided MATLAB code can be used to obtain desired .geo file.

```
[grains,ebbsd('indexed').grainId] = calcGrains(ebbsd('indexed'));
ebbsd(grains(grains.grainSize<=50)) = [];
[grains,ebbsd('indexed').grainId] = calcGrains(ebbsd('indexed'));
F = splineFilter;
ebbsd = smooth(ebbsd('indexed'),F,'fill',grains);
```

```
[grains,ebsd('indexed').grainId] = calcGrains(ebsd('indexed'));
[grains,ebsd.grainId,ebsd.mis2mean] = calcGrains(ebsd('indexed'),'angle',15*degree);
grains = grains.smooth(15);
G=gmsGeo(grains);
savegeo(G,'N1_A.geo');
```

13. Open the .geo file created in notepad and edit the following parameters

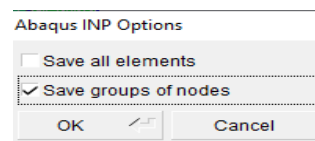
th=50;

e\_def=20

and Save the file.

14. Open the Gmsh software, load the saved .geo file, and export it as an .inp file.

During the export process, a dialog box will appear; ensure that the "Save groups of nodes" option is selected.



15. A .txt file is also generated, which represents the Euler angles (Phi1, Phi, and Phi2). Copy these angles into the 0\_0 section of the 2103009\_N4\_EulerwinkelUmrechner.xlsx file. Then, copy the data from the 0\_0 RotMat section into a new Notepad file. Save this file, and it will serve as the .ori file.

16. Open the saved .inp file, edit the first and last lines as mentioned below, and then save the file.

The first line should be:

```
*Part, name=N1_A
```

```
*NODE
```

The last line should be

```
*End Part
```

17. The next step is to run the script P3\_ori\_in\_inp.py in Spyder. Ensure that the .inp file, .ori file, and the Python script are all located in the same folder before executing the script.

18. After executing the program, provide the required details as prompted. This will generate a new .inp file with the added orientation information.

```
Geben Sie den Name ein: N1_A
Anzahl der Koerner?482
Geben Sie das Material ein:IN
```

19. Before using the .ori file in Abaqus, make the following changes:

- Replace the word volume with Grain\_ throughout the file.
- Ensure that Grain\_ is consistent and does not appear as Grain\_\_ or with any additional underscores. These adjustments are crucial to avoid errors during further calculations.

20. Use Remote Desktop Connection(`elwe<x>.rhrk.uni-kl.de(<x>=1,...,4)`) to access the system and launch the Abaqus software. Then, load the .inp file with orientation by navigating to:

File → Import → Model → Select the .inp file.

21. Select Module → Part

22. Select Module → Property → create material

- Provide the Name as 'IN'
- Select General → Density and Enter the value as 8.5E-9
- Select Mechanical → Elasticity → Elastic and select the type to be orthotropic and enter the values

280274	190988	280274	190988	190988	280274	127064	127064	127064
--------	--------	--------	--------	--------	--------	--------	--------	--------

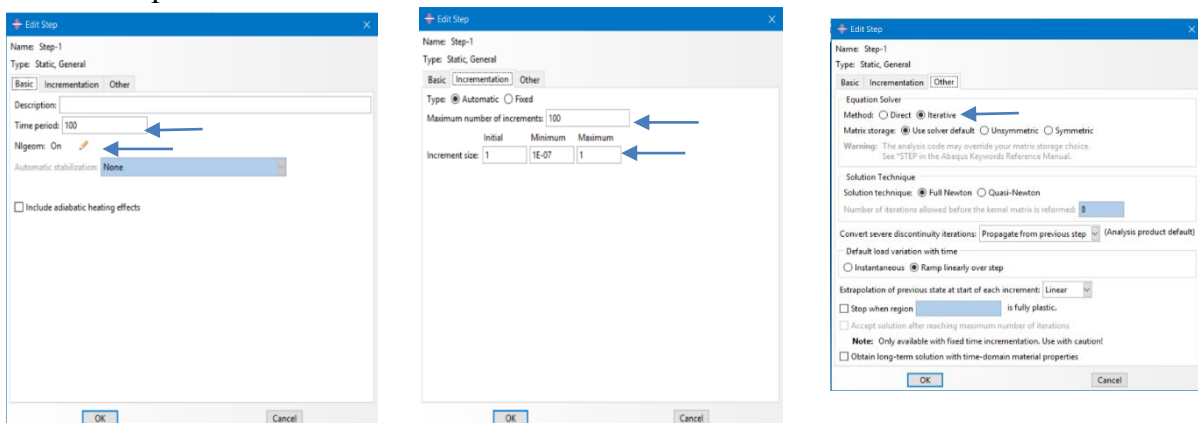
- Select Mechanical → Plasticity → plastic and select the Hardening to be Isotropic and enter the values

	Yield stress	Plastic strain
1	300	0
2	400	0.0053
3	470	0.02
4	500	0.03
5	820	0.53

- Click ok

23. Select Module → Assembly → Create Instance → Ok

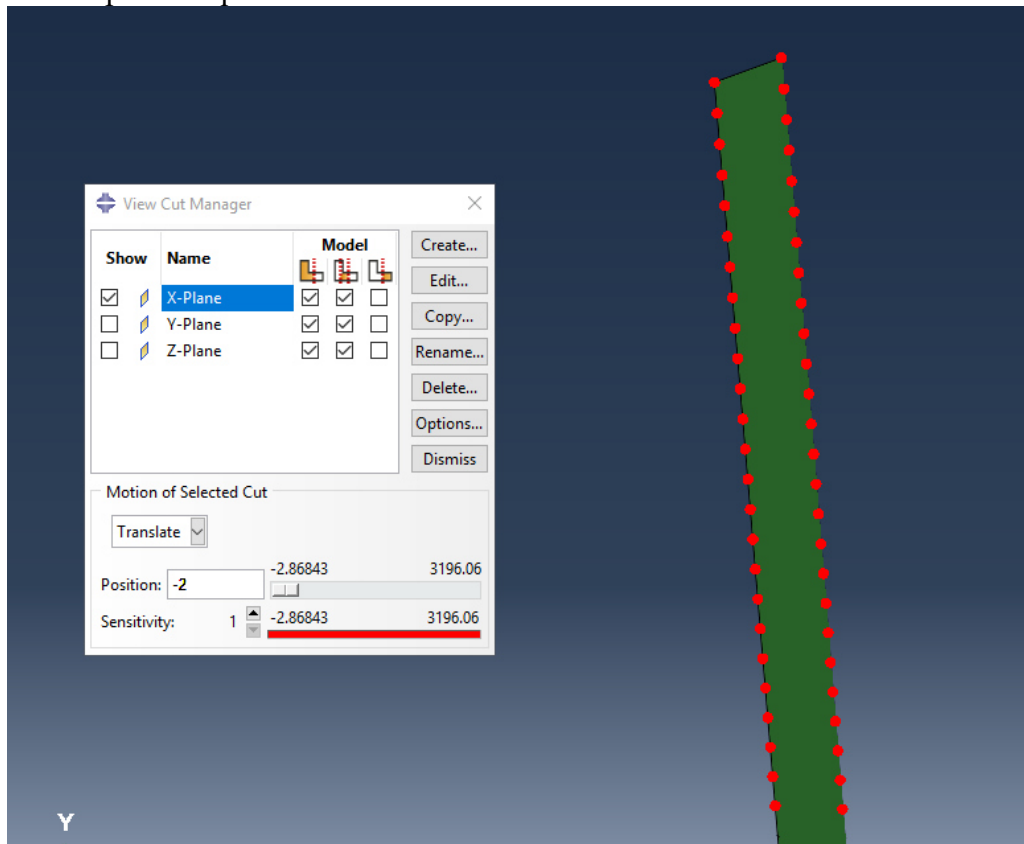
24. Select Module → Step → Create step → Continue and make sure the following options are selected



25. Select Module → Load → Create boundary condition

- Provide a name COMPRESSION LEFT
- Select the category to be mechanical
- Select Type for the selected step to be Displacement/Rotation.

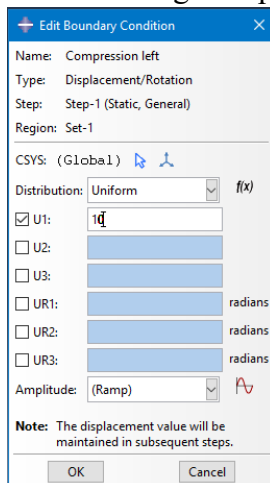
- Locate and click on Activate/Deactivate View Cut Manager in tools. A tab as see below will appear. Adjust the Position values to isolate and display only the edge portion of the sample as required.



- After selecting the edges, press Done

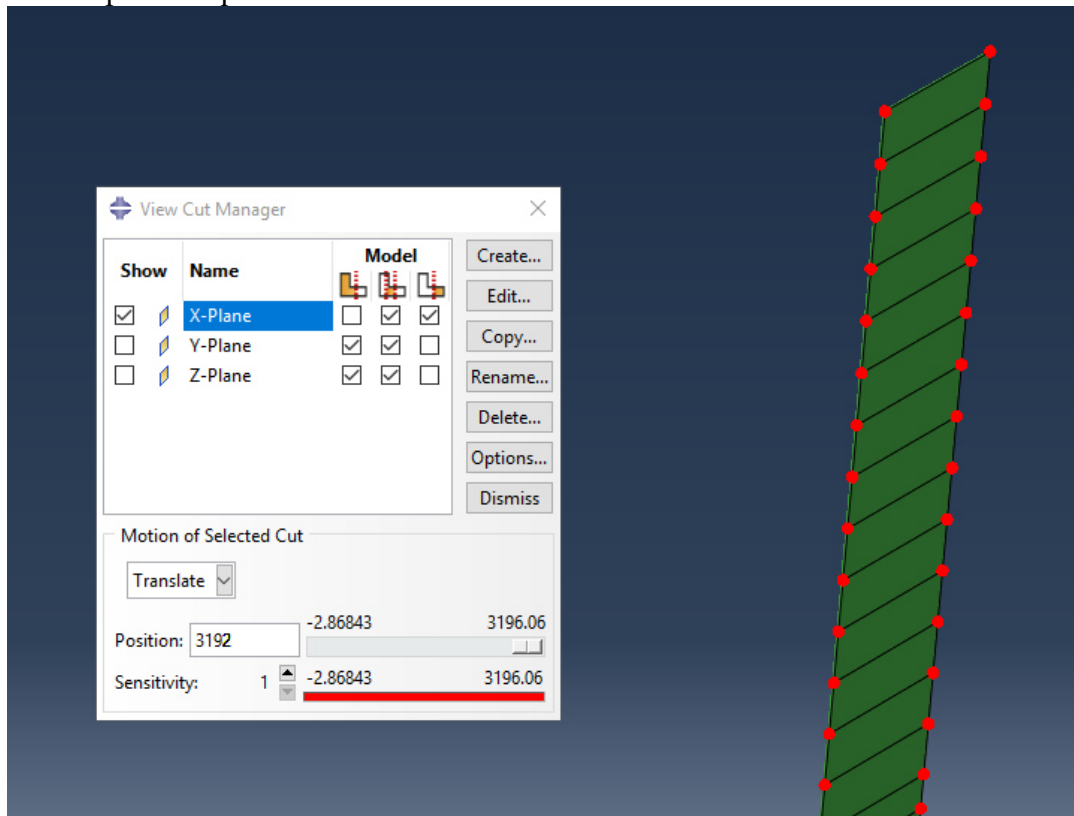


- The following tab appears and the mentioned data should be entered.



- Click Ok, Now Boundary Condition 1 is created. Similarly, we have to create Boundary conditions for all other edges.
- 26. Select Module → Load → Create boundary condition
- Provide a name FIX RIGHT
- Select the category to be mechanical
- Select Type for the selected step to be Displacement/Rotation.

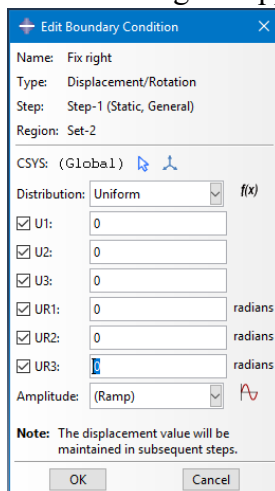
- Locate and click on Activate/Deactivate View Cut Manager in tools. A tab as see below will appear. Adjust the Position values to isolate and display only the edge portion of the sample as required.



- After selecting the edges, press Done

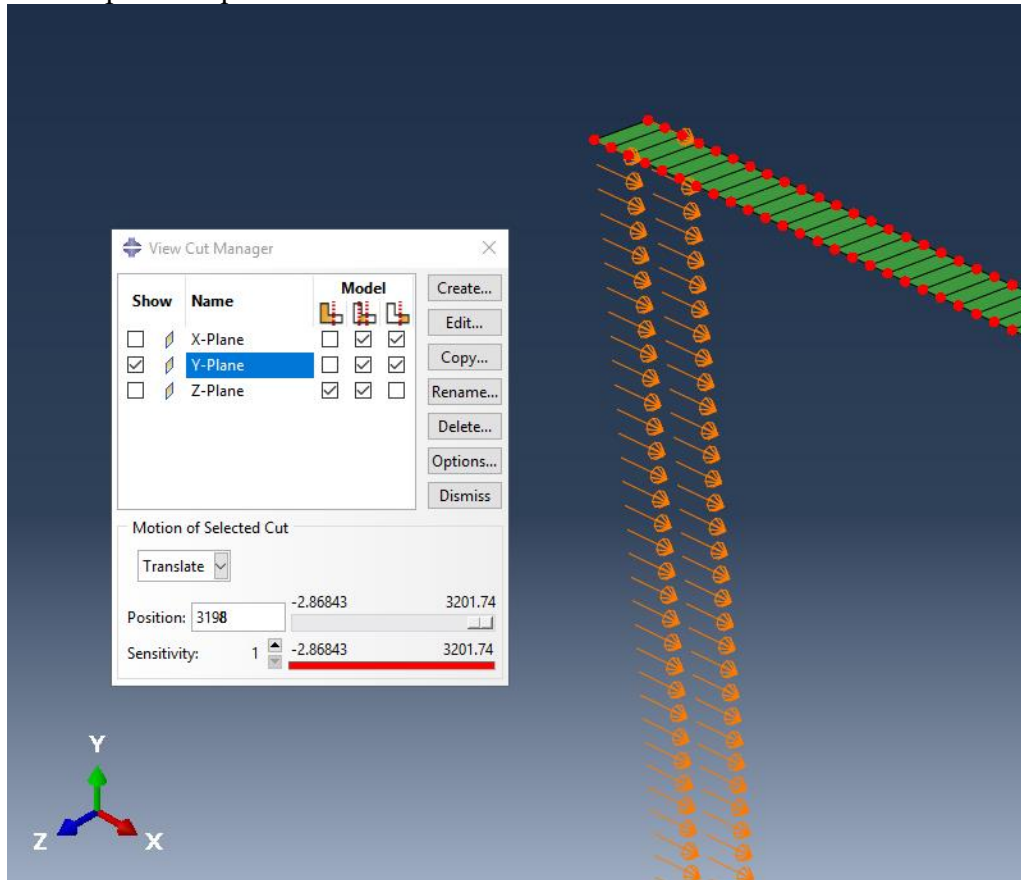


- The following tab appears and the mentioned data should be entered.



- Click Ok, Now Boundary Condition 2 is created. Similarly, we have to create Boundary conditions for all other edges.
- 27. Select Module → Load → Create boundary condition
- Provide a name FIX TOP
- Select the category to be mechanical
- Select Type for the selected step to be Displacement/Rotation.

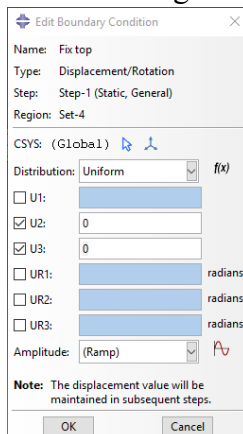
- Locate and click on Activate/Deactivate View Cut Manager in tools. A tab as see below will appear. Adjust the Position values to isolate and display only the edge portion of the sample as required.



- After selecting the edges, press Done

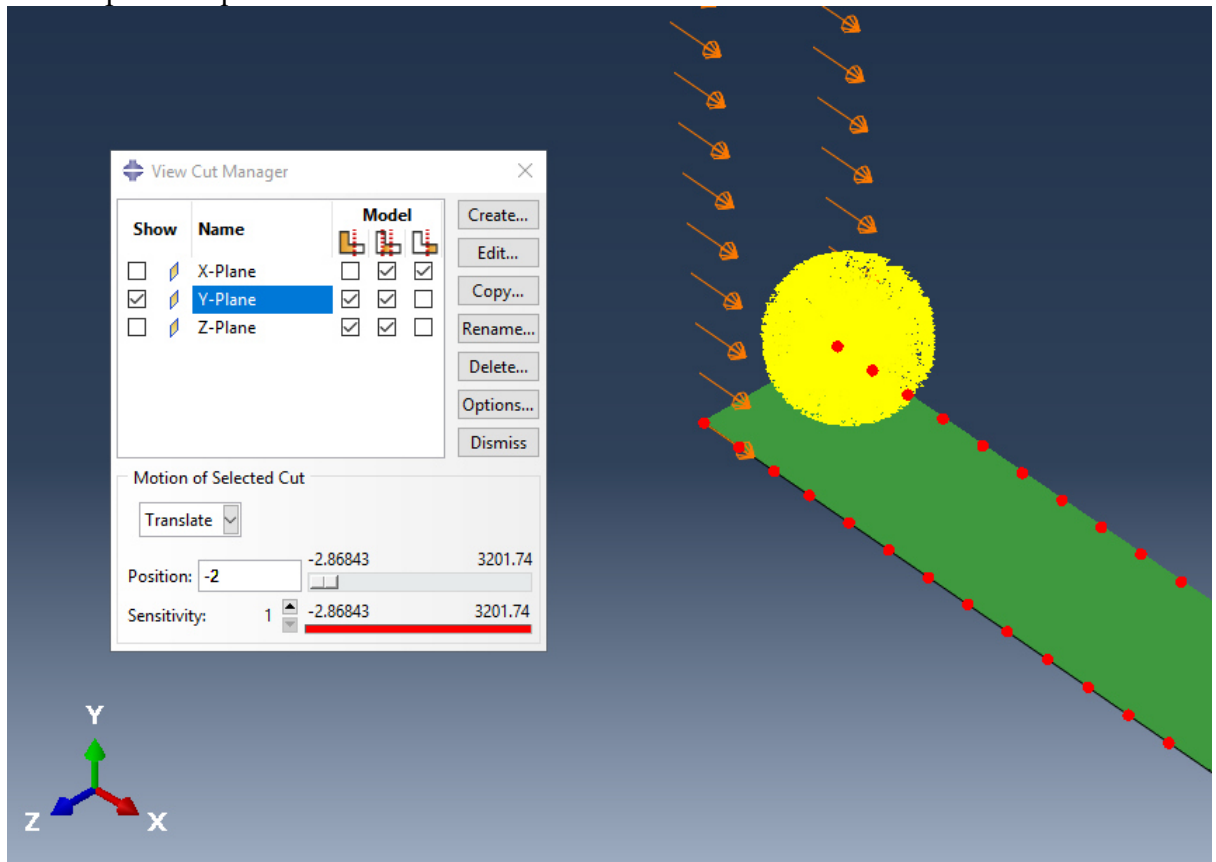


- The following tab appears and the mentioned data should be entered.



- Click Ok, Now Boundary Condition 3 is created. Similarly, we have to create Boundary conditions for all other edges.
- 28. Select Module → Load → Create boundary condition
- Provide a name FIX BOTTOM
- Select the category to be mechanical
- Select Type for the selected step to be Displacement/Rotation.

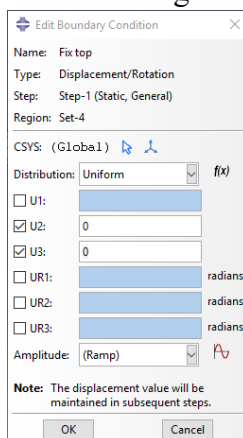
- Locate and click on Activate/Deactivate View Cut Manager in tools. A tab as see below will appear. Adjust the Position values to isolate and display only the edge portion of the sample as required.



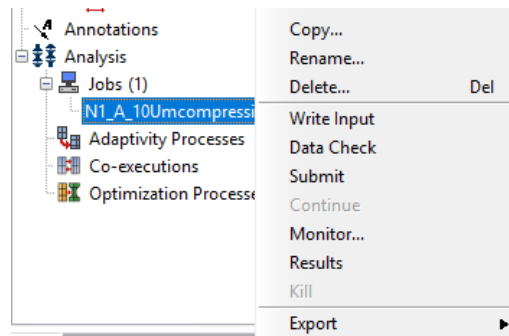
- After selecting the edges, press Done



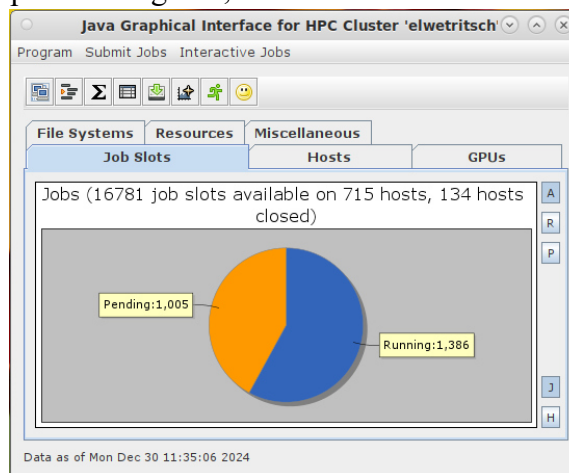
- The following tab appears and the mentioned data should be entered.



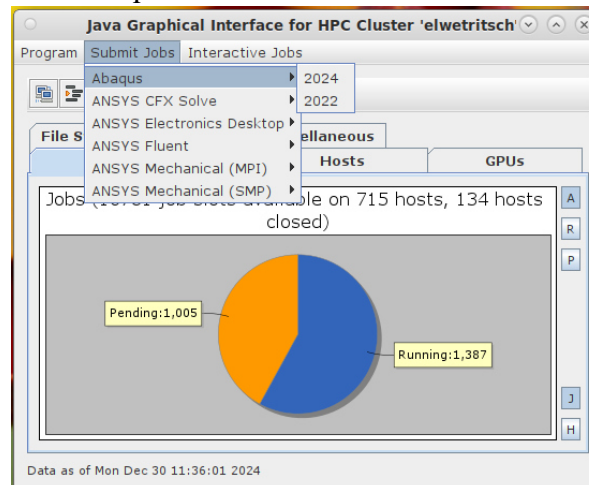
- Click Ok, Now Boundary Condition 4 is created. Similarly, we have to create Boundary conditions for all other edges.
29. Select Module → Job → create Job → Provide a name and click Ok. A new dialogue box will appear select Ok. Now a job will be created.
  30. Open the Job tab, right-click on the file created, and select Write Input. This action will generate an .inp file, which can be found in current work directory and this file will subsequently be used to obtain the .odb file.



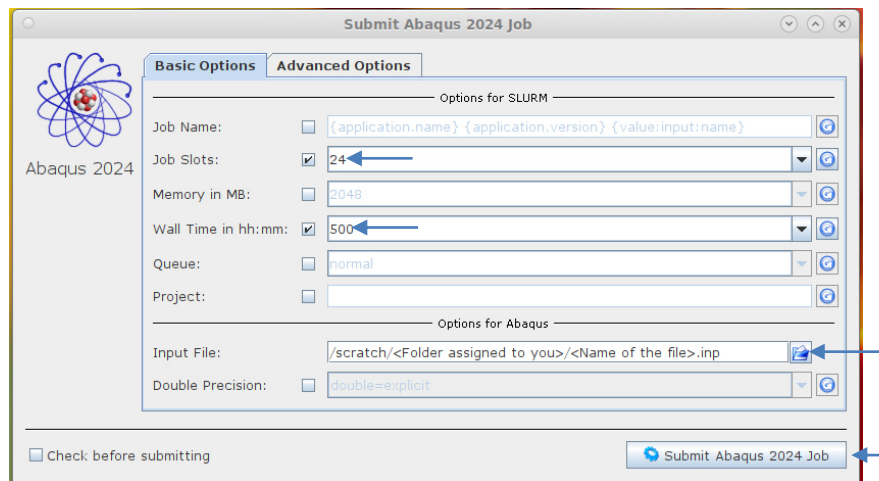
31. As the we are working on Remote Desktop connection Elwetrirsch set the work directory to be My computer → File system →scratch→ <Folder assigned to you>
32. Upon saving the file, follow these steps to generate the .odb file. Navigate to Applications → RPTU Software → jSLURM – SLURM Graphical User Interface. This action will open a dialog box, as illustrated below.



33. Go to Submit jobs → Abaqus → 2024



34. Ensure that all required details are correctly filled in, and then proceed to submit the Abaqus 2024 job.



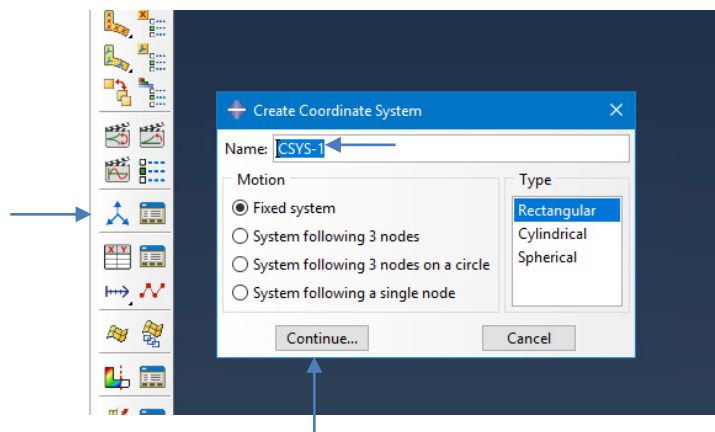
35. Once the job is complete, you will receive a notification via email. The finished .odb file can be located on your system by navigating to My Computer → File System → scratch → <Folder assigned to you>.

```

Job ID: 13239743
Cluster: elwetrtsch
User/Group: /sacc
State: COMPLETED (exit code 0)
Nodes: 1
Cores per node: 24
CPU Utilized: 02:02:05
CPU Efficiency: 66.79% of 03:02:48 core-walltime
Job Wall-clock time: 00:07:37
Memory Utilized: 579.26 MB
Memory Efficiency: 1.21% of 46.88 GB

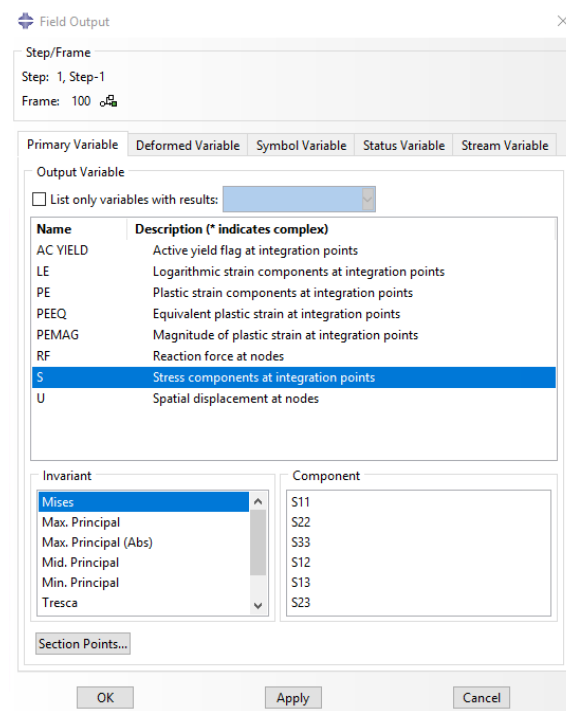
```

36. This .odb file can be opened in Abaqus to analyse the stress and strain within the sample by following these steps. File → Open → <open the respective .odb file>  
 37. Create a coordinate system, assign it a name, and click Continue to proceed.

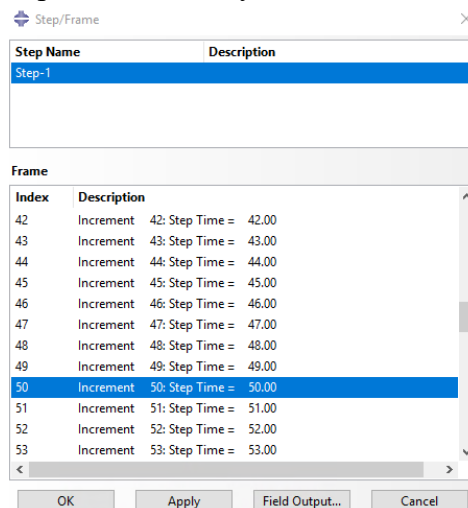


38. A dialog box will appear; press Enter three times to assign values to the three axes.  
 39. The next step is to navigate to Result → Options → Transformation → User-specified, select CSYS1, and click OK.

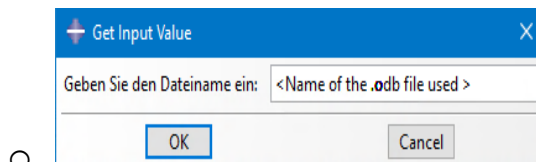
40. Navigate to Result → Field Output to analyse various types of stress and strain.

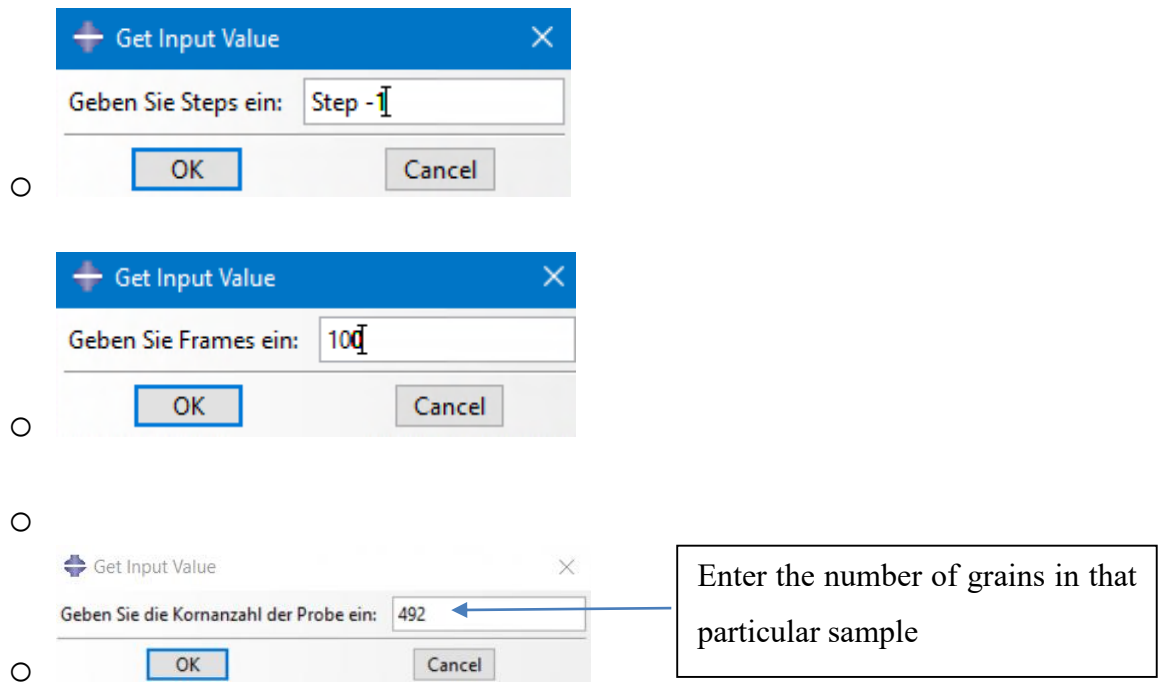


41. Navigate to Result → Step/Frame to analyse stress and strain at different steps.



42. To calculate the resulting shear stress, use a specific Python script (Schubspannungen - N1A.py). Execute it by navigating to File → Run Script and selecting the script. A series of dialog boxes will then appear. Do the following.





43. Upon executing this a file of odb.results format will be obtained from which resulting shear stress plot can be viewed and analysed. This file can be found in the preselected directory.

By following all the steps and using the data obtained we can perform GND analysis

### 7.1. Calculation of energy needed to move a dislocation

The energy required to move a dislocation is determined by considering key parameters such as shear stress, the Burgers vector, and the distance travelled by the dislocation line. The following section outlines the steps involved in the calculation.

For a material like IN617 the elastic energy stored per unit length of dislocation is given by

$$E_d = \frac{1}{2} \frac{Gb^2}{(1-\nu)} \quad (3)$$

Where  $E_d$  is the energy per unit length of dislocation (J/m),  $G$  is the shear modulus(Pa),  $b$  is the burgers vector (m) and  $\nu$  is Poisson's ratio.

Work required to move dislocation over a distance  $L$  against an applied shear stress  $\tau$  is given by

$$w = \tau \cdot b \cdot L \quad (4)$$

Where  $W$  is the work done(J),  $\tau$  is applied shear stress(Pa),  $b$  is burgers vector (m),  $L$  distance moved by dislocation (m).